

Investigation of the mechanical behaviour of conical cans with large slopes

Auteur : De Oliveira Vieira, Marcos Vinicius

Promoteur(s) : Rigo, Philippe

Faculté : Faculté des Sciences appliquées

Diplôme : Master : ingénieur civil mécanicien, à finalité spécialisée en "Advanced Ship Design"

Année académique : 2022-2023

URI/URL : <http://hdl.handle.net/2268.2/18056>

Avertissement à l'attention des usagers :

Tous les documents placés en accès ouvert sur le site le site MatheO sont protégés par le droit d'auteur. Conformément aux principes énoncés par la "Budapest Open Access Initiative"(BOAI, 2002), l'utilisateur du site peut lire, télécharger, copier, transmettre, imprimer, chercher ou faire un lien vers le texte intégral de ces documents, les disséquer pour les indexer, s'en servir de données pour un logiciel, ou s'en servir à toute autre fin légale (ou prévue par la réglementation relative au droit d'auteur). Toute utilisation du document à des fins commerciales est strictement interdite.

Par ailleurs, l'utilisateur s'engage à respecter les droits moraux de l'auteur, principalement le droit à l'intégrité de l'oeuvre et le droit de paternité et ce dans toute utilisation que l'utilisateur entreprend. Ainsi, à titre d'exemple, lorsqu'il reproduira un document par extrait ou dans son intégralité, l'utilisateur citera de manière complète les sources telles que mentionnées ci-dessus. Toute utilisation non explicitement autorisée ci-avant (telle que par exemple, la modification du document ou son résumé) nécessite l'autorisation préalable et expresse des auteurs ou de leurs ayants droit.



With the support of the
Erasmus+ Programme
of the European Union



Investigation of the mechanical behaviour of conical cans with large slopes

submitted on 07 August 2023

by

DE OLIVEIRA VIEIRA Marcos Vinicius

Leuvenselaan 55

3300 Tienen

marcos.vieira@uni-rostock.de

Student ID No.: 222202305

First Reviewer:

Prof. Dr. Patrick Kaeding

Universität Rostock

Universitätsplatz 1

18055 Rostock

Germany

Second Reviewer:

Dr. Ir. Timothee Pire

ParkWind N.V.

Sint-Maartenstraat 5

3000 Leuven

Belgium

External Reviewer:

Prof. Simone Saettone

Universidad Politécnica de

Madrid

Escuela Técnica Superior

de Ingenieros Navales

Av. de la Memoria, 4,

28040 Madrid

Spain

[This page is intentionally left blank]

Contents

List of Figures	iv
List of Tables	vi
List of Abbreviations	vii
Abstract	ix
1 INTRODUCTION	1
1.1 Background and motivation	1
1.2 Problem statement	2
1.3 Objective and aims	4
1.4 Report structure	4
2 STATE OF ART	5
2.1 Current practices	5
2.2 The transition region	10
3 PROPOSED DESIGNS	12
3.1 Design 1: conical TP with one large angle	12
3.2 Design 2: conical TP with two large angles	13
3.3 Design 3: stairwise TP	15
4 ANALYTICAL INVESTIGATION	17
4.1 Loads definition	17
4.2 Global stress assessment	18
4.3 Lateral deflection and TPE	28
4.4 Ultimate limit state theory	29
4.4.1 <i>Tubular connections: axial compression</i>	31
4.4.2 <i>Tubular connections: bending</i>	32
4.4.3 <i>Tubular connections: shear</i>	32
4.4.4 <i>Tubular connections: loads interaction</i>	33
4.4.5 <i>Tubular connections: buckling as shell cylinder and as shell column</i>	33
4.4.6 <i>Conical connections</i>	35
4.5 Fatigue limit state theory	37
4.5.1 <i>Stress concentration factors</i>	38
4.5.2 <i>S-N curve</i>	39
4.6 Analytical results	40
4.6.1 <i>Minimum thickness</i>	40
4.6.2 <i>Maximum deflection and TPE</i>	43

4.6.3	<i>ULS results</i>	43
4.6.4	<i>FLS results</i>	46
4.6.5	<i>Slope and thickness sensitivity analysis</i>	48
5	NUMERICAL INVESTIGATION	52
5.1	Applicable codes and standards	52
5.2	Geometry	52
5.3	Physical formulation and hypothesis	53
5.4	Mesh study	54
5.5	Displacement and Von Mises stresses	59
5.6	Discontinuities	62
6	COMPARISON AND DESIGN DISCUSSION	66
6.1	Analytical and numerical comparison	66
6.2	Design outcome	69
7	CONCLUSION	72
8	ACKNOWLEDGEMENTS	74
	References	75
A	DESIGN DRAWINGS	78
B	TABLES AND SPREADSHEETS	82
B.1	Main dimensions	82
B.2	Stress distribution	82
B.3	Fatigue Limit State	84
B.4	Ultimate Limit State	89
B.5	Extrapolated values - hot spot stress	96
C	FEA PLOTS	97

List of Figures

1	Monopile substructure, foundation and its elements [1].	1
2	Scheme of MP-TP connection with main dimensions	3
3	Summary of the standard monopile manufacturing process [2].	6
4	Navantia-Windar XXL monopile factory.	6
5	Illustrative images of the roller bending operation [3].	7
6	Variables for the calculation of the truncated cone profile [4].	7
7	Top view illustration of the rolling bending working space.	8
8	Roller welding beds.	9
9	TP-less monopile [5].	10
10	MP-TP connection types [6].	11
11	Proposed Design 1.	13
12	Proposed Design 2.	15
13	Proposed Design 3.	16
14	Models of boundary conditions	19
15	Clamped transition piece model.	20
16	Forces and moments application.	20
17	Bending moment distribution.	21
18	Torsional moment distribution.	21
19	Normal force distribution.	22
20	Shear force distribution.	22
21	Closed thin-walled section [7].	25
22	Shear stress sinusoidal distribution.	26
23	Section of a cylinder with two elements in different circumferential positions.	27
24	Types of cross-sections.	30
25	Buckling modes.	34
26	Cone geometry.	35
27	Sources of stress concentrations in tubular connections.	38
28	Parameters of the conical-tubular connections.	39
29	Variation of the maximum SCF.	49
30	Variation of the calculated fatigue life.	50
31	Variation of the maximum SCF in can_1.	50
32	Variation of the calculated fatigue life in can_1.	51
33	Surface geometries in NX interface.	53
34	Boundary conditions imposed in NX.	54
35	6 nodes shell element.	55
36	Global convergence of Design 1.	56
37	Global convergence of Design 3.	57

38	Aspect ratio metric.	57
39	Warping factor metric.	58
40	Finer mesh of 100 mm at Design 3 geometry.	58
41	Displacement field Design 1 Maximum value: 7.97 mm	59
42	Displacement field Design 3 Maximum value: 10.63 mm	60
43	Von Mises Stress Design 1 Maximum value: 128.47 MPa	60
44	Von Mises Stress Design 3 Maximum value: 167.87 MPa	61
45	Von Mises stress Front view Stresses combined at nodes.	62
46	Discontinuities Design 1 Front view Maximum value: 66.06.	63
47	Discontinuities Design 2 Front view Maximum value: 148.85.	63
48	Derivation of hot spot stress through linear extrapolation [8].	64
49	Local refinement for extrapolation of hot spot stress.	65
50	TPE convergence plot comparison	67
51	Stress distribution along Design 1 from FEA and analytical approach.	67
52	Stress distribution along Design 3 from FEA and analytical approach.	68
53	Von Mises stresses at different points in Design 1	70
54	Collar component from Design 3.	71
55	Production rolling forging equipment to manufacture rings and collars [9].	71

List of Tables

2	General constraints on the project.	3
3	Fixed dimensions of cans of Design 1.	12
4	General configuration of Design 1.	13
5	Fixed dimensions of cans of Design 2.	14
6	General configuration of Design 2.	14
7	Fixed dimensions of cans of Design 3.	15
8	General configuration of Design 3.	16
9	ULS extreme load values and load cases	18
10	FLS loads - Damage equivalent loads.	18
11	Load condition and respective stress generated.	23
12	Design 1 minimum can thickness to pass all ULS and FLS criteria, in mm.	41
13	Design 2 minimum can thickness to pass all ULS and FLS criteria, in mm.	41
14	Design 3 minimum can thickness to pass all ULS and FLS criteria, in mm.	42
15	The total mass of each design, in tonnes.	43
16	Analytical results of the TPE absolute value and maximum lateral deflection.	43
17	Stresses result at the junctions of Design 1, in MPa.	44
18	Stresses result at the junctions of Design 3, in MPa.	44
19	Main ULS results from the tubular junction of Design 1.	45
20	Main ULS results from the conical junctions of Design 1.	45
21	Main ULS results from the tubular junction of Design 3.	46
22	Main ULS results from the conical junctions of Design 3.	46
23	Stress concentration factors for Design 1 components and junctions.	47
24	Stress concentration factors for Design 3 components and junctions.	47
25	Main fatigue life results of Design 1.	48
26	Main fatigue life results of Design 3.	48
27	Refinement study for Design 1.	56
28	Refinement study for Design 3.	56
29	Geometry approximation results for the finer mesh.	59
30	Stress distribution results from FEA for Design 1.	61
31	Stress distribution results from FEA for Design 3.	61
32	Hot spot stresses at junctions of Design 1, in MPa.	65
33	Hot spot stresses at junctions of Design 3, in MPa.	65
34	Comparison between numerical and analytical TPE and deflection results for Design 1.	66
35	Comparison between numerical and analytical TPE and deflection results for Design 3.	66
36	Total mass of Design 1 and Design 3, in tonnes.	69

[This page is intentionally left blank]

List of Abbreviations

CAD	Computer-aided design
DEL	Damage equivalent load
DOF	Degrees of freedom
FEA	Finite element analysis
FEM	Finite element method
FLS	Fatigue limit state
LAT	Lowest astronomical tidal
LRFD	Load and resistance factor design
LSD	Limit state design
MP	Monopile
SCF	Stress concentration factor
TP	Transition piece
TPE	Total potential energy
ULS	Ultimate limit state
WTG	Wind turbine generator

DECLARATION OF AUTHORSHIP

I, **DE OLIVEIRA VIEIRA, Marcos Vinicius** declare that this thesis and the work presented in it are my own and have been generated by me as the result of my own original research.

Where I have consulted the published work of others, this is always clearly attributed.

Where I have quoted from the work of others, the source is always given. With the exception of such quotations, this thesis is entirely my own work.

I have acknowledged all main sources of help.

Where the thesis is based on work done by myself jointly with others, I have made clear exactly what was done by others and what I have contributed myself.

This thesis contains no material that has been submitted previously, in whole or in part, for the award of any other academic degree or diploma.

I cede copyright of the thesis in favour of the University of Rostock.

Date: 07/08/2023

Signature: *Marcos Vieira*

[This page is intentionally left blank]

ABSTRACT

Currently, monopile foundations are the most used type of fixed-bottom structures in the offshore wind industry. The support structure of a fixed offshore wind turbine also includes a transition piece that connects the monopile to the wind tower. Both monopile and transition pieces are commonly manufactured from welded cans. Moreover, often this connection needs to overcome a diameter disparity between the pile and the wind tower. In a typical design, this transition between diameters is done by using conical cans in the monopile, in addition to the usual cylindrical ones. The greater the disparity, the greater the required slope on the conical cans.

However, a non-conventional solution is offered. It consists of performing the diameter change in the transition piece by means of conical cans. In that sense, the primary steel of three different transition pieces is designed using a given available clearance based on a real case situation. In addition, slope angles larger than the current industrial limit of 5° are considered.

The proposed transition piece concepts are investigated in the face of the applicable standards for the limit states. The aim is to obtain a minimum thickness of the cans that complies with all the criteria established by the design standards. Initially, the ultimate limit states are assessed analytically. Later, a computational analysis using the finite element method provides comparable results. Moreover, the fatigue limit state is also studied, especially the stress concentration factors generated by the conical cans and the effect that the slope angle has on the fatigue life of the cans.

The results indicate how the large slope cans become a critical source of stress intensification in the transition piece structure by increasing the stress concentration factors, creating singularity regions, and interfering with the local stress convergence. Finally, a discussion about manufacturing challenges related to the production of conical cans is introduced for the case of the proposed designs.

1. INTRODUCTION

1.1. Background and motivation

Fixed structures are currently the most common solution for the foundation of offshore wind turbines, especially in the case of water depths less than 60 meters. Among some alternatives, the monopile foundations are quite popular due to lower manufacturing, transport, and installation costs. Generally, these structures are installed in a water depth range between 10 m and 30 m, with larger piles that may reach up to 60 m in the coming future [10]. More than 65% of the wind farms currently installed in the North Sea are based on monopile foundations and substructures [11].

Monopiles (MP) are typically hollow steel cylinders, usually composed of cans welded together, that extend upwards from below the mudline and attach to a transition piece (TP) that links the foundation to the tower and turbine. As Figure 1 shows, monopiles are not only a foundation element, but also part of the substructure together with the transition piece. On top of that, a complete setup of this type of fixed offshore wind platform includes secondary steel elements such as corrosion protection systems, boat landings to provide access to the monopile via a ladder, internal platforms that feed in cables, and external platforms that allow access from vessels enabling maintenance to take place.

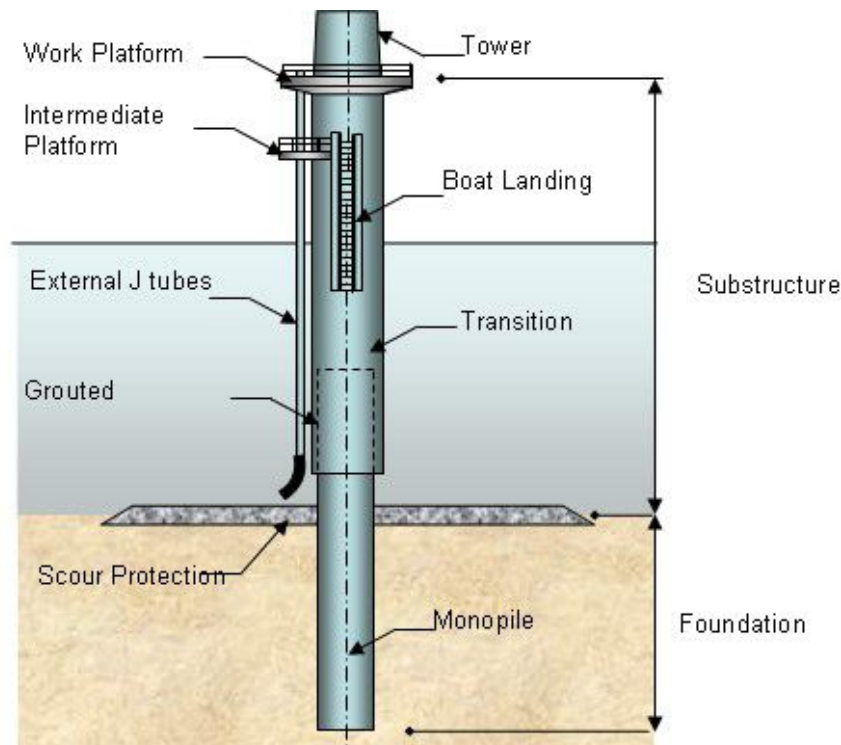


Figure 1: Monopile substructure, foundation and its elements [1].

Typically, the top part of the substructure consists of a cylindrical section with an

outer diameter corresponding to the wind turbine tower's bottom diameter. In the same way, the bottom part is also cylindrical with the pile's outer diameter needed to fulfil the design criteria of stiffness and resistance. Finally, the transition piece is the component that brings these two parts together and holds up the secondary steel elements. This transition element is also a fundamental structural component as it receives the loads that act on the wind turbine and ultimately transfers them to the foundation. Similarly to the monopile, it is composed of steel cans welded together. Nowadays, a TP-less concept may also be found and it consists of combining the MP and the TP in a single structure.

1.2. Problem statement

The constant and increasing progress in the development of larger offshore wind turbines brings along new demands and conditions that impose design limitations. Part of these limitations affect directly the design of the transitioning region and the way how one goes from a larger diameter at the bottom to a smaller diameter at the top of the substructure.

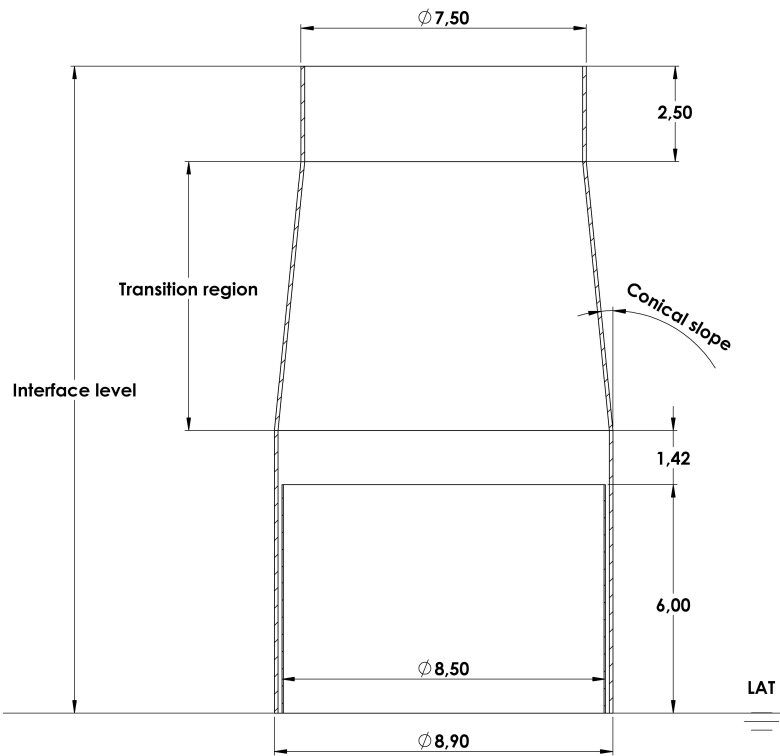
As mentioned in subsection 1.1, in a typical MP the top diameter is governed by the tower's dimensions given by the wind turbine supplier, and the bottom diameter is determined according to the soil conditions. Moreover, a height constraint is present along the transitioning region. At first, it imposes that the substructure must be high enough to achieve a specific air gap clearance that protects the external platform from water. On the other hand, the substructure must be low enough to reduce or maintain the interface level and hub height in order to control the lever arm, reduce the magnitude of the generated moments, and reduce the requirements for installation vessel crane height. Furthermore, aspects such as cabling routes and space for secondary steel elements attachment may also play a role and impose requirements for the total height available for the transition from a larger to a smaller diameter.

Normally, this transition of diameter along a certain height is promoted by means of conical slope cans in the MP. However, large slope angles may arise if two scenarios are present: a large diameter disparity needs to be overcome, or a very limited vertical clearance is available to develop the transition. Both conditions will require rough changes in diameter that may be translated into the use of cans with slopes larger than the industry limit of 5° . In subsection 2.1 this specific limitation is further explored.

This project, based on a reference case, aims to study a non-typical setup in which the MP is cylindrical and the conical cans are part of the TP, instead. Furthermore, large slope cans are considered. In that sense, it becomes important to study the overall impact of large slope TPs in terms of transferred loads and on the limit states of the substructure. In this context, possible solutions regarding TP designs are assessed based on the site and load conditions from a specific offshore wind project. Inspired by this case, the constraints described in Table 2 and Figure 2 are imposed.

Table 2: General constraints on the project. LAT is the lowest astronomical tidal.

Parameter	Value	Unit
Distance from the top of MP to LAT	6.00	m
Upper straight section of TP	2.50	m
Clearance from the top of MP to the conical shape	1.42	m
MP outer diameter	8.50	m
TP outer diameter	8.90	m
Top of the TP outer diameter	7.50	m
Interface level	17.00	m

**Figure 2:** Scheme of MP-TP connection above the LAT with main dimensions and constraints for a specific site condition. The MP is fully cylindrical and the conical slope is imposed on the TP.

The 1.42 metres clearance between the conical shape region and the top of the MP is important for installation and maintenance reasons. In case of a bolted connection between MP and TP, this clearance leaves the necessary space for a tool or bolt tensioner. In the case of grouted connections, this space is also important for the grout injection, as an internal platform is located in this region. Furthermore, the 6 metres from the top of the MP to the LAT is also an important gap to avoid any water pressure below this internal platform. Figure 2 does not illustrate the full TP, but only its extension until the LAT. The TP may extend over 7 meters below the LAT, however, in this project, just

part of the structure is considered and, as it will be defined later due to the boundary conditions, only the TP region from above the MP height is taken into account.

1.3. Objective and aims

This report aims to identify and investigate the challenges of the design and fabrication of large slope conical cans for the transition piece of offshore wind substructures. Starting from the constraint of the interface of a given site, some solutions are proposed in the design space available. Later, their structural aspects are analytically and numerically studied using the applicable codes and standards in addition to given environmental conditions. Initially, the goal is to check if the suggested concepts comply with the rules in terms of the limit states. Some studies are performed in order to understand the effects of large slopes and the behaviour of the proposed designs. Following, fabricability is assessed and final outcomes about the designs are given.

1.4. Report structure

At first, in section 2, an overview of the current practices in terms of MP-TP design is introduced. The TP structure is discussed and alternatives for the transition region are designed. Following that, section 3 presents the three proposed TP designs that are studied in this project. Their dimensions, components, and connection types are defined.

Next, on section 4, an analytical investigation is realized with the support of the applicable standards. Firstly, a simplified setup is defined for the structure and boundary conditions in order to study its behaviour in the face of a static linear problem. Some hypothesis are presented as well as their limitations. Following, using the mechanical of materials approach, a description of the stress distribution in the TP is suggested. Moreover, analytical calculations of the maximum deflection and total potential energy are assessed. Lastly, several ULS and FLS criteria are described, the main results are presented and additional analyses are performed aimed to verify the effect of the can slope on FLS results.

On section 5, a numerical approach is offered to study specifically the stress distribution along the TP. Aspects such as geometry preparation, mesh study, convergence, and singularities are addressed. On top of that, the results are introduced. In the end, an approach is implemented to deal with the stress at the junctions using local mesh refinement and the derivation of hot spot stresses using extrapolation.

Finally, section 6 draws some comparisons between the numerical and analytical results and offers some explanations for the deviations and correlations found. The designs proposed are discussed not only regarding the challenges that arise in terms of the mechanical response to the external loads but also regarding the specific manufacturing obstacles of each one of them. Lastly, suggestions are proposed to deal with it.

2. STATE OF ART

2.1. Current practices

The design of a monopile is a multidisciplinary and complex task. It requires taking into consideration aspects related to the site characteristics, turbine characteristics, and ground profile. Moreover, installation and manufacturing particularities must be considered in advance so that the proposed design is feasible.

Some simplified design approaches have been proposed in the literature as initial tools for the selection of the pile dimensions [12]. Initially, they rely on the collecting of the input turbine, Meteocean, and geotechnical data. Along with these details, the limit state design criteria is assessed and an initial guess for the pile dimension is defined. Based on this initial value and on the site conditions, one can obtain the wave, current and wind loads and the pile dimensions are updated accordingly.

In the last couple of years, pushed by increasingly larger and more efficient turbines, the industry also developed larger monopiles so that regular-size monopiles with diameters of 5-6 metres have been superseded by the so-called XL monopile (diameters of 6-8 metres) and, even more by XXL monopiles (diameters of 8-11 metres). Despite fabrication challenges, the XXL monopile has been widely used nowadays due to efforts to scale up the capabilities in order to obtain a strong supply chain, lower costs, and relatively easy installation [13]. The thickness of these monopiles may vary between 70 mm and 140 mm and it weighs up to 2500 tons.

The manufacturing process is quite similar for all sizes. First, one bevels steel plates. The industry standard is to use S355 structural steel [12]. After that, the plates are rolled using 3 or 4 rolls bending machines and tack welded. Later, one applies longitudinal welding and obtains a cylindrical can section. In order to get the long seamless pile, several cans are positioned and welded together by applying internal and external circumferential butt welding. In the end, measurements are done to check the dimensional quality, the quality of the weld is assessed through non-destructive testing (NDT), the structure is blasted, primer is used and, finally, the coating is applied. A summary of the process is shown in Figure 3.

The transition piece is fabricated on a similar process. In the case of a cylindrical TP, the process is identical and simpler as straight rectangular plates are cut to be rolled and welded. However, in some cases, a conical can is mandatory to provide a smoother transition along the transitioning region. This type of structure provides a more gradual narrowing that can distribute loads more efficiently, minimize stress concentrations and reduce the overall weight.

Cylindrical and conical cans are both manufactured by means of roller bending machines. The process is one of the stages of an assembly line layout in a manufacturing plant. Overall,

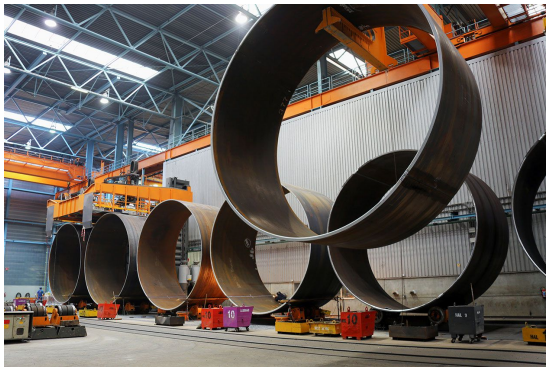
it includes the cutting, feeding, bending, and welding of the cans, in addition to inspections, calibration, coating, and storage. Figure 4 shows an example of this type of factory.



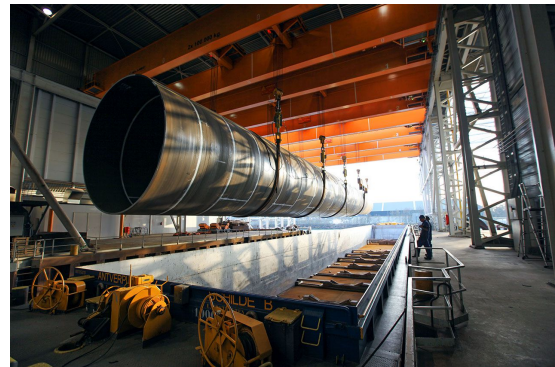
(a) Steel plates.



(b) Bending process to provide the can curvature.



(c) Cans as a result of the welded plates.



(d) Near finished monopile after the welding of several cans.

Figure 3: Summary of the standard monopile manufacturing process [2].

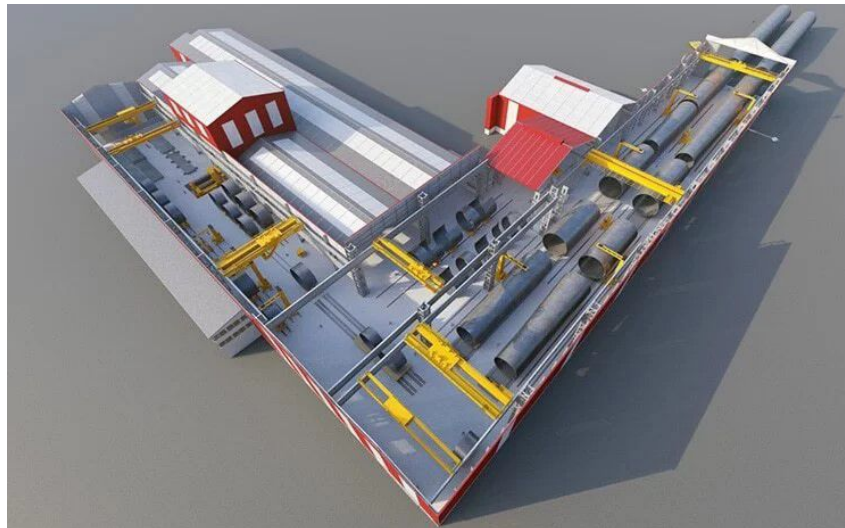
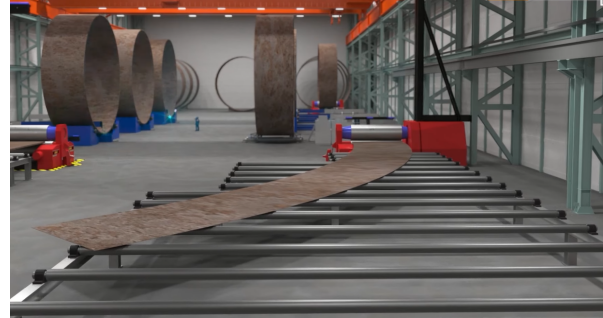


Figure 4: Navantia-Windar XXL monopile factory. On the top left is located the area for cutting plates and bending the cans. Following the flow of the factory plant, it depicts the welding area and the output of the assembled monopiles. The process is similar for TPs [14].

In the specific case of conical cans, the procedure encounters some extra limitations. One of them is related to the required space in order to perform the bending process of the cans. Generally, the plate is transported through a roller feed table and it inlets the roller bending machine, as shown in Figure 5.



(a) Rolling bending operation | Cylindrical can



(b) Rolling bending operation | Conical can

Figure 5: Illustrative images of the roller bending operation [3].

Nonetheless, depending on the slope of the can to be produced, the shape and dimension of the plate change. More specifically, the larger the slope, the larger the dimensions required to move the plate and feed it into the roller bending machine. Currently, the most common slope angle resides in the range between 1° and 3° , and there are companies able to produce cans until 5° [15].

A truncated cone profile is formed from an unfolded curved plate. In order to sketch the workspace needed, one needs to calculate the dimensions of the unfolded plate. Equation 1 to Equation 3 and Figure 6 present the formulas and variables to obtain the dimensions.

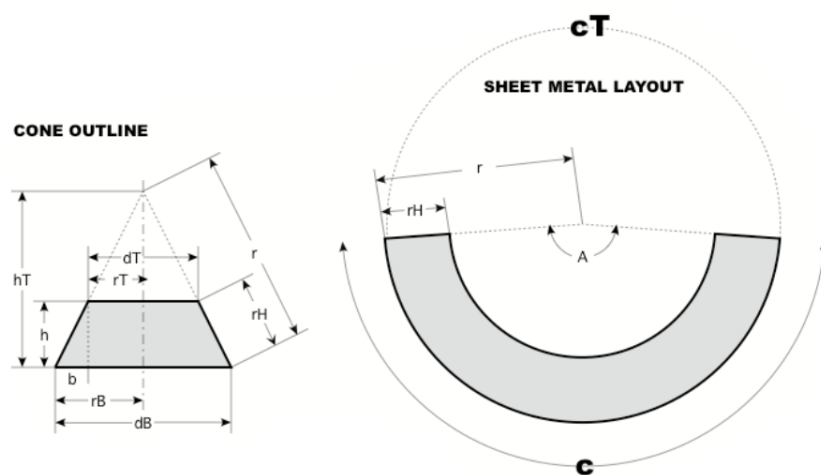


Figure 6: Variables for the calculation of the truncated cone profile [4].

$$h_T = \frac{hdB}{dB - dT} , \frac{hdB}{dB - dT} \quad (1)$$

$$r_H = \sqrt{h^2 + b^2} , r = \sqrt{h_T^2 + r_B^2} \quad (2)$$

$$c = \pi dB , c_T = 2\pi r , A = \frac{360c}{c_T} \quad (3)$$

Considering this, two sketches are drawn in order to compare the working space necessary to feed in the plates, as shown in Figure 7. One of them is done for a reference can with a slope of 3° . The other one is an unfolded profile with a slope of 6° . Moreover, a minimum clearance of 1.5 metres is defined between the work table and the plate.

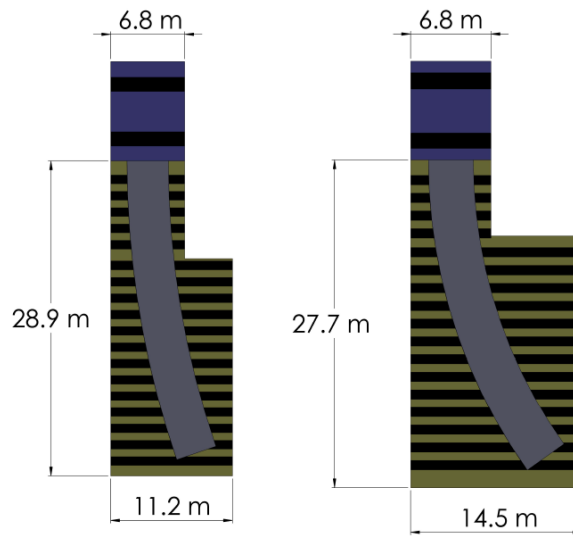


Figure 7: Top view illustration of the rolling bending working space. The figure on the left is the reference can case (3° slope) and the figure on the right is the case of a large slope can with 6° . In blue is the rolling bending machine, and in yellow is the rolling feed table.

Therefore, the larger slope can require a 3.3 metre wider working space in the inlet region. This may be a bottleneck or not depending on the manufacturer and factory layout. On top of that, other factors may be affected by this larger slope, such as the outlet space and the forces in the rolling bending machine

Another challenge that steep angles bring to manufacturing is concerning the welding between cans. This procedure is done with the help of rollers that can incline up to the conical slope so that the conical surface sits on them while the cone axis remains horizontal, as shown in Figure 8. However, large slope shapes affect the welding rollers' capacity to effectively position the cans during the welding operation. In other words, the steeper the angle of the cone, the higher the propensity of the cone to fall off the rollers during the operation. Due to all these reasons, for most of the fabricators, the conical slope limit is 5° [15].



Figure 8: Roller welding beds are used for turning the structure for welding. Further, it helps to readjust the cans positioning in order to account for the slope of the conical cans. However, the steeper the angle the more the structure tends to fall off the rollers [16].

In addition to the slope constraints, the manufacturing of the cans also presents thickness limitations. These limits are considered in subsection 4.6 when the final thickness of the cans is determined. Firstly, a maximum thickness of 140 mm is established for the cans. The bending process and the welding of truncated cone profiles thicker than that becomes costly and quite challenging for most of the manufacturers. Secondly, a maximum thickness jump of 20 mm is assumed for consecutive cans. This has to do with difficulties that may emerge during the alignment and the welding of the pieces.

After its production and assembly, the monopile is taken to the installation site on a floating vessel such as a barge or an installation vessel that tows the structure to the right location. Next, the monopile is upended and vertically hung with a crane usually located at the installation vessel. Then, it is lowered on its position around a positioning gripper frame. This equipment promotes pile driving and limits tilting motion.

Depending on the weight and on the site soil properties, the monopile initially self-penetrates the sea bed. A noise reduction system is placed around it and following, a hydro hammer is used to drive the structure into the soil. After that, a lifting tool is fixed in the transition piece and it levers and places the transition piece on top of the monopile for further fixation.

The transition piece installation is done, firstly, by lifting the structure from the installation vessel. Then, it is lowered on the MP, and depending on the type of MP-TP connection it is fixed. In the case of a grouted connection, after being lowered, the TP is fixed with grout[17]. In the case of a bolted connection, after being lowered, MP and TP are fixed by means of a bolted flange with a skirt that overlaps the MP, and then the

annulus between MP and TP is filled with grout.

2.2. The transition region

As mentioned in section 1, due to geometrical and site constraints in most cases it is needed to promote a diameter reduction between the lower and upper part of the substructure. In the context of this project, this has to be done along the region here defined as the transition region. Important to highlight that simply enlarging the wind turbine generator (WTG) tower would not be a proper solution, among other reasons, due to suppliers' constraints [15].

The most common practice to connect the tower to the MP is to use a transition piece in a MP-TP configuration. This element is a tubular steel structure that is directly connected to the monopile foundation and to the wind turbine tower. The MP-TP configuration, however, is not the only possible solution to deal with this transition region. More recently, TP-less alternatives have been adopted [18], as shown in Figure 9. This configuration consists of a monopile also fabricated using steel cans that are welded together. However, the top can is equipped with steel stubs and supports to accommodate the secondary steel. This setup reduces inspection duration as it eliminates connections present in the MP-TP configuration.



Figure 9: TP-less monopile [5].

On the other hand, the installation of a TP-less design requires several lifts and a quite calm sea. Therefore, the traditional design using a transition piece still remains standard. Among its advantages, one may refer to the fact that the installation of the secondary steel components is done directly with the transition piece in one single structure. In addition, this design allows the use of a shorter monopile which means a vessel with a smaller

installation capacity and potential financial reductions. In the case of this traditional design, another critical aspect is the connection between the monopile and the transition piece. The main types are the grouted connection, the bolted flange connection, and the slip joint.

The grouted connection consists of filling the annulus between the two concentric parts (MP and TP) with a cementitious grout cast [6]. Usually, conical-shaped grouted connections are designed to avoid settlement issues, and shear keys are implemented to reduce damage in the grout, to provide extra resistance against slipping, and they consist of circumferential welds on both TP and MP surfaces [6]. These conical connections usually have a slope between 1° and 3° , reaching a maximum at 5° due to manufacturing constraints [15].

The bolted connections are composed of a ring flange that is manufactured on the inner surface of both MP and TP. These flanges are attached by means of high-strength bolts. Although these connections provide a safe and secure solution, they also face integrity challenges when it comes to fatigue crack initiation and propagation at threads. Moreover, the loss of pretension also contributes to the increase in the fatigue loading in the bolts.

The third possible type of connection is a slip joint. In this case, the parts are attached through friction between each individual part. This alternative presents a significant advantage in comparison to the grouted connection for not requiring the welding of shear keys which is a time-consuming process. Furthermore, this design reduces considerably the installation time and does not require any personnel to be present, reducing safety risks. The different connection types and variations are presented in Figure 10.

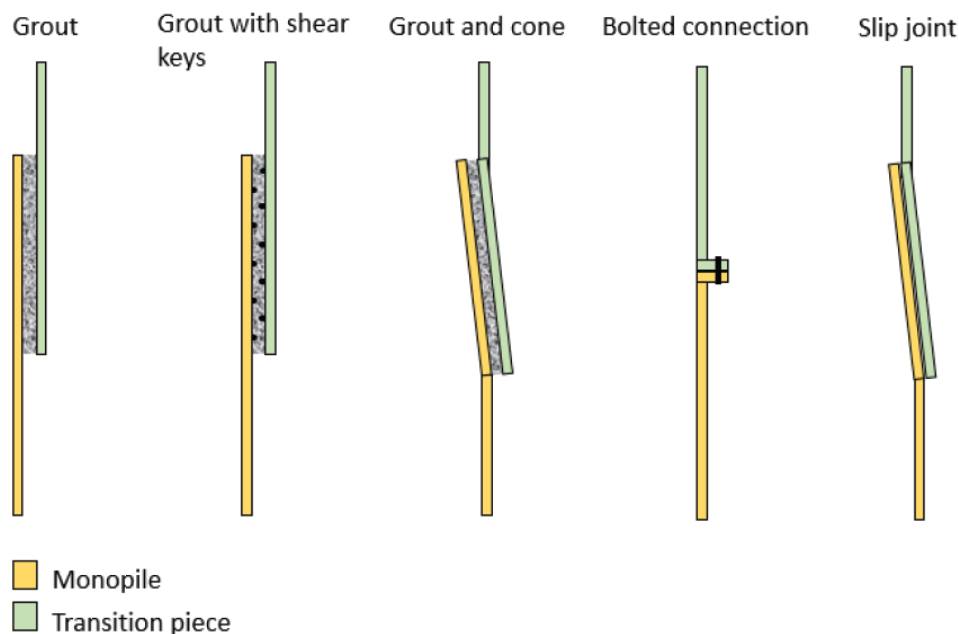


Figure 10: MP-TP connection types [6].

3. PROPOSED DESIGNS

Three TP designs are proposed according to the general constraints imposed in Table 2. All of them correspond to a TP-MP grouted connection without shear keys (first connection type in Figure 10). That is the connection adopted as it is the most suitable for this project. Moreover, the conical shape is imposed only in the TP.

These models are based on current solutions blended with the defined requirements and some adaptations. They were modelled using a CAD tool by applying a trial and error approach that would better fill the transition region. More detailed technical drawings are found in Appendix A. Furthermore, each design is composed of cans with a maximum height of 3.8 metres. The division into cans is imposed only along the transition region, therefore the sections above and below it are formed by a single cylindrical section (according to Figure 2), namely *top_can* and *bottom_can*.

In the tables below, *diameter at the top* refers to the diameter at the upper part of each can whereas the *diameter at the bottom* refers to the circular dimension at the lower part of the individual component. For truncated conical components, these dimensions will be different. Moreover, the slope is the angular measure from the vertical axis, as illustrated in Figure 2, and it is an individual can feature. Finally, *Connection type* refers to the type of link between the two cans according to the slope they have. In the case of both cans with the same angle from the vertical, one has a *tubular* connection, and in the case of the connection of cans with different slopes, one has a *conical* connection.

3.1. Design 1: conical TP with one large angle

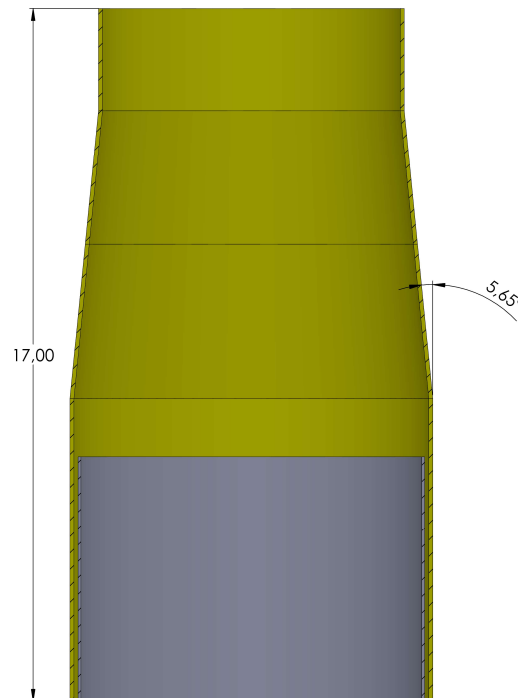
The first design (Figure 11) consists of a truncated conical shape generated within an interface level limit of 17 m. As a result, the transition region available is equal to 7.08 m, and a conical slope of 5.65° is generated which is over the theoretical limit of 5° as mentioned in section 2. Table 3 presents the dimensions, and Table 4 presents the components of this TP along with the type of connection between them. This design is generated from a straightforward link between the two diameters. It is composed of two intermediate cans in addition to the top and bottom ones.

Table 3: Fixed dimensions of cans of Design 1.

Components	Outer diameter at top [mm]	Outer diameter at bottom [mm]	Height [mm]	Slope [°]
top_can	7500.00	7500.00	2500.00	0.00
can_1	7500.00	8148.58	3280.00	5.65
can_2	8148.58	8900.00	3800.00	5.65
bottom_can	8900.00	8900.00	1420.00	0.00

Table 4: General configuration of Design 1.

Components	Junction	Connection type
top_can can_1	junction1	conical
can_1 can_2	junction2	tubular
can_2 bottom_can	junction3	conical

**Figure 11:** Design 1. In yellow is the TP above the LAT and in grey is the MP above the LAT.

3.2. Design 2: conical TP with two large angles

The second design (Figure 12) consists of sections that alternate between conical and tubular shapes (Table 6). Moreover, two conical cans are included with large angles, as given in Table 5. The interface level and the available transition region are kept the same, at 17 m and 7.08 m respectively.

This design is composed of more and shorter intermediate cans. The idea is to promote the diameter reduction by means of restricting the height of the cans that would exceed

the 5° limitation. As shown in section 2 the can height and slope are related to its required workspace. In that sense, as a larger slope would be needed, this design tries to reduce the height. In the end, this resulted in a greater number of cans needed and a design that interchanges between inclined and straight cans. The straight ones are fixed with 2 metres height and the inclined ones are even shorter.

Table 5: Fixed dimensions of cans of Design 2.

Components	Outer diameter	Outer diameter	Height	Slope
	at top [mm]	at bottom [mm]	[mm]	[°]
top_can	7500.00	7500.00	2500.00	0.00
can_1	7500.00	7500.00	2000.00	0.00
can_2	7500.00	8002.02	1500.00	9.50
can_3	8002.02	8002.02	2000.00	0.00
can_4	8002.02	8900.00	1580.00	15.86
bottom_can	8900.00	8900.00	1420.00	0.00

Table 6: General configuration of Design 2.

Components	Junction	Connection type
top_can	junction1	tubular
can_1		
can_1	junction2	conical
can_2		
can_2	junction3	conical
can_3		
can_3	junction4	conical
can_4		
can_4	junction5	conical
bottom_can		

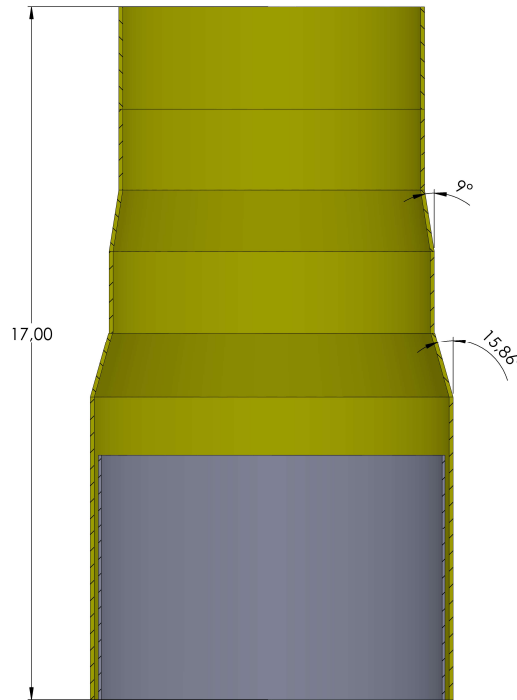


Figure 12: Design 2. In yellow is the TP above the LAT and in grey is the MP above the LAT.

3.3. Design 3: stairwise TP

The third alternative to be investigated (Figure 13) is a stair-wise design. The idea of this model is to reduce the diameter along the transition region using conical cans within the 5° maximum slope and the interface level limit of 17 m.

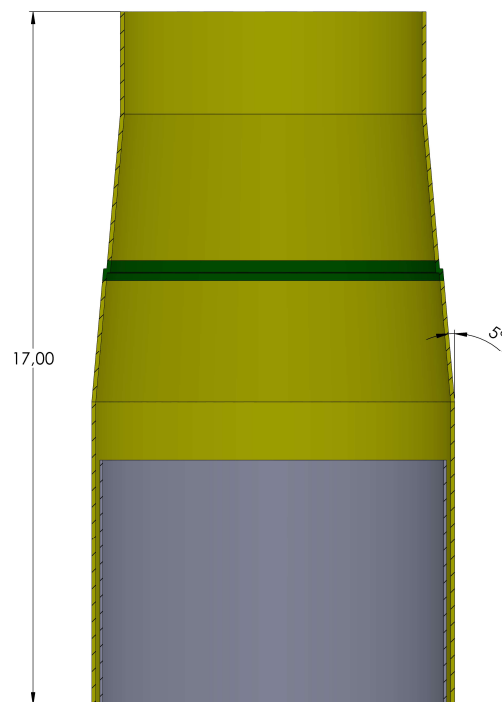
Nonetheless, to promote that, the intermediate cans are welded to a forged component named *collar* (in Table 7 and Table 8) that connects them in pairs. The collar slope is also 5° , and a more detailed drawing is found in Appendix A.

Table 7: Fixed dimensions of cans of Design 3.

Components	Outer diameter	Outer diameter	Height [mm]	Slope [°]
	at top [mm]	at bottom [mm]		
top_can	7500.00	7500.00	2500.00	0.00
can_1	7500.00	8130.62	3604.00	5.00
collar	8130.62	8377.52	490.00	5.00
can_2	8377.52	8900.00	2986.00	5.00
bottom_can	8900.00	8900.00	7420.00	0.00

Table 8: General configuration of Design 3.

Components	Junction	Connection type
top_can can_1	junction1	conical
can_1 collar	junction2	tubular
collar can_2	junction3	tubular
can_2 bottom_can	junction4	conical

**Figure 13:** Design 3. In yellow is the TP above the LAT and in grey is the MP above the LAT.

4. ANALYTICAL INVESTIGATION

Each one of the designs presented in section 3 is evaluated in the face of DNV-ST-0126 [19]. This is a standard for the design of wind turbine support structures, such as transition pieces. In that sense, all requirements, principles, and acceptance criteria are assessed for obtaining the limit states of the steel substructure. Along with other standards and recommended practices, this document is used as the main guideline for the design analysis. The approach consists of fixing the diameter and height dimensions as presented in Table 4 to Table 7, and varying the thickness of the cans in order to find the minimum thickness that would pass all the limits state conditions.

The standard DNV-OS-J101 defines the limit state as a condition beyond which a structure or structural component will no longer satisfy specific design requirements [20]. The limit states design method (LSD or LRFD) introduces load and material factors into the design loads and material resistance in order to account for uncertainties and obtain a more conservative estimation of the structure's safety and serviceability.

In this project, the ultimate limit state (ULS) and the fatigue limit state (FLS) are assessed. The former refers to a once-in-a-lifetime event of collapse or extreme deflection, and the latter refers to a possible failure or crack initiation due to cyclic loads. The ULS for the transition piece is obtained through the NORSOK N-004 [21] and the DNV-RP-C202 [22], whereas the FLS is evaluated using the DNV-RP-C203 [8].

4.1. Loads definition

Two sets of load conditions are used for the evaluation of limit states. One for the ULS and another for the FLS. These loads are considered as boundary conditions (external loads) of the model that studies the transition piece design only and they are imposed at the interface level, at 17 mLAT (Figure 2). In the case of the ULS, extreme resulting load conditions corresponding to a return period of 50 years are used. These loads are generated by different design load cases according to IEC 61400-1-3 [23]. These load cases are defined by several parameters for the simulation of a complete model of a wind turbine that covers the monopile, geotechnical conditions, and the turbine itself. Such parameters include wind, waves, and sea currents conditions in addition to the water level and partial safety factors.

Given the environmental conditions at the reference project site, load cases and the extreme internal responses (shear, normal force, bending, and torsion) are obtained at the interface level. Following, they are used as input and external loads for the simplified model that analyses only the transition piece. The extreme bending moment and extreme torsional moment are obtained at the power production design situation in an extremely coherent gust with direction change, which corresponds to the design load case 1.4 [23].

The extreme normal force is developed also at the power production but in extreme turbulence, which corresponds to the design load case 1.3. Finally, the extreme shear force is obtained at power production with a control system fault or loss of the electrical network, which refers to load case 2.1. In all cases, a partial safety factor of 1.35 is considered, except for the extreme normal force, where no safety factor is used. Further descriptions of each one of these load cases may be found at IEC 61400-1-3 [23]. Table 9 summarizes the loads for the ULS analysis.

Table 9: ULS extreme load values and load cases at 17 m from the lowest astronomical tide (LAT).

Load	DLC	Value	Unit
Shear force (F_y)	2.1	3406	kN
Normal force (F_z)	1.3	-16385	kN
Torsional moment (M_z)	1.4	-33737	kNm
Bending moment (M_x)	1.4	474000	kNm

In the case of the FLS loads, damage equivalent loads (DELs) are considered. The DEL is frequently used in wind farm studies and it corresponds to a single load level with a given number of load cycles that results in the same damage as the original load cycles set with different amplitudes [24]. Furthermore, no normal load is considered in the set of DEL, as they do not present a critical cyclic behaviour. Additionally, as the stress range is in tension the cracks grow faster and the compressive loads actually would help to close them.

Table 10: FLS loads - Damage equivalent loads for 10^7 stress cycles and $m = 5$.

Load	Value	Unit
Equivalent bending moment	71707	kNm
Equivalent shear force	872	kN
Equivalent torsional moment	26541	kNm

Important to point out that whether in the ULS or FLS study, a hypothesis of perfect load transfer between consecutive cans is considered. In other words, for the analytical estimation of the stresses, the welded junctions are able to ideally transfer the loads between cans without any stress jump other than the stress concentration factors appraised in the FLS calculation.

4.2. Global stress assessment

In a more detailed analysis of the substructure with a pile foundation fixed to the seabed, the soil-pile interaction may be taken into account using different methods. One of them

relies on using linear elastic springs that provide stiffness at the end of the monopile. This stiffness property ought to be carefully selected according to the geotechnical data (Figure 14). However, in this project, the monopile itself is not assessed and the hypothesis of a fixed boundary condition at the grouted connection between the monopile and the transition piece is applied because one considers that this region is relatively far from the soil and it can be considered as a zero relative rotation region due to the stiff grout connection. This hypothesis is considered for the analysis of the transition piece stress distribution.

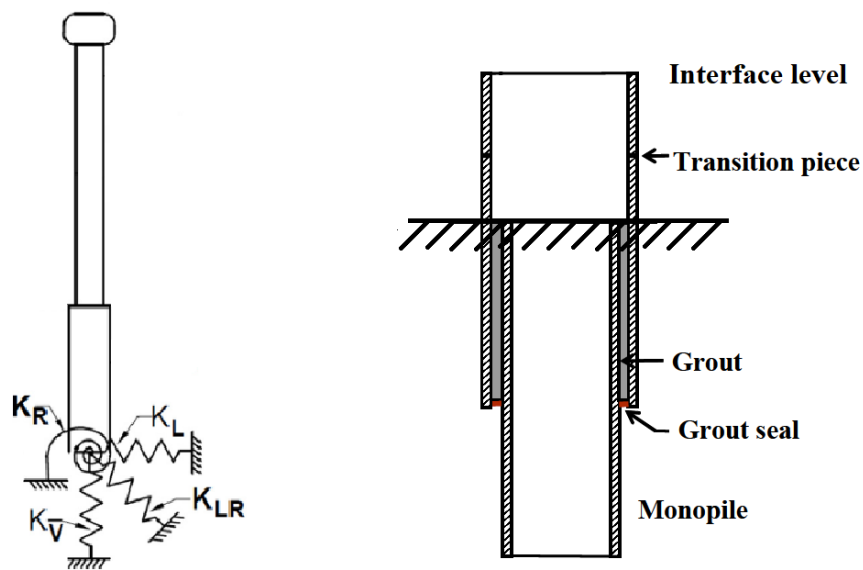


Figure 14: In the left, a soil model of boundary conditions using linear springs. On the right, the simplified model considered [25].

Therefore, a simplified model is used to evaluate the global stresses which will be inputs for the analytical calculation of the limit states. This model uses the loads in Table 9 and in Table 10 for ULS calculation and FLS calculation, respectively. However, the results presented in this section are taken from the load condition of the ULS case, as shown in Table 9.

Moreover, the model considers only the transition piece with a clamped end at the grouted connection and a free end at the interface level, as illustrated in Figure 15. In other words, this means to say that the grouted connection fully transfers the loads in the MP-TP interface. On top of that, although the proposed designs present conical shapes, the cross-sections considered throughout the analytical calculation are simply hollow circles with variable diameters and thicknesses along the longitudinal direction z due to the different cans that compose the transition part.

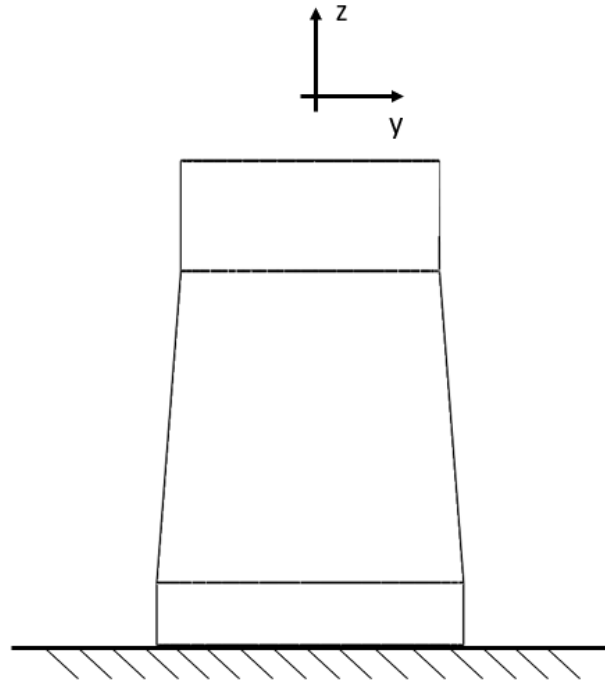


Figure 15: Clamped transition piece model. The total length is the same for all three proposed designs and it is equal to 11 metres.

Given the ULS loads for a specific site as in Table 9, the diagram in Figure 16 is considered.

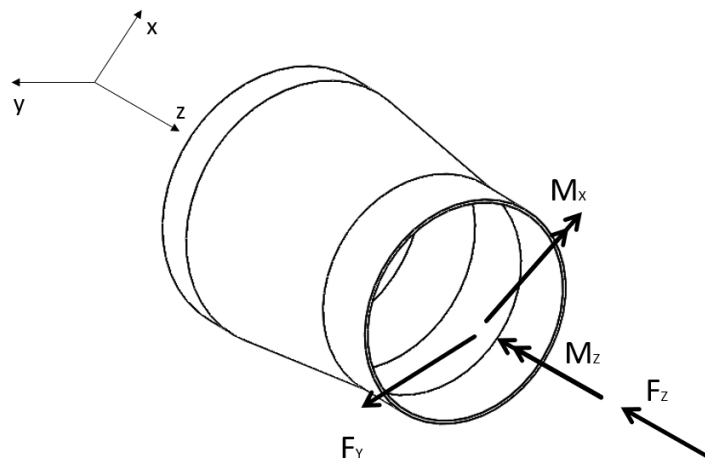


Figure 16: Forces and moments application.

The first step in order to determine the stress distribution along the components of the transition piece is to find the internal loads generated. The load condition described in Figure 16 and load values from Table 9 originate a bending moment, a shear force, a normal force, and a torsion distribution, as illustrated in diagrams from Figure 17 to Figure 20.

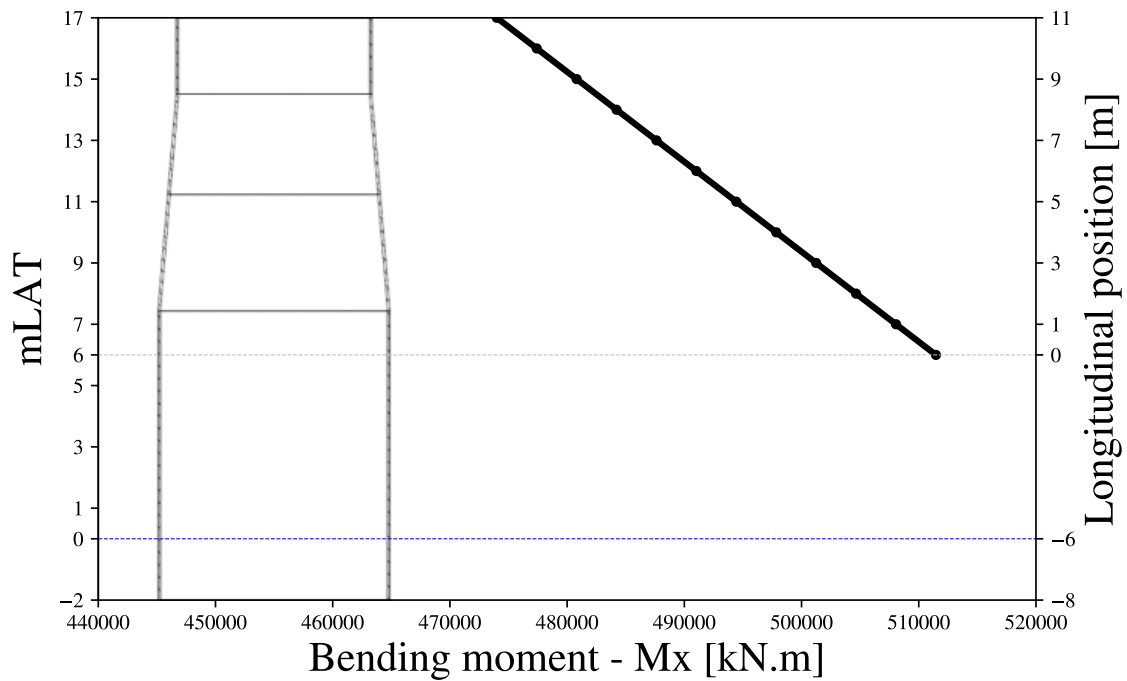


Figure 17: Bending moment distribution. Values go from 474000 kNm at the interface with the tower (17 mLAT) up to 511466 kNm at the MP-TP interface (grey horizontal line). The blue line is the LAT. The plot range starts at 440000 kNm.

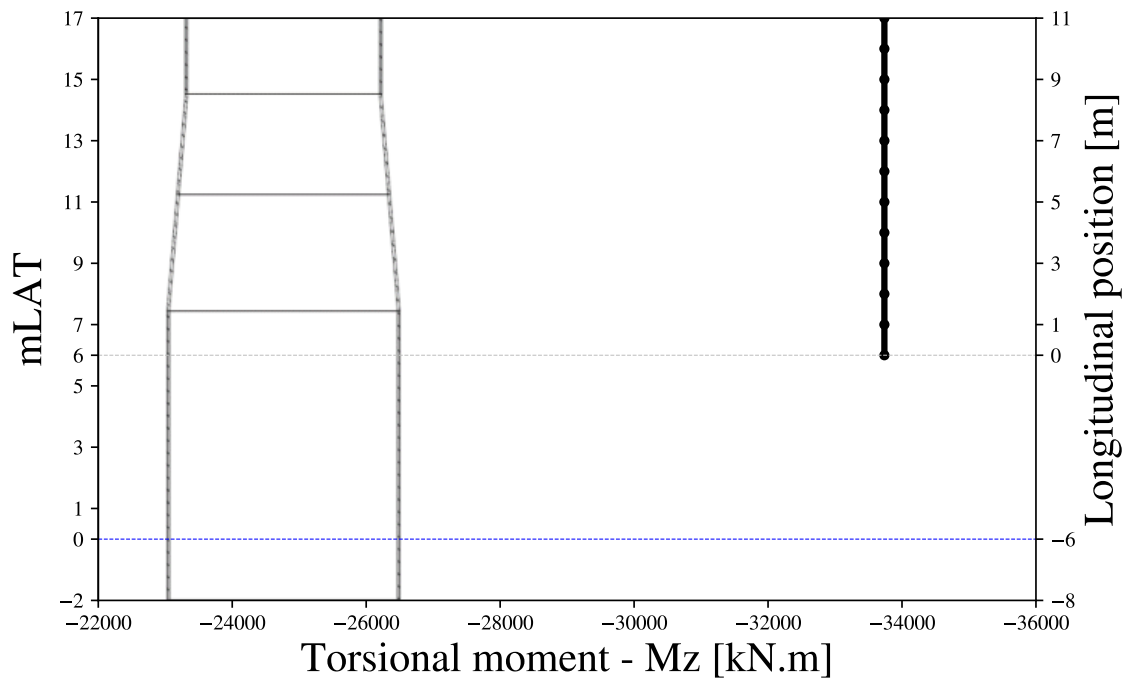


Figure 18: Torsional moment distribution. A constant value of -33737 kNm along the transition piece. The plot range starts at -220000 kNm.

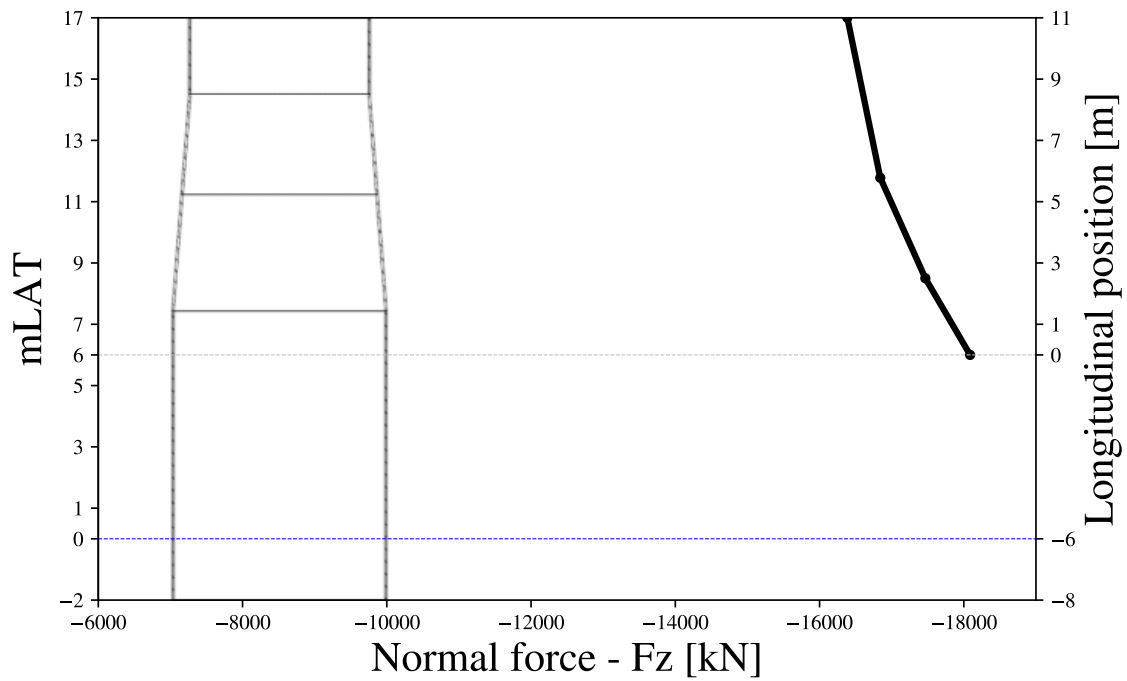


Figure 19: Normal force distribution. Values go from -16385 kN at the interface with the tower (17 mLAT) up to -18139 kN at the MP-TP interface (grey horizontal line). This diagram takes into account the self-weight of the cans of Design 1. The plot range starts at -6000kN.

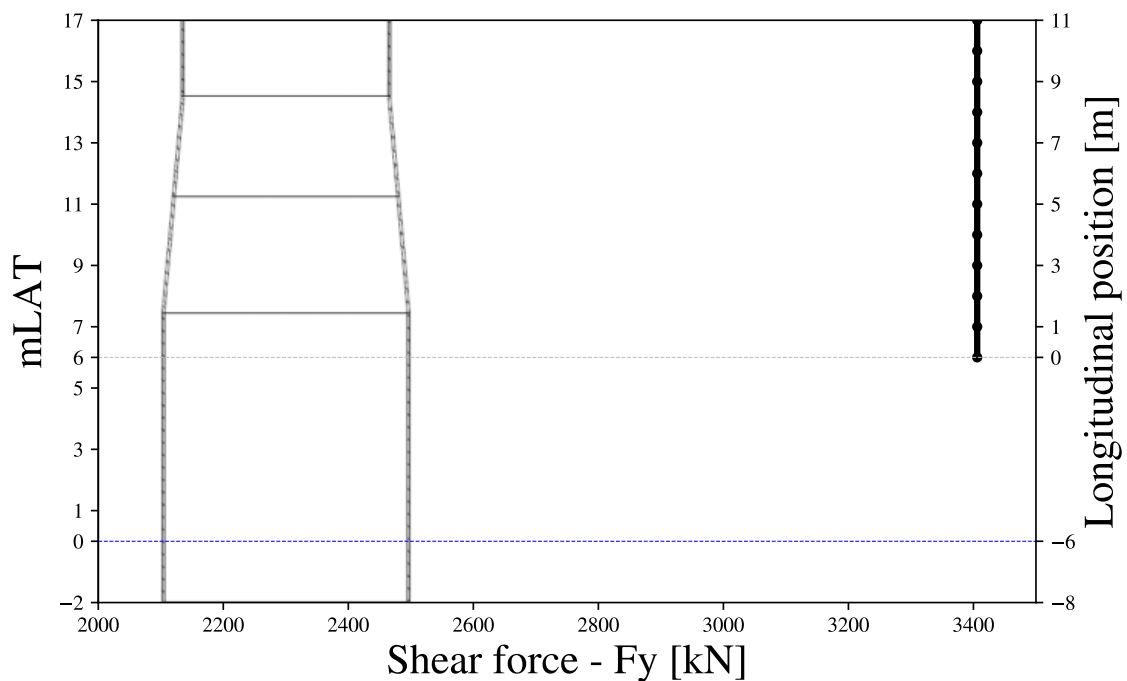


Figure 20: Shear force distribution in Design 1. A constant value of 3406 kN along the transition piece. The plot range starts at 2000 kN.

As shown in Figure 17, the bending moment is composed of a constant value that comes from the interface bending moment M_x and a variable bending moment in the same direction, here called M'_x . This moment is generated by the interface lateral force F_y . The torsion, and shear force, nonetheless, are constant along the transition piece length. In addition, Figure 19 shows the effect of the self-weight of the cans as the bottom cans have to carry more vertical loads. The normal force plot is the only one that is different depending on the design because each one of the designs presented at section 3 has a distinct weight. Figure 19 illustrates the plot for Design 1, however, the curve shape will be similar to all the others.

Moreover, each one of these loads produces different stress components along the transition piece. Table 11 summarizes and relates the stresses with the correspondent loads.

Table 11: Load condition and respective stress generated.

Load	Generated stress
M_x	σ_z
F_y	τ_{yz} and σ_z
M_z	τ_{yz}
F_z	σ_z

Once again, this table only represents the stresses that will be generated by the loads used as boundary conditions for the ULS study. The DEL, as presented in Table 10, will also generate similar types of stresses but of different magnitudes.

Regarding the bending moment (M_x and M'_x) and the lateral force (F_y) imposed at $L = 11$ m, this model suggests the use of the Euler–Bernoulli beam theory. This theory establishes a relationship between the external load applied and the deflection of the cross-section. Some hypotheses are considered in order to properly hold this situation in the context of the Euler-Bernoulli theory. They include a small deflection hypothesis, an isotropic and homogeneous material behaviour, the cross-section remaining plane, the structure remaining in the elastic domain under the applied loads, and finally, one considers a slender beam.

From the static equilibrium of a piece dA of the section (Equation 4), the constitutive relation (Equation 5), and considering the kinematic compatibility (Equation 6), Equation 7, Equation 8, and Equation 9 are obtained.

$$M = \int_A \sigma y dA \quad (4)$$

$$\epsilon = -y\omega''(z) \quad (5)$$

$$\sigma = E\epsilon \quad (6)$$

$$M(z) = EI\omega^{ii}(z) \quad (7)$$

$$Q(z) = -EI\omega^{iii}(z) \quad (8)$$

$$q(z) = -EI\omega^{iv}(z) \quad (9)$$

Where $M(z)$ is the bending moment distribution along the longitudinal coordinate, $Q(z)$ is the shear force distribution along the same coordinate, and $q(z)$ is the lateral force along the z -direction. Moreover, σ is the normal stress generated by the correspondent bending moment, y is the distance from the centre of the piece dA to the reference axis along the y -direction, ϵ is the strain, ω is the lateral deflection produced by the bending moment, E is the Young's Modulus and I is the second moment of area of the cross-section.

Therefore, the shear force distribution is the integral of the lateral forces along the beam length and the bending moment distribution is given by the integral of the shear force along the length. Finally, the normal stress due to bending is expressed as in Equation 10. As Table 11 shows, F_y , M_x and F_z produce normal stress σ_z . In the case of F_y this normal stress appears due to the bending moment M'_x that this force induces and that is simply the product of the force by the distance to the clamped end. Ultimately, the total normal stress is given by Equation 12.

$$\sigma_{z_M}(r, z) = \frac{(M_x(z) + M'_x(z))r}{I} \quad (10)$$

$$\sigma_{z_N}(z) = \frac{F_z(z)}{A} \quad (11)$$

$$\sigma_z(r, z) = \sigma_{z_M}(r, z) + \sigma_{z_N}(z) \quad (12)$$

So, the total normal stress is a function of the longitudinal position z and the radius r . In that sense, it is expected that the maximum value will occur at the external radius (or diameter) along the length of the transition piece.

On the other hand, the lateral force F_y and the torsion moment M_z produce shear stresses, as presented in Table 11. The expression for the shear stress produced by the torsion moment in a closed profile is given by Equation 13 and it is a straightforward result from the torsion theory where the material is subject to twisting and no warping is considered.

$$\tau_{yz_T}(r) = \frac{M_z r}{J} \quad (13)$$

Where J is the polar moment of inertia. In contrast, the transverse shear stress produced by the lateral force is obtained for the specific case of a thin-walled tube section. The equilibrium of moments of a piece dA of the section results in the Equation 14.

$$\tau_{yz_F}(r) = \frac{F_y S(r)}{I(r)t} \quad (14)$$

$S(r)$ is defined as the first moment of area and it is the product of the cross-section area (A) by the distance to the neutral axis (\bar{y}), as written in Equation 15. The parameter t is the thickness of the can. Considering the closed thin-walled section in Figure 21, two symmetrically placed points located at a mean radius R are defined (P and Q). The shear stress at these points is the same and is given by the Equation 14 evaluated on $r = R$, as demonstrated in Equation 15 and Equation 16.

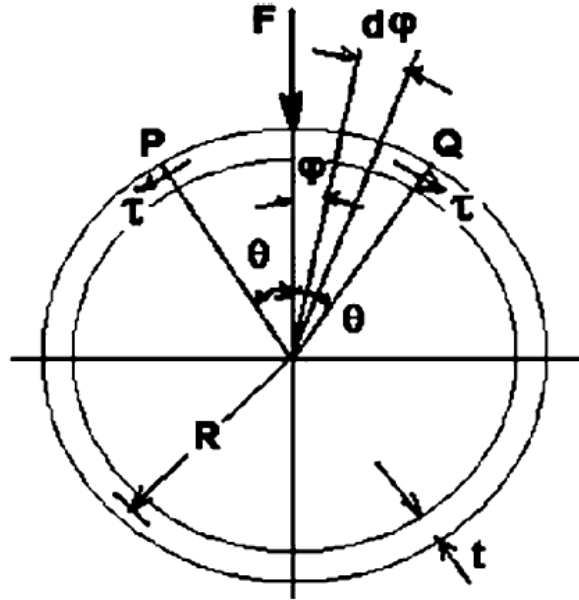


Figure 21: Closed thin-walled section [7].

$$S = A\bar{y} = \int_{-\theta}^{\theta} R t d\phi R \cos \phi = 2R^2 t \sin \theta \quad (15)$$

$$S = \int_0^{2\pi} R t d\phi R^2 \cos^2 \phi = \pi R^3 t \quad (16)$$

The Equation 15 and Equation 16 are evaluated along the angular coordinate ϕ . From the more trivial problem of a rod subject to a force on its end, one knows that the maximum shear stress occurs at the neutral axis. The same will happen with the hollow cylinder, therefore one may assume $\theta = \pi/2$ and $\sin \theta = 1$. Finally, the Equation 17 and the sinusoidal shear distribution illustrated in Figure 22 are found.

$$\tau_{yz.max_F} = \frac{F_y}{\pi R t} \quad (17)$$

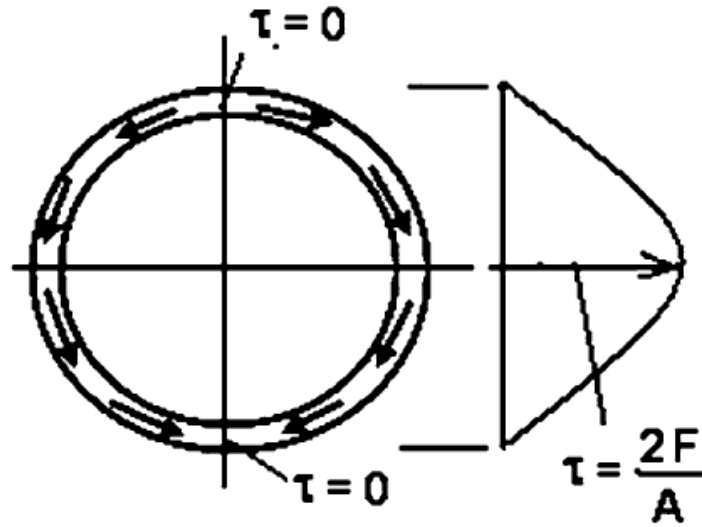


Figure 22: Shear stress sinusoidal distribution and maximum value at the neutral axis [7].

In the end, the maximum total shear is given by the sum of the torsion contribution at the outer diameter (where it is maximum according to Equation 13) and the lateral force contribution, as shown in Equation 18.

$$\tau_{yz_{max}} = \tau_{yz_{max_F}} + \tau_{yz_T} \quad (18)$$

Following that, the stress components are used to obtain the Von Mises stress and its distribution along the longitudinal direction of the transition piece. The specific stress state is considered as shown in Equation 19. Moreover, Table 17 and Table 18 present the results for the junction locations for each one of the designs.

$$\sigma_{VM} = \sqrt{\sigma_z^2 + 3\tau_{yz}^2} \quad (19)$$

This stress analysis is followed using both ULS calculation and FLS calculation. The main difference is regarding the load values and loads that are present on each limit state evaluation, as shown in Table 9 and Table 10. In the case of the ultimate state, this analysis provides the global stresses that are used as input for all the verification done in subsection 4.4. For the fatigue state, the assessment of stresses using the described procedure provides the stress range that is an input for the calculation explained in subsection 4.5.

It is important to mention that the procedure followed to calculate the Von Mises stress considers that the region that suffers more solicitation is not affected by all the induced stresses in Table 11. Although the radial location of the maximum stresses will always be at the external diameter, the circumferential location depends on the loads' magnitude and their induced stresses.

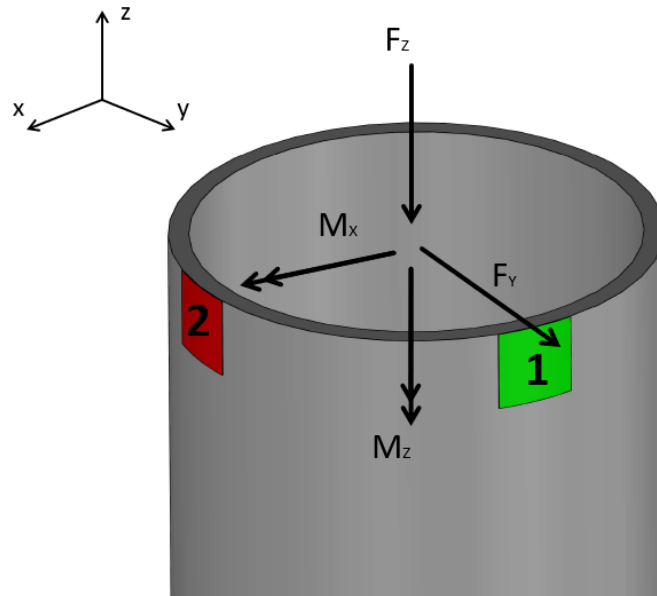


Figure 23: Section of a cylinder with two elements in different circumferential positions.

Figure 23 shows a section of a cylinder with 2 elements highlighted. One of them, element 1, is located along the y -axis, and element 2 is located along the x -axis. Considering a coordinate system in the centre of the cylinder, both pieces are in the positive coordinates of x and y with a magnitude equal to the external radius. The shear stress induced by M_z is the same around the solid. So is it the normal stress induced by F_z .

However, the normal stress induced by M_x goes from zero at element 2 up to its maximum magnitude at element 1. From Equation 4, this is equivalent to saying that element 2 is located at a zero distance from the moment application axis ($y = 0$), whereas element 1 is at the maximum distance, equivalent to the external radius of the cylinder. Moreover, the shear stress induced by F_y varies from zero at element 1 up to its maximum at element 2 as a consequence of what is shown in Figure 22.

Therefore, both elements are affected by the shear stress from torsion and the normal stress from compression, but element 2 is not affected by the normal stress from bending (M_x and also M'_x) and element 1 is not affected by the transversal shear stress from F_y . The regions circumferentially located between them are affected by both induced stresses, but at a lower magnitude depending on the distance to the axis of the moment and shear applications.

In the end, what defines the regions under more loading solicitation and higher Von Mises stress is the comparison between the shear stress induced by F_y and the normal stress induced by M_x and M'_x . In the case of this project, the latter is considerably larger. This indicates that the region of maximum stress is going to be a zone where the normal stress induced by bending is dominant. As Figure 23 illustrates, this region is in the axis of element 1. On top of that, the bending moment generates normal compressive stress on the negative region of the y -axis which sums up the stress from F_z . For this reason, it is

expected that the region of maximum stresses is located at $y = -R_{ext}$ and $x = 0$, where R_{ext} is the external radius.

4.3. Lateral deflection and TPE

Another important result that is assessed analytically is the maximum lateral deflection ω_{max} . Considering Equation 7 it is possible to isolate the second derivative of the lateral deflection as a function of the bending moment, the material and cross-section properties (Equation 20). Moreover, doing a balance of moments one has the Equation 21 as the bending moment distribution along the TP. Therefore, following the Equation 22 to Equation 24 it is possible to obtain an expression for ω and for its maximum value ω_{max} that will occur at $z = L$ (at the free end of the TP).

$$\frac{\partial^2 \omega}{\partial z^2} = \frac{M(z)}{EI} \quad (20)$$

$$M(z) = M_x(z) + F_y(L - z) \quad (21)$$

$$\frac{\partial^2 \omega}{\partial z^2} = \frac{M_x(z) + F_y(L - z)}{EI} \quad (22)$$

$$\omega(z) = \frac{1}{EI} \left(\frac{M_x z^2}{2} + \frac{F_y L z^2}{2} - \frac{F_y z^3}{6} \right) \quad (23)$$

$$\omega_{max} = \frac{1}{6EI} (3M_x L^2 + 3F_y L^3 - L^3) \quad (24)$$

Finally, another critical parameter to be calculated is the total potential energy (TPE). This scalar is important for static problems such as the one studied in this project as it indicates a stable equilibrium condition. Moreover, it will play an important role in the numerical analysis. The TPE is defined in Equation 25 as a function of the strain energy of the system U and the work done by the external forces P .

$$\text{TPE} = \Pi = U - P \quad (25)$$

As a result of Clapeyron's theorem, one may state that the strain energy is half of the work done by the external forces which simplifies the expression of the TPE to Equation 26 which is dependent only on the strain energy [26].

$$\text{TPE} = U - 2U = -U \quad (26)$$

As indicated in Table 11, four loading types are present in the problem. Each one of them produces strain energy [27] as given in Equation 27 to Equation 30.

$$U_{bending} = \int_0^L \frac{M(z)^2}{2EI} dz \quad (27)$$

$$U_{shear} = \frac{F_y^2 L}{2AG} \quad (28)$$

$$U_{torsion} = \frac{M_z^2 L}{2GJ} \quad (29)$$

$$U_{normal} = \frac{F_z^2 L}{2EA} \quad (30)$$

Where G is the shear modulus of the S355 steel, 81 GPa. Finally, using the expression of the bending moment given in Equation 21, one may solve the integral in Equation 27, and the TPE expression in Equation 31 is obtained.

$$TPE = - \left[\frac{F_z^2 L}{2EA} + \frac{1}{2EI} \left(M_x^2 L + 2M_x F_y L^2 + \frac{F_y^2 L^3}{3} \right) + \frac{M_z^2 L}{2GJ} + \frac{F_y^2 L}{2AG} \right] \quad (31)$$

4.4. Ultimate limit state theory

The cross-section properties that allow the calculation of stresses are defined according to the specific design and the z-position (junction considered). Each design has a different can diameter and slope. Moreover, it is located at a given height from the interface between the transition piece and the tower. As a result, the stress distribution along the transition piece will be distinct for each design.

Depending on the connection type, as presented in Table 3 to Table 8, each junction is evaluated with regard to specific requirements that are defined on the DNV-ST-0126 [19]. This rule indicates that tubular connections ought to be checked using the NORSOK N-004 [21] when it comes to bending, axial load, and torsion. Buckling checking, however, has to be done using the DNV-RP-C202 [22] as a reference. In the case of conical connection type, the NORSOK N-004 [21] provides the necessary LRFD calculation.

Initially, a similar thickness is considered for all the cans in all the designs. Moreover, the tubular connections are checked with regard to their structural strength and stability which includes axial compression, local buckling as a shell cylinder, global buckling as a shell column, bending moment, shear force, torsional moment, and the interaction between shear, bending, and torsion. The conical connections, on the other hand, are evaluated in terms of local buckling, junction yielding, and junction buckling, as stated by the NORSOK N-004 [21].

The same calculation is performed for all the junctions of all the proposed designs. All relevant failure modes are identified depending on the type of connection and one needs to check if the limit state is exceeded. Generally, the safety equation is given by the Equation 32.

$$S_d \leq \frac{R_k}{\gamma_M} \quad (32)$$

Where R_k is a characteristic resistance and S_d is a design action effect. First, one defines a yield strength (f_y) equal to 355 MPa corresponding to a S355 structural steel,

and a material factor γ_M of 1.15. Then, the cross-section of each junction is classified according to its ability to develop plastic hinges. Different cross-sectional types are defined depending on the ratio between the external diameter of the junction D and the can thickness t compared with a coefficient related to the relative strain ϵ , as in Equation 33 for cross-section type IV.

$$\frac{D}{t} > 90\epsilon^2 \quad (33)$$

The relative strain ϵ is defined as $\epsilon = \sqrt{235/f_y}$, where f_y is the yield strength.

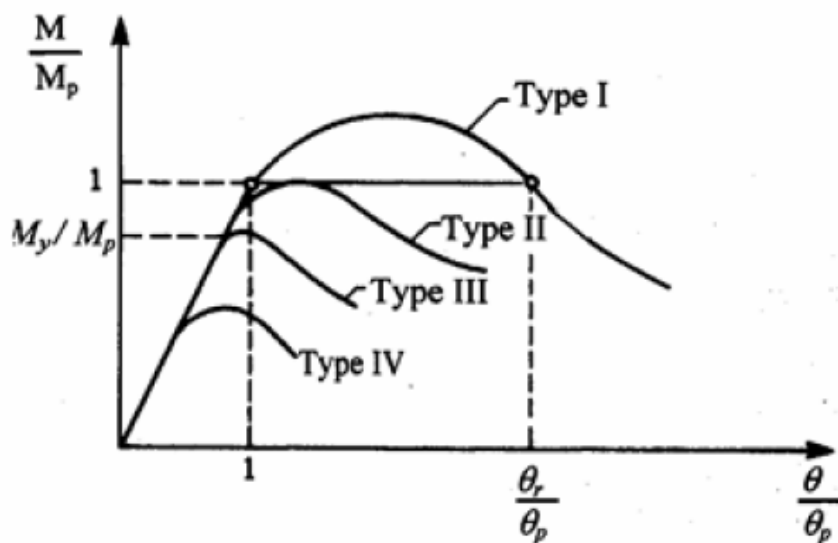


Figure 24: Types of cross-sections according to their ability to develop plastic hinges [19]. The vertical axis is the ratio between the applied moment and the plastic bending moment whereas the horizontal axis corresponds to the ratio between the curvature imposed by the moment and the plastic limit.

All of the cases studied in this project refer to thin-walled cross-section type IV, which means that the local buckling phenomena must be considered as it reduces the strength and stability of the tubular member, as shown in Figure 24. In these cases, failure modes involve combinations of member flexural buckling and local shell buckling [19].

Another important preliminary step is to determine a reduced thickness t_p depending on an expected maximum corrosion rate V_{corr} . This expected corrosion is given by DNV-RP-0416 [28] as equal to 0.3 considering the external surface of a primary structural part in the splash zone in a region of temperate climate. This correction has to be considered as such in the ULS calculations and as half of it in the FLS calculations [28] for the thickness of the conical can (t_c) and for the thickness of the tubular can (t_t). The reduced thickness is calculated as shown in Equation 34.

$$t_p = t - V_{corr}(T_d - T_c) \quad (34)$$

Where T_d is the design life of the structure considered 31.5 years and T_c is the design useful life of the coating, assumed as 20 years which corresponds to a system based on glass-flake reinforced epoxy or polyester in the splash zone [28].

4.4.1. Tubular connections: axial compression

The first aspect to be verified is the axial compression. In this case, the condition is that the design axial force, given in Table 9 as F_x , must be less or equal to the axial compression resistance $N_{c,Rd}$, in kN, defined in Equation 36. This requirement is expressed in Equation 35.

$$F_x \leq N_{c,Rd} \quad (35)$$

$$N_{c,Rd} = \frac{Af_c}{\gamma_M} \quad (36)$$

A is the cross-section area at the junction and f_c is the characteristic axial compressive strength, in MPa. This value is obtained from a set of expressions that depend on the column slenderness parameter $\bar{\lambda}$ as defined in Equation 37.

$$\bar{\lambda} = \frac{kl}{\pi i} \sqrt{\frac{f_{cl}}{E}} \quad (37)$$

k is the effective length factor accounted as 1 for a piling structure, l is the longer unbraced length (assumed as the total length of the can) and i is the radius of gyration which is given by $\sqrt{\frac{I}{A}}$. The parameter f_{cl} is the characteristic local buckling strength and it is determined according to the ratio between the yield strength f_y and the characteristic elastic local buckling strength f_{cle} , as shown in Equation 38 to Equation 41.

$$f_{cl} = f_y \quad \text{for } \frac{f_y}{f_{cle}} \leq 0.170 \quad (38)$$

$$f_{cl} = \left(1.047 - 0.274 \frac{f_y}{f_{cle}}\right) \quad \text{for } 0.170 < \frac{f_y}{f_{cle}} \leq 1.911 \quad (39)$$

$$f_{cl} = f_{cle} \quad \text{for } \frac{f_y}{f_{cle}} > 1.911 \quad (40)$$

$$f_{cle} = 2C_e E \frac{t_p}{D} \quad (41)$$

Where C_e is the critical elastic buckling coefficient assumed as 0.3. From the characteristic local buckling strength f_{cl} found, Equation 37, Equation 42 and Equation 43 are used to obtain the characteristic axial compressive strength f_c .

$$f_c = (1 - 0.28\bar{\lambda}^2)f_y \quad \text{for } \bar{\lambda} \leq 1.34 \quad (42)$$

$$f_c = \frac{0.9}{\bar{\lambda}^2} f_y \quad \text{for } \bar{\lambda} > 1.34 \quad (43)$$

4.4.2. Tubular connections: bending

The second load to be verified is the bending moment. The tubular members should satisfy the condition expressed in Equation 44. This expression simply states that the design bending moment M_x has to be less or equal to the bending moment resistance M_{Rd} . This resistance is defined in Equation 45.

$$M_x \leq M_{Rd} \quad (44)$$

$$M_{Rd} = \frac{f_m W}{\gamma_M} \quad (45)$$

Where f_m is the characteristic bending strength and should be determined from Equation 46 to Equation 48. Moreover, W is the elastic section modulus and Z is the plastic section modulus given by Equation 49 and Equation 50 respectively.

$$f_m = \frac{Z}{W} f_y \quad \text{for } \frac{f_y D}{Et_p} \leq 0.0517 \quad (46)$$

$$f_m = \left[1.13 - 2.58 \left(\frac{f_y D}{Et_p} \right) \right] \left(\frac{Z}{W} \right) f_y \quad \text{for } 0.0517 < \frac{f_y D}{Et_p} \leq 0.1034 \quad (47)$$

$$f_m = \left[0.94 - 0.76 \left(\frac{f_y D}{Et_p} \right) \right] \left(\frac{Z}{W} \right) f_y \quad \text{for } 0.1034 < \frac{f_y D}{Et_p} \leq \frac{120 f_y}{E} \quad (48)$$

$$W = \frac{\pi[D^4 - (D - 2t_p)^4]}{32D} \quad (49)$$

$$Z = \frac{D^3 - (D - 2t_p)^3}{6} \quad (50)$$

4.4.3. Tubular connections: shear

Next, the shear loads are also evaluated following the same safety criteria expressed in Equation 32. Two loads are assessed separately: the shear force (a condition in Equation 51 must be satisfied) and the torsional moment (a condition in Equation 52 must be satisfied).

$$F_y \leq V_{Rd} \quad (51)$$

$$M_z \leq M_{T,Rd} \quad (52)$$

The shear force resistance V_{Rd} and the torsional moment resistance $M_{T,Rd}$ are defined in Equation 53 and Equation 54, respectively. Moreover, J is the polar moment of inertia given by Equation 55.

$$V_{Rd} = \frac{A f_y}{2\sqrt{3}\gamma_M} \quad (53)$$

$$M_{T,Rd} = \frac{2J f_y}{D\sqrt{3}\gamma_M} \quad (54)$$

$$J = \frac{\pi[D^4 - (D - 2t_p)^4]}{32} \quad (55)$$

4.4.4. Tubular connections: loads interaction

An additional criterion is studied in the context of the NORSOK N-004 [21] which is regarding the interaction of the shear force, bending moment, and torsion in tubular connections. The condition to be satisfied is expressed in Equation 56 and Equation 57 depending on the ratio between the design shear force F_y and the shear force resistance V_{Rd} .

$$\frac{M_x}{M_{Red,Rd}} \leq \sqrt{1.4 - \frac{F_y}{V_{Rd}}} \quad \text{for } \frac{F_y}{V_{Rd}} \geq 0.4 \quad (56)$$

$$\frac{M_x}{M_{Red,Rd}} \leq 1.0 \quad \text{for } \frac{F_y}{V_{Rd}} < 0.4 \quad (57)$$

$M_{Red,Rd}$ is the reduced design bending moment resistance due to the torsional moment and it is calculated through to Equation 58 as a function of the reduced bending strength due to torsional moment (Equation 59) and the shear stress due to design torsional moment (Equation 60).

$$M_{Red,Rd} = \frac{W f_{m,Red}}{\gamma_M} \quad (58)$$

$$f_{m,Red} = \sqrt{1 - 3 \left(\frac{\tau_{T,Sd}}{f_d} \right)^2} \quad (59)$$

$$\tau_{T,Sd} = \frac{M_z}{2\pi R^2 t_p} \quad (60)$$

Where R is the radius of the tubular member and f_d is the design yield strength defined as $\frac{f_y}{\gamma_M}$.

4.4.5. Tubular connections: buckling as shell cylinder and as shell column

The buckling study is performed in accordance with the DNV-RP-C202 [22]. This recommended practice deals with the buckling stability of shell structures. According to the rules, a tubular structure may behave as a shell if $\frac{f_y}{f_{cle}} > 0.170$.

In this project that is the case of every junction of all the designs proposed. Therefore, the approach presented by the recommended practice is followed. In the case of unstiffened cylindrical shells, two buckling modes have to be verified. The first mode is the shell buckling which refers to the local buckling of the shell plating between the longitudinal divisions, the junctions. The second mode is the column buckling which refers to the overall buckling of the structure. Figure 25 illustrates both of them.

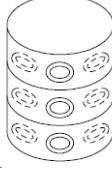
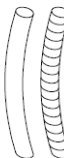
<i>Buckling mode</i>	<i>Type of structure geometry</i>
	<i>Ring stiffened (unstiffened circular)</i>
a) Shell buckling	 Section 3.4
e) Column buckling	 Section 3.8

Figure 25: Buckling modes to be verified [22].

The general stability requirement for shells is given by Equation 61 and f_{ksd} is the design shell buckling strength. The stress $\sigma_{j,Sd}$ is the Von Mises stress calculated as shown in Equation 19, for the case where there is no internal pressure.

$$\sigma_{j,Sd} \leq f_{ksd} \quad (61)$$

Moreover, the design shell buckling strength is obtained from the characteristic buckling strength f_{ks} (Equation 62) and a parameter $\bar{\lambda}_s$ (Equation 63). This parameter is a function of the elastic buckling strength for each one of the loads to which the structure is subject ($f_{E,N}$, $f_{E,M}$ and $f_{E,\tau}$ in Equation 64). More details of the calculation of these parameters may be found in DNV-RP-C202 [22].

$$f_{ksd} = \frac{f_{ks}}{\gamma_M} \quad (62)$$

$$f_{ks} = \frac{f_y}{\sqrt{1 + \bar{\lambda}_s^4}} \quad (63)$$

$$\bar{\lambda}_s^2 = \frac{f_y}{\sigma_{j,Sd}} \left[\frac{\sigma_{zN}}{f_{E,N}} + \frac{\sigma_{zM}}{f_{E,M}} + \frac{\tau_{zx}}{f_{E,\tau}} \right] \quad (64)$$

The second buckling mode to be evaluated is the overall column buckling. However, according to the DNV RP-C202 [22] this stability requirement should be assessed only if the Equation 65 is true. For all the cases in this project, this is not the case and, therefore, it is not expected to observe a column buckling behaviour in the structure as for the

proposed designs and given load conditions.

$$\left(\frac{kl}{i_c}\right)^2 \geq 2.5 \frac{E}{f_y} \quad (65)$$

4.4.6. Conical connections

The ultimate limit state of the conical connections is assessed by means of the NORSOK N-004 [21]. The local buckling, the junction yielding, and the junction buckling are studied. Firstly, the standard suggests the characterization of a cone side and a tubular side, as illustrated in Figure 26. All the following calculation at the junction has to be done both for the tubular side element and the conical side element. This is important, especially for cases where the junction has elements with different thicknesses. Further, the standard indicates the calculation of the equivalent design axial stress within the conical transition $\sigma_{equ,Sd}$ as a function of global actions at the junction, as shown from Equation 66 to Equation 68. These equations refer to the conical side. In order to calculate the tubular side, one replaces the thickness accordingly.

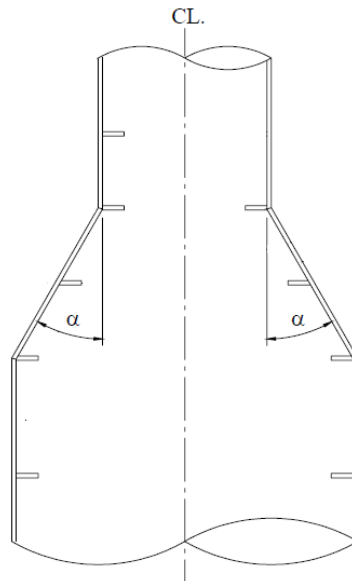


Figure 26: Cone geometry is composed of two tubular parts (straight) and a conical side (inclined at the slope α). This picture shows stiffeners along the conical region, but this project deals with an unstiffened structure [8].

$$\sigma_{ac,Sd} = \frac{F_z}{\pi(D - t_c \cos \alpha)t_c} \quad (66)$$

$$\sigma_{mc,Sd} = \frac{M_x}{\frac{\pi}{4}(D - t_c \cos \alpha)^2 t_c} \quad (67)$$

$$\sigma_{equ,Sd} = \frac{\sigma_{ac,Sd} + \sigma_{mc,Sd}}{\cos \alpha} \quad (68)$$

Where, $\sigma_{ac,Sd}$ is the design axial stress at the section within the cone due to global loads, $\sigma_{mc,Sd}$ is the design bending stress at the section within the cone due to global loads, t_c is the thickness of the cone element and α is the cone slope. These global load stresses are calculated as explained in subsection 4.2. Another set of stresses that need to be computed is the local bending stresses, which are given by the Equation 69 and Equation 70 for the tubular and cone sides, respectively.

$$\sigma_{mt,Sd} = \frac{0.6t_t\sqrt{D(t_t + t_c)}}{t_t^2}(\sigma_{z_N} + \sigma_{z_M}) \tan \alpha \quad (69)$$

$$\sigma_{mlc,Sd} = \frac{0.6t_t\sqrt{D(t_t + t_c)}}{t_c^2}(\sigma_{z_N} + \sigma_{z_M}) \tan \alpha \quad (70)$$

Where σ_{z_N} is the normal stress from compression and σ_{z_M} is the normal stress from bending. Finally, the hoop stress at the junction is also calculated. Although no pressure deviation between the inside and outside of the transition piece is considered, this component of stress is present due to unbalanced radial line forces and it is estimated as a function of σ_{z_N} and σ_{z_M} in Equation 71.

$$\sigma_{hc,Sd} = 0.45\sqrt{\frac{D}{t_t}}(\sigma_{z_N} + \sigma_{z_M}) \tan \alpha \quad (71)$$

The next step is to verify the strength requirements at the conical transition. The local buckling under axial compression and bending is verified as well as the junction yielding. On top of that, as the hoop stress is found to be compressive, the standard also requires another junction buckling check. In the case of the local buckling, the criteria follows the general safety expression in Equation 32, as Equation 72 shows.

$$\sigma_{equ,Sd} \leq \frac{f_{clc}}{\gamma_M} \quad (72)$$

Where f_{clc} is the local buckling strength of the conical transition and it is calculated using the Equation 38 to Equation 41 with an equivalent diameter equals to $\frac{D}{\cos \alpha}$.

The junction yielding establishes the Equation 73 as criteria to be respected, where the total design stress $\sigma_{tot,Sd}$ is the sum of the design axial stress (Equation 66), the design bending stress (Equation 67) and the local bending stress (Equation 70 and Equation 69).

$$\sqrt{\sigma_{tot,Sd}^2 + \sigma_{hc,Sd}^2 + \sigma_{hc,Sd}|\sigma_{tot,Sd}|} \leq \frac{f_y}{\gamma_M} \quad (73)$$

Finally, in the case of the junction buckling check due to compressive hoop stress, the

two expressions in Equation 74 and Equation 75 must be respected.

$$\sigma_{tot,Sd} \leq \frac{f_{cl}}{\gamma_M} \quad (74)$$

$$\sigma_{hc,Sd} \leq \frac{f_h}{\gamma_M} \quad (75)$$

Where f_h is the characteristic hoop buckling strength, calculated with a similar approach as the one used in Equation 38 to Equation 41 using the elastic hoop buckling strength for tubular section (f_{he}) equals to $0.8E(t_t/D)^2$.

The summary of results of the LRFD calculation is presented in subsection 4.6 and the full result including the intermediate parameter values is found in Appendix B.

4.5. Fatigue limit state theory

The fatigue design aims to ensure that the structure resists cumulative damage due to cyclic loads. In that sense, the fatigue limit state (FLS) corresponds to failure due to dynamic loading [19]. This analysis has to be carried out for each individual member of the structure and takes into account sources of fatigue cracking such as forms of stress concentration. In most cases, the fatigue assessment is determinant to define acceptable dimensions of a MP or TP design. The final goal is to obtain a minimum thickness taking into account the corrosion allowance as in Equation 34.

Two norms are used to evaluate the FLS. The DNV-RP-C203 [8] and the DNV-ST-0126 [19]. In general, they present principles, requirements, acceptance criteria, and recommendations for analysis based on fatigue tests of steel materials. In this project, the fatigue analysis is done based on the S-N curve and the given damage equivalent loads (DEL) at the interface level.

As mentioned in subsection 4.4 and shown in Equation 34, the corrosion allowance shall be considered in the structural design for all limit state analyses by appropriate reduction of nominal thicknesses [28]. Therefore, all the FLS assessment is done considering the reduced thickness of the tubular and conical cans. However, in the case of the fatigue calculations, according to DNV-ST-0126 [19], the nominal thickness is reduced by half the corrosion allowance, which means that V_{corr} is assumed as 0.15 for the computation done in this section.

The procedure starts with the calculation of the stress concentration factors (SCFs) at each junction and element. Moreover, using the equivalent loads, the nominal stress is calculated by following the steps described in subsection 4.2. After that, the results are applied to the SCFs in order to obtain the hot spot stress range, as Equation 76 shows.

$$\sigma_{hotspot} = SCF \sigma_{nominal} \quad (76)$$

The SCF is calculated according to the type of junction. Moreover, the thickness transitions and eccentricities are also taken into account. For each junction two SCFs are obtained, one for each component.

4.5.1. Stress concentration factors

The SCF quantifies the increment in the nominal stress due to the geometrical features of the structure. In this project, some junctions represent an important region of stress concentration due to the slope and/or change in thickness between consecutive cans. In order to calculate the SCFs, once again, the junctions are divided into tubular and conical connections.

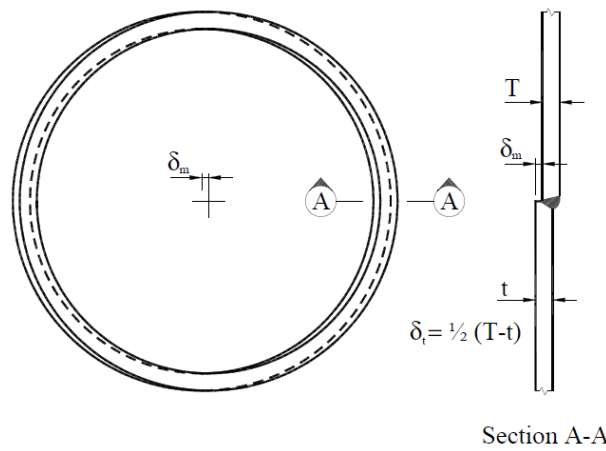


Figure 27: Sources of stress concentrations in tubular connections. δ_0 is a misalignment inherent in the S-N data, δ_m is the maximum misalignment and δ_t is the eccentricity due to change in thickness [8].

The tubular connections link cans by means of circumferential butt welding. The SCF in this type of junction is given by Equation 77. This formula takes into account different sources of local stress concentrations as shown in Figure 27.

$$SCF_{tub} = 1 + \frac{6(\delta_t + \delta_m - \delta_0)}{t} \frac{1}{1 + \left(\frac{T}{t}\right)^\beta} e^{-\xi} \quad (77)$$

In Equation 77, t is the smaller thickness, T is the greater thickness of the junction, and the parameters ξ and β are given by the Equation 78 and Equation 79.

$$\xi = \frac{1.82L}{\sqrt{Dt}} \frac{1}{1 + \left(\frac{T}{t}\right)^\beta} \quad (78)$$

$$\beta = 1.5 - \frac{1.0}{\log\left(\frac{D}{t}\right)} + \frac{3.0}{\left[\log\left(\frac{D}{t}\right)\right]^2} \quad (79)$$

Where L is the width of the weld at the surface given by half of the sum of the thickness

of consecutive cans, and D is the diameter at the junction. Important to highlight that, per junction, two SCFs are calculated for each can. One for the inner diameter and one for the outer diameter. However, in the end, just the most critical case is considered which is mostly the outer diameter concentration factor.

The SCF of unstiffened conical-tubular connections is estimated using Equation 80 for the tubular side element, and Equation 81 for the conical side element. Figure 28 illustrates the parameters in the equations.

$$SCF_{cone1} = 1 + \frac{0.6t_t\sqrt{D(t_t + t_c)}}{t_t^2} \tan \alpha \quad (80)$$

$$SCF_{cone2} = 1 + \frac{0.6t_t\sqrt{D(t_t + t_c)}}{t_c^2} \tan \alpha \quad (81)$$

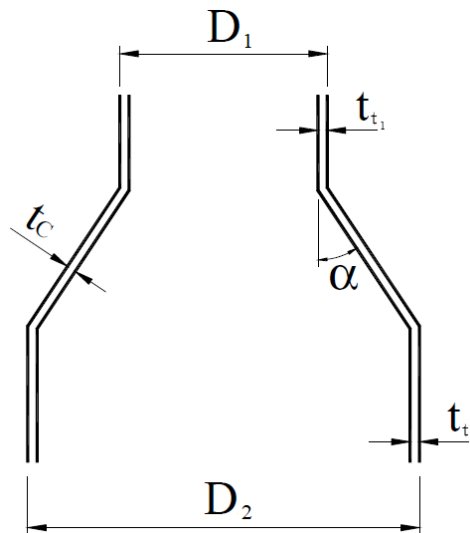


Figure 28: Parameters of the conical-tubular connections. Adapted from [8].

4.5.2. S-N curve

Next, a modified S-N curve is introduced according to Equation 82.

$$\log N = \log \bar{a} - m \log \left[\Delta \sigma \left(\frac{t_p}{t_{ref}} \right)^k \right] \quad (82)$$

This equation is a modification of the basic S-N curve that considers the thickness effect. N refers to the fatigue life, in cycles, for a given stress range, $\log \bar{a}$ and m are obtained through the S-N curve T, which is the one indicated for tubular joints and the conical transitions. Additionally, t_p is the reduced thickness (Equation 34) through which a crack will most likely grow, and t_{ref} is the reference thickness that is equal to 32 mm for the welded tubular and conical connections [8]. The curve and tables are fully presented in

Appendix B.

Moreover, $\Delta\sigma$ is a hot spot stress range which is a direct result of the Equation 76 applied to a nominal stress range. In that sense, this stress range has to be calculated in order to solve Equation 82. The approach is to consider a set of DELs shown in Table 10 related to a specific site condition and taken at the interface level (17 mLAT).

The DELs are used to calculate the nominal stress by means of the Euler-Bernoulli theory just like the procedure followed in the calculation of the stress at the junctions and presented in subsection 4.1. The resulting Von Mises stress obtained is considered the upper bound of the stress range and zero is the lower bound.

Following the calculation of the fatigue life, in cycles, one applies Miner's rule (Equation 83) to obtain the cumulative damage D . In addition to being smaller than 1, this damage has to respect the Equation 85 when compared with a usage factor η as defined in Equation 84.

$$D = \frac{n}{N} \quad (83)$$

$$\eta = \frac{1}{DFF} \quad (84)$$

$$D < \eta \quad (85)$$

Where n is the number of stress cycles, assumed as 10^7 and DFF is the design fatigue factor. Considering the location of the transition piece at an upper splash zone DFF is equal to 3 [8]. Furthermore, a calculated fatigue life L_c , in years, is also obtained from the theoretical fatigue life L_t , in years, and the cumulative damage D , according to Equation 86. In this project $L_t = 31.5$ years.

$$L_c = \frac{L_t}{D} \quad (86)$$

The results of the FLS calculation are presented in subsection 4.6 and the intermediate findings may be found in Appendix B.

4.6. Analytical results

4.6.1. Minimum thickness

In order to perform the calculations presented in subsection 4.4 and subsection 4.5, some spreadsheets were prepared. As previously stated, the main goal of the analytical calculation is to find the minimum thickness that would satisfy all the requirements. With that in mind, this first analysis provided an important result for the following studies. As explained and shown below, the minimum thickness assessment resulted in the phasing out of Design 2 as a feasible structure due to manufacturing limitations.

Initially, an identical thickness is assigned to all the cans. From that, each can thickness

is fine-tuned until all the ULS and FLS requirements are fulfilled. That being the case, the FLS criteria proved to be dominant in most of the cans.

Table 12 from Table 14 show the minimum thickness for the cans in order to pass all ULS and FLS requirements in addition to the final thicknesses selected. This final thickness is assumed using two conditions mentioned in section 2 that restrain the manufacturing and welding of the cans together. The first one is the maximum thickness of 140 mm for each can and the second one is a maximum thickness jump of 20 mm for consecutive cans.

Table 12: Design 1 minimum can thickness to pass all ULS and FLS criteria, in mm.

Design 1			
Can	Min. thickness - ULS	Min. thickness - FLS	Final thickness
top_can	90	104	104
can_1	80	104	104
can_2	69	82	84
bottom_can	69	79	79

From the ULS results of Design 1, the more critical criterion is found to be the yielding at the conical junctions. At the top of the TP, the normal stresses arising from the bending moment and the normal force are greater than the same type of stresses at lower LAT. This happens due to the fact that the diameter at the top is smaller which results in a smaller cross-section area. Moreover, regarding the conical yielding check, the major contribution comes exactly from the normal stresses, as they contribute to the hoop stress $\sigma_{hc,Sd}$ and to the total design stress $\sigma_{tot,Sd}$, as shown in Equation 73 and Equation 71, respectively.

When it comes to the minimum thickness from the FLS study, the conical slope promotes an increment in the SCF at Junction 1 (top_can + can_1) and Junction 3 (can_2 + bottom_can). On top of that, the hot spot stress range is higher at the top resulting in thicker cans in this region. In the end, the final thicknesses selected for top_can, can_1, and bottom_can are the same as the minimum in FLS, but for can_2 there is an increment from 82 mm to 84 mm due to the need for 20 mm thickness clearance from can_1.

Table 13: Design 2 minimum can thickness to pass all ULS and FLS criteria, in mm.

Design 2			
Can	Min. thickness - ULS	Min. thickness - FLS	Final thickness
top_can	68	88	114
can_1	110	125	134
can_2	120	125	147
can_3	146	117	167
can_4	122	187	187
bottom_can	117	131	167

In the second design, shown in Table 13, the top_can is able to carry the loads with a quite small thickness because it is welded to the can_1 as a tubular connection. This type of connection reveals itself not as critical as it is in the case of conical connections at the top, especially for ULS. Moreover, the can_3 is a crucial element in the design. By the ULS calculation, its required thickness is the largest among all the cans, even larger than the FLS thickness for the same component, and the reason for that may rely on the fact that this can, whilst not inclined, is located between two conical connections with increasing slopes. Comparing the thickness of can_2 and can_4 one can notice that the greater the slope, the thicker the can has to be in terms of ULS requirement. This happens because the slope contributes to the increment of design axial stress $\sigma_{ac,Sd}$ (Equation 66), the design bending stress $\sigma_{mc,Sd}$ (Equation 67), the local bending stress $\sigma_{mlc,Sd}$ (Equation 70) and, consequently, the total design stress $\sigma_{tot,Sd}$.

In the case of the required thickness due to the FLS, the most critical feature turns out to be the slope of the can. Once again, the slope contributes to the increase of stresses, this time by means of the SCF, especially in can_4 which presents an extremely high slope. The final thickness is determined for each can using can_4 as a starting point and following a fine-tuning respecting the manufacturing limits.

Table 14: Design 3 minimum can thickness to pass all ULS and FLS criteria, in mm.

Design 3				
Can	Min. thickness - ULS	Min. thickness - FLS	Final thickness	
top_can	79	98	98	
can_1	79	98	98	
collar	75	73	78	
can_2	75	71	75	
bottom_can	66	68	68	

Finally, the third design minimum thickness requirement presents a similar rationale as Design 1, as shown in Table 14. The cans in the upper region of the TP require a greater thickness to comply with the ULS criteria. Nonetheless, one may point out that the collar and can_2 present a more critical result in terms of ULS than FLS. However, important to mention that the FLS is evaluated only in terms of the junctions. Depending on the way this collar is designed and manufactured, its geometry may create other stress concentration regions and this should be evaluated. Still, the thickness required is relatively thin. This happens due to the fact that the collar is not part of any conical junction but it is linked by means of tubular junctions with can_1 and can_2.

Table 15 presents the mass of Design 1, Design 2 and Design 3 based on these final thicknesses assumed as in Table 12 to Table 14.

Table 15: The total mass of each design, in tonnes.

Design 1		Design 2		Design 3	
Component	Mass [ton]	Component	Mass [ton]	Component	Mass [ton]
top_can	47.42	top_can	51.91	top_can	44.72
can_1	64.95	can_1	48.68	can_1	67.22
can_2	66.44	can_2	41.35	collar	7.71
bottom_can	24.40	can_3	64.54	can_2	47.30
		can_4	60.22	bottom_can	21.03
		bottom_can	51.07		
Total	203.22	Total	317.77	Total	187.98

As anticipated, a significant result and conclusion are drawn from these results, especially when one evaluates the results in Table 13. The resulting thicknesses for most of the cans in Design 2 are not feasible due to manufacturing constraints. For this reason, Design 2 is ruled out at this stage of the study, and its ULS and FLS results are omitted in the next pages but may be found in the Appendix B.

4.6.2. Maximum deflection and TPE

According to Equation 24 and Equation 31, the maximum deflection ω_{max} and the TPE depend on the cross-section considered. Due to the fact that the cross-section properties are variable (inertia and areas) an approximation is done using the geometrical mean value from these properties taken at the junctions. Table 16 displays the results for Design 1 and Design 3. These values play an important role in the comparison between the continuum solution and the numerical approximation that will be presented in the next section.

Table 16: Analytical results of the TPE absolute value and maximum lateral deflection.

	Design 1	Design 3	Unit
TPE	3.61×10^5	3.96×10^5	J
Maximum deflection (ω_{max})	8.23	9.03	mm

4.6.3. ULS results

Given the final thickness adopted for the components of each design, Table 17 to Table 18 show the global stresses at the junctions obtained according to the procedure described in subsection 4.2. The bending moment M_x produces normal stresses of tension and compression on the cross-section, which means negative and positive values of σ_{z_M} . However, as the normal force F_z generates compression (Table 9), the compressive action of M_x is more critical and it is the one displayed in the following tables.

Table 17: Stresses result at the junctions of Design 1, in MPa.

Design 1			
	Junction 1	Junction 2	Junction 3
σ_{z_M}	-111.26	-118.61	-108.17
σ_{z_N}	-7.09	-8.39	-8.47
Normal stress (σ_z)	-118.35	-126.99	-116.64
τ_{yz_T}	3.89	4.05	3.60
Shear stress (τ_{yz})	3.89	4.05	3.60
Von Mises stress	118.54	127.19	116.81

Table 18: Stresses result at the junctions of Design 3, in MPa.

Design 3				
	Junction 1	Junction 2	Junction 3	Junction 4
σ_{z_M}	-117.91	-128.51	-126.19	-125.66
σ_{z_N}	-7.51	-9.06	-9.19	-9.80
Normal stress (σ_z)	-125.42	-137.57	-135.37	-135.46
τ_{yz_T}	4.12	4.38	4.29	4.18
Shear stress (τ_{yz})	4.12	4.38	4.29	4.18
Von Mises stress	125.62	137.78	135.58	135.65

As explained in subsection 4.2 and shown in Figure 23 the most critical region in the geometry is the one aligned with the negative y-axis and zero x-axis. This region does not suffer from the shear stress due to the lateral force F_y . Instead, that is the region where the maximum normal stress from the bending moment sums up to the normal stress from the normal force. In addition, these results quantitatively demonstrate the way how the stresses distribute along the junctions. In terms of global stresses, Junction 2 is the most critical one in Design 1. Furthermore, in the case of Design 3, Junction 2 is the most critical one, although the stress values in Junction 3 and Junction 4 are close to it. On top of that, Table 17 and Table 18 also show how dominant the normal stresses are, especially due to the large value that the M_x assumes when compared with the other loads, as shown in Table 9.

Following, the main ULS results according to the procedure shown in subsection 4.4 are presented. Table 19 and Table 20 show the results of Design 1, and Table 21 and Table 22 show the results of Design 3. In these tables, the design axial compression (force) includes not only the natural boundary condition but also the self-weight of the cans above the considered junction. Moreover, the thickness t_p refers to the smaller reduced thickness at the junction, namely the smaller nominal thickness between the two cans reduced by the corrosion allowance.

Table 19: Main ULS results from the tubular junction of Design 1.

Junction 2				
Parameter	can_1	can_2	Unit	
Outer diameter	8.15		mm	
Thickness (t_p)	99	79	mm	
Axial compression resistance ($N_{c,Rd}$)	7.71×10^5	6.17×10^5	kN	
Design axial compression (F_z)	0.17×10^5		kN	
Von Mises stress ($\sigma_{j,Sd}$)	127.19		MPa	
Design shell buckling strength ($f_{k,sd}$)	299.53	294.04	MPa	
Bending moment resistance (M_{Rd})	1.65×10^6	1.28×10^6	kNm	
Design bending moment (M_x)	0.49×10^6		kNm	
Shear force resistance (V_{Rd})	2.23×10^5	1.78×10^5	kN	
Design shear force (F_x)	0.03×10^5		kN	
Torsional moment resistance ($M_{T,Rd}$)	1.77×10^6	1.42×10^6	kNm	
Design torsional moment (M_z)	0.03×10^6		kNm	

From the results in Table 19, one may notice how close the design loads are to the limit of each can (resistance). The axial load represents less than 3% of the axial compression resistance. The Von Mises stress is around 44% of the shell buckling strength. The applied bending moment represents 30% of the bending moment resistance. The same type of analysis may be done from results in Table 20, where the axial stress in the conical region reaches around 34% of the local buckling strength for the elements in Junction 1, for instance.

Table 20: Main ULS results from the conical junctions of Design 1.

Parameter	Junction 1		Junction 3		Unit
	top_can	can_1	can_2	bottom_can	
Outer diameter	7.5		8.9		mm
Thickness (t_p)	99	99	79	74	mm
Slope (α)	5.65		5.65		°
Design axial force (F_z)	1.69×10^4		1.81×10^4		kN
Design bending moment (M_x)	4.83×10^5		5.07×10^5		kNm
Equivalent design axial stress ($\sigma_{eq,Sd}$)	121.39		114.01		MPa
Design hoop stress ($\sigma_{hc,Sd}$)	-45.87		-56.98		MPa
Local buckling strength (f_{clc})	350.78	350.78	340.59	338.48	MPa
Characteristic axial local compressive strength (f_{cl})	354.42	354.01	353.64	354.80	MPa
Characteristic hoop buckling strength (f_h)	355	355	355	355	MPa
Total design stress ($\sigma_{tot,Sd}$)	-204.84	34.90	18.19	-225.89	MPa

In the case of Design 3, as one notices in Table 21 the Von Mises stress is around 47% of the shell buckling strength of can_2 in Junction 3, the design bending moment reaches around 43% of the bending moment resistance in the same component and, according to

Table 22, the axial stress in the conical region is around 38% of the local buckling strength. The exact percentages will depend on the component and the junction one is looking at.

Table 21: Main ULS results from the tubular junction of Design 3.

Parameter	Junction 2		Junction 3		Unit
	can_1	connection	connection	can_2	
Outer diameter		8.13		8.38	mm
Thickness (t_p)	93	73	73	70	mm
Axial compression resistance ($N_{c,Rd}$)	7.24×10^5	5.69×10^5	5.87×10^5	5.63×10^5	kN
Design axial compression (F_z)		0.17×10^5		0.18×10^5	kN
Von Mises stress ($\sigma_{j,Sd}$)		137.78		135.58	MPa
Design shell buckling strength (f_{ksd})	296.92	307.53	307.52	285.92	MPa
Bending moment resistance (M_{Rd})	1.53×10^6	1.16×10^6	1.23×10^6	1.17×10^6	kNm
Design bending moment (M_x)		0.49×10^6		0.50×10^6	kNm
Shear force resistance (V_{Rd})	2.09×10^5	1.64×10^5	1.69×10^5	1.62×10^5	kN
Design shear force (F_x)		0.03×10^5		0.03×10^5	kN
Torsional moment resistance ($M_{T,Rd}$)	1.66×10^6	1.31×10^6	1.39×10^6	1.34×10^6	kNm
Design torsional moment (M_z)		0.03×10^6		0.03×10^6	kNm

Table 22: Main ULS results from the conical junctions of Design 3.

Parameter	Junction 1		Junction 4		Unit	
	top_can	can_1	can_2	bottom_can		
Outer diameter		7.5		8.9	mm	
Thickness (t_p)	93	93	70	63	mm	
Slope (α)		5.00		5.00	°	
Design axial force (F_z)		1.68×10^4		1.80×10^4	kN	
Design bending moment (M_x)		4.83×10^5		5.07×10^5	kNm	
Equivalent design axial stress ($\sigma_{eq,Sd}$)		128.90		128.27	MPa	
Design hoop stress ($\sigma_{hc,Sd}$)		-44.38		-63.47	MPa	
Local buckling strength (f_{clc})	349.46	349.46	336.62	332.71	MPa	
Characteristic axial local compressive strength (f_{cl})	354.39	353.73	354.07	354.77	MPa	
Characteristic hoop buckling strength (f_h)	355	355	355	355	MPa	
Total design stress ($\sigma_{tot,Sd}$)		-209.11	45.20	28.71	-258.43	MPa

4.6.4. FLS results

The main results from the FLS assessment are found below. For the calculation of the SCF at the tubular connections, it is assumed that there is no S-N curve misalignment δ_0 and that the maximum misalignment δ_m is 3 mm. Table 23 and Table 24 show the SCF of each design.

These results refer to the maximum SCF at the outer diameter. SCF values for the inner diameter may be found in Appendix B. As the data shows, some of the components have 2 different SCFs as they are welded to other components at their top and at their bottom. In that sense, the greater SCF per component is taken for the hot spot stress

range calculation as it will be more critical for the design. The *Type* parameter in the tables below refers to the type of connection between cans. When there is a change in slope between consecutive cans, one has a conical junction type. If both cans have the same slope, then one has a tubular junction type.

Table 23: Stress concentration factors for Design 1 components and junctions.

Junction	Type	Component	SCF
Junction1	conical	top_can	1.72
		can_1	1.72
Junction2	tubular	can_1	1.31
		can_2	1.44
Junction3	conical	can_2	1.91
		bottom_can	1.81

Table 24: Stress concentration factors for Design 3 components and junctions.

Junction	Type	Component	SCF
Junction1	conical	top_can	1.66
		can_1	1.66
Junction2	tubular	can_1	1.33
		collar	1.47
Junction3	tubular	collar	1.16
		can_2	1.11
Junction 4	conical	can_2	1.78
		bottom_can	1.88

In order to check all relevant criteria and to get the fatigue life, the nominal stress range is calculated using the DEL in Table 10 and following the same procedure as explained in subsection 4.2. Considering the number of stress cycles n equal to 10^7 and using the S-N curve data in Appendix B, the results in Table 25 and Table 26 are found. On top of that, as mentioned in subsection 4.5, a design fatigue factor (DFF) equal to 3 is assumed, considering the structure in the upper splash zone.

Similarly to the SCF calculation, a single component presents two different values of fatigue life, one per junction. The values in Table 25 and Table 26 feature only the minimum fatigue life per component. Other results are found in Appendix B.

Table 25: Main fatigue life results of Design 1.

Parameter	top_can	can_1	can_2	bottom_can	Unit
Nominal stress range ($\sigma_{nominal}$)	18.26	18.26	19.71	18.22	MPa
Hot spot stress range ($\sigma_{hotspot}$)	31.38	31.38	32.83	32.93	MPa
Cycles to failure (N)	3.11×10^7	3.11×10^7	3.25×10^7	3.46×10^7	cycles
Cumulative damage (D)	0.32	0.32	0.31	0.29	-
Calculated fatigue life (L_c)	98	98	102	109	Years

Table 26: Main fatigue life results of Design 3.

Parameter	top_can	can_1	connection	can_2	bottom_can	Unit
Nominal stress range ($\sigma_{nominal}$)	19.35	19.35	20.03	16.84	18.57	MPa
Hot spot stress range ($\sigma_{hotspot}$)	32.03	32.03	29.55	29.00	34.97	MPa
Cycles to failure (N)	3.02×10^7	3.02×10^7	6.05×10^7	6.99×10^7	3.11×10^7	cycles
Cumulative damage (D)	0.33	0.33	0.17	0.14	0.32	-
Calculated fatigue life (L_c)	95	95	191	220	98	Years

Due to the fine-tuning process used to obtain the cans' thicknesses, the calculated fatigue life of all components is similar, as well as the cumulative damage. That is due to the fact that, for all components, the criteria applied is the same, as stated in Equation 85.

4.6.5. Slope and thickness sensitivity analysis

As previously explained, the slope angle α has an important influence on ULS results by means of the stresses generated at the conical regions. Furthermore, Equation 80 and Equation 81 also show the link between the slope and the SCF in conical junctions. In that sense, two more detailed studies are performed to illustrate this influence and to verify how this affects the fatigue life.

In order to proceed with it, one needs to relax one of the constraints established initially in Table 2 as it is not possible to study variable slope angles in an isolated way without changing other aspects of the design. Any isolated change in the slope would stretch or squeeze the structure modifying the interface level. Any change in the interface level would result in distinct DELs. Thus, the slope is altered solely over the diameter adjustment, and, hence, the loads in Table 10 are still valid. Equation 87 shows how these parameters are related.

$$\alpha = \arctan\left(\frac{D_{bottom} - D_{top}}{2h_{can}}\right) \quad (87)$$

Where D_{bottom} is the bottom diameter of the truncated conical can, D_{top} is the top diameter, and h_{can} is the height. The studies are performed only for Design 1. The first one deals with the two intermediate cans (can_1 and can_2) and it is presented in Figure 29. The slope variation is done by changing the top diameter of can_1 and the

bottom diameter of can_2 in such a way that both have the same slope. On top of that, the SCFs values assessed refer to the value generated in the conical junctions that these components are part of (junction1 for can_1 and junction3 for can_2).

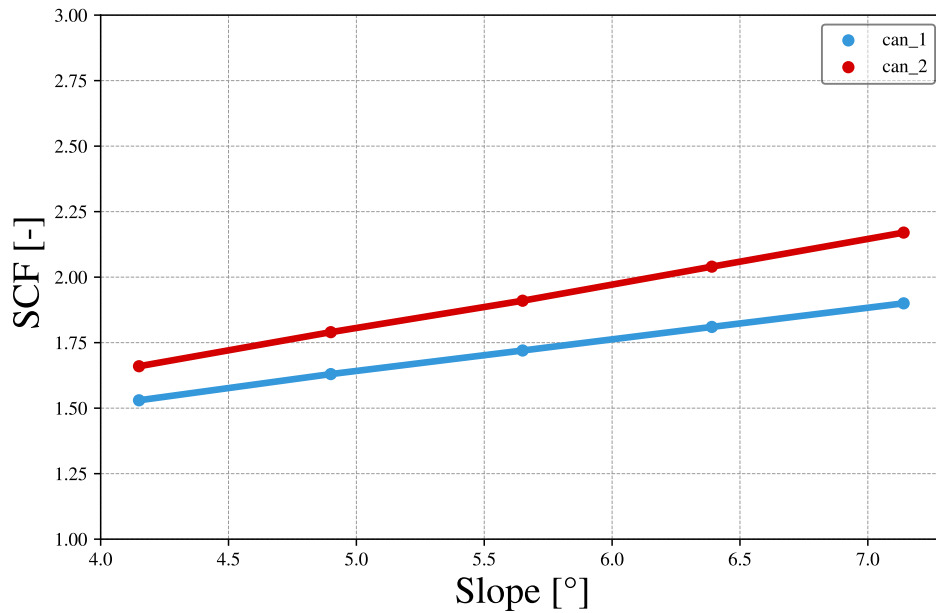


Figure 29: Variation of the maximum stress concentration factor at each component as a function of the cone slope. Components of Design 1.

It is important to point out that the SCF of the cans depends not only on their own dimensions but also on the dimensions of the other cans that are attached to them. Moreover, in this first study, the thicknesses are kept as in the final thickness in Table 12. Finally, the slope range displayed in the plots is a result of a fluctuation of diameters from 7.67 m to 7.33 m at can_1 and from 8.7 m to 9.1 m at can_2.

In Figure 29 one may notice that, for the same slope, can_1 has a smaller SCF because it also has a smaller thickness (see Equation 80 and Equation 81). Not only that, but the diameter also affects the SCF value. In that sense, one possible way to compensate for the quick decay in fatigue life, in case a large slope is used, is to increase the thickness of the can.

Finally, Figure 30 illustrates the same sensitivity study, but in terms of the fatigue life variation. This graph points out that can_1's rate of fatigue life decline is greater than that of can_2. In that sense, for slopes greater than 5.5° , even though the SCF is greater in can_2, the fatigue life of can_1 is smaller due to the fact that can_2 is thicker than can_1. Moreover, it is interesting to highlight that a slight change in the hot spot stress or the SCF has a massive impact on fatigue life because, as shown in Equation 82 and Equation 86, a greater stress range decreases the fatigue life and may even change the Wöhler coefficient m (from 5 to 3) and the region to be considered in the S-N curve.

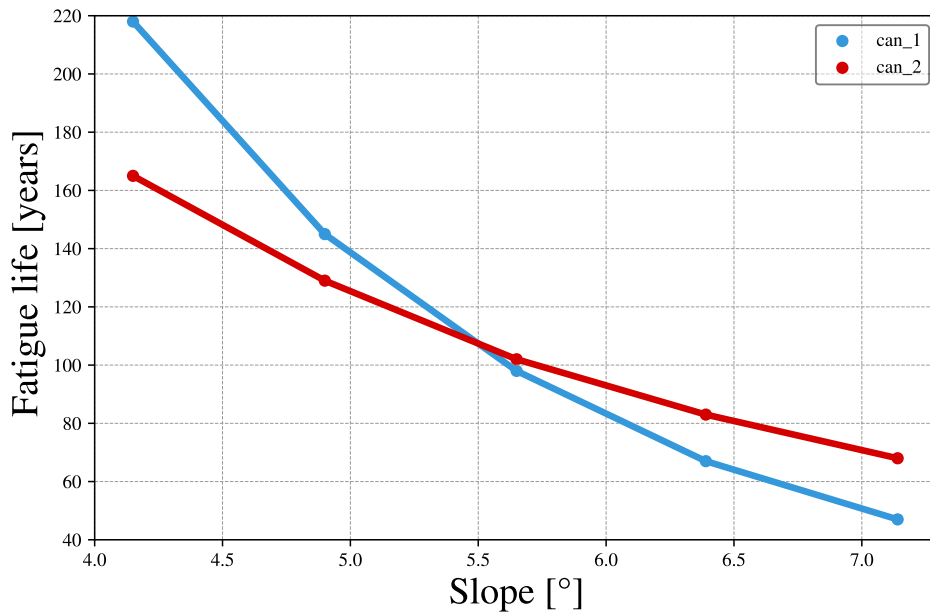


Figure 30: Variation of the calculated fatigue life, in years, of each component as a function of the cone slope. Components of Design 1.

A second study is performed, as shown in Figure 31. This time, one focuses only on can_1 of Design 1 and promotes a variation in its thickness in order to understand how the SCF and the fatigue life change.

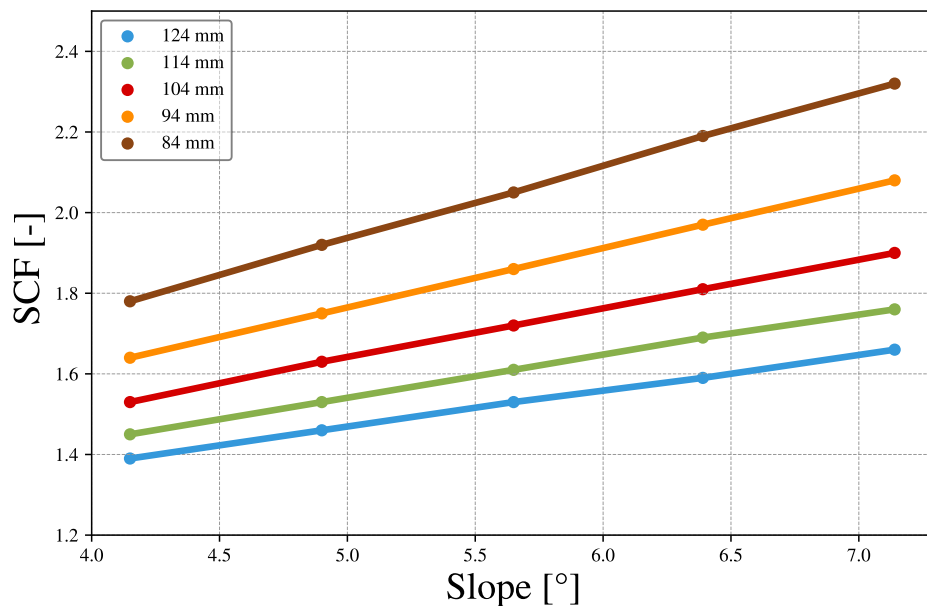


Figure 31: Variation of the maximum stress concentration factor in can_1 of Design 1 for different thicknesses.

All the other dimensions and thicknesses are kept as in Table 3 and Table 12. Further-

more, the results presented refer to the conical junction that this can is part of (junction1). Figure 31 shows that the SCF grows at a similar rate for all the different thicknesses. This is a direct result of the Equation 81. Moreover, as expected, the thinner the can, the greater the SCF. Figure 32, on the other hand, illustrates the decay in fatigue life over the slope increase. However, it also indicates that the decay rate is greater for thicker cans.

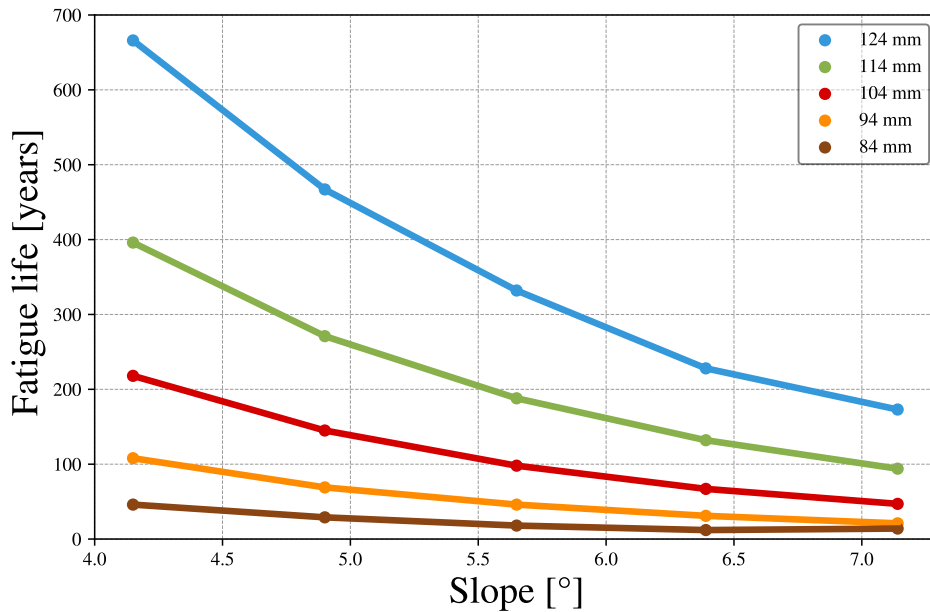


Figure 32: Variation of the calculated fatigue life in can_1 for different thicknesses.

Using the plot in Figure 32 it is possible to estimate the minimum thickness that can_1 needs to have. Combining the expressions from Equation 83 to Equation 86 for the case of this project where $\eta = 0.3$ and $L_t = 31.5$ years, L_c has to be at least 94.5 years. Restraining the slope angle to 5° , Figure 32 shows that the can needs to have between 94 mm and 104 mm. A slope smaller than 4.5° , for instance, could allow for a can with 94 mm of thickness.

Finally, in Figure 32 the effect that a stress increment has on the fatigue life is even more evident. By reducing the thickness for the same can, the SCF and stress range increase and this produces a large decay in the fatigue life.

5. NUMERICAL INVESTIGATION

5.1. Applicable codes and standards

The numerical approach based on the finite element method (FEM) is implemented with the purpose of verifying the analytical results found. More specifically the maximum displacement and stress distribution. This finite element analysis (FEA) is carried out by means of the computational software *Siemens NX, 1859 version* and the specific solver *Simcenter SAMSEF 18.2* used with an academic institutional license. The machine used for the simulations is an Intel(R) Core(TM) i5-8265U CPU @ 1.60GHz with 8040 MB of physical RAM. The software is used not only to run the simulations but also to build the model, pre-processing and post-processing the results. The main results are here documented by plots.

It is important to highlight that a FEA produces an approximate solution. The structure is decomposed into elements interconnected by a discrete number of nodal points. The method consists of finding the displacement anywhere inside the elements from an interpolation of these nodal points' displacement. In addition, one assumes displacement modes on every element such that a continuity (in displacement) between adjacent elements is respected.

The DNV-ST-0126 [19] presents some general guidelines for the FEM analysis and the DNV-RP-C203 [8] is used in the context of assessment at stress concentration regions. Moreover, common good practices in modelling, geometry preparation, and meshing are implemented in order to obtain results as close as possible to the analytical solutions.

As stated in section 4, the results from the ULS and FLS studies follow the decision of disregarding Design 2 as a feasible one. For this reason, this design is not an object of the FEA investigation. Finally, further FEA plots are found in Appendix C.

5.2. Geometry

The TPs are modelled as single mid surfaces using the dimensions given in subsection 3.1 (Design 1) and subsection 3.3 (Design 3). Initially, a sketch is created in the xz-plane (blue line in Figure 33), and then, it is revolved around the z-axis. After that, edges are generated in order to mark and divide the faces that will be the different cans along the longitudinal direction z. Therefore, each can correspond to a face on the surface. This allows to assign a different mesh thickness for each face. However, this also requires special attention for the mesh continuity between the faces of the surface. On top of that, for Design 3, for instance, the fillets in the edges of the collar are removed so that the mesh generation becomes easier. In the end, a part file (*.prt*) is generated.

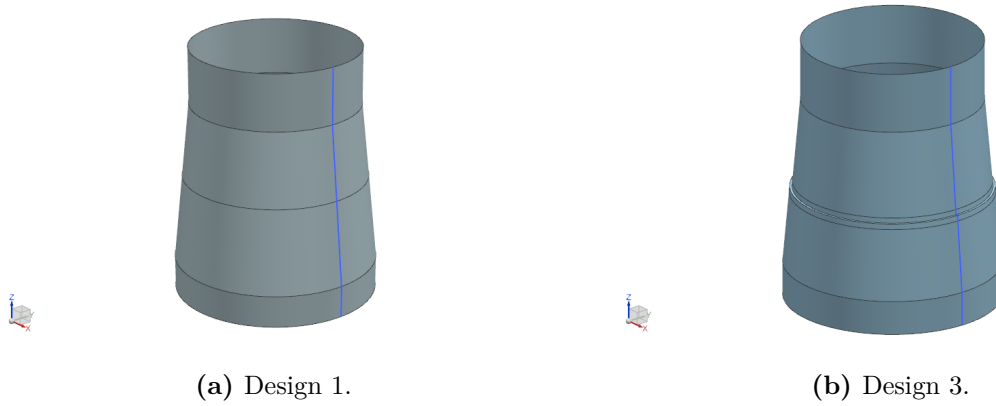


Figure 33: Surface geometries in NX interface.

5.3. Physical formulation and hypothesis

Following this, the proper hypothesis and boundary conditions are established to reflect the physical reality. Firstly, one assumes a linear static simulation. This also brings along the hypothesis of small deflections, inter-element continuity, and, therefore, a perfect bonded connection between the cans. For this reason, although each can is a separate instance, they share their topology, especially in terms of continuity of displacement. This is achieved through the sketching procedure described previously. Furthermore, welding effects such as initial imperfections and residual stresses in the junctions are not detailed modelled or considered in the simulations. Important to highlight that, although the geometry is clearly symmetric, the loads are not. The coupling of the applied moments and loads does not allow a suitable 2D model that can account for all the effects they produce.

In general, this type of FEA tries to solve Equation 88, a linear equation.

$$Kq = g \quad (88)$$

Where, K is the stiffness matrix, q is a vector with the generalized displacements (degrees of freedom) and g is a vector with natural boundary conditions as concentrated loads (at nodes) [26]. In addition, one essential boundary condition is defined which is the fixing end according to Figure 15. By imposing this boundary condition, the six degrees of freedom of the cylindrical face are restrained and all the rigid body modes are suppressed.

The natural set of boundary conditions consists of the extreme loads in Table 9. Due to limitations imposed by the way the software interprets the load application, the forces and moments are applied in a node created at the centre of the TP's top, at 11 m. Subsequently, this node is bonded to the nodes of the interface by means of rigid links (*RigidLinks[RBE]*). Figure 34 shows the complete setup of boundary conditions in Design 1 geometry. The same setup is applied to Design 3.

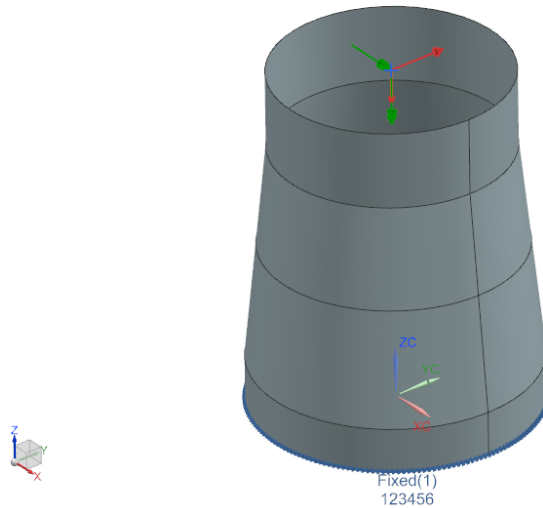


Figure 34: Boundary conditions imposed in *NX*. At the top, a blue point marks the location of the node where the forces and moments are applied. In red F_y and F_z , and in green M_x and M_z . At the bottom, in blue, is the fixed constraint and the indication of the restrained degrees of freedom.

5.4. Mesh study

The spatial discretization of the structure is a critical part of the FEA. Results and their reliability depend upon, among other factors, the appropriate mesh. This includes not only the element size but also its type, order, shape, and spacial fitting in the sense of approximating the structure's area. The mesh study is firstly interested in obtaining the more adequate element type and then, with it, a convergence study is performed. This whole study is done with Design 1, thereafter with the same element type the convergence is performed for the structure of Design 3.

According to the literature, there are notable distinctions in the performance of triangular and quadrilateral finite elements [26]. Triangular elements are not particularly effective in handling bending problems and are therefore suggested only for regions with minimal stress variations or when the geometry of a quadrilateral element is unsuitable. However, the geometry of the proposed TPs proved to be better and more easily filled with triangular elements. Moreover, as mentioned in section 4, the structure behaves as a shell based on its yielding strength and the characteristic elastic local buckling strength. Additionally, quadratic (second-order) interpolation elements demonstrate an improved capacity to represent the circular shape of the structure and more accurate results with fewer elements [29]. Thus, the *Heterosis Shell - T155*, a shell element, is used and a *.fem* file is generated in *NX*. This file contains the mesh data such as nodes, elements, physical properties, and material properties.

This element type is defined by six nodes. Three corner nodes and three mid-side nodes with six degrees of freedom each (three rotations and three translations). Furthermore, it

uses the 3-midpoint rule to assign three Gauss (integration) points [30], as illustrated in Figure 35.

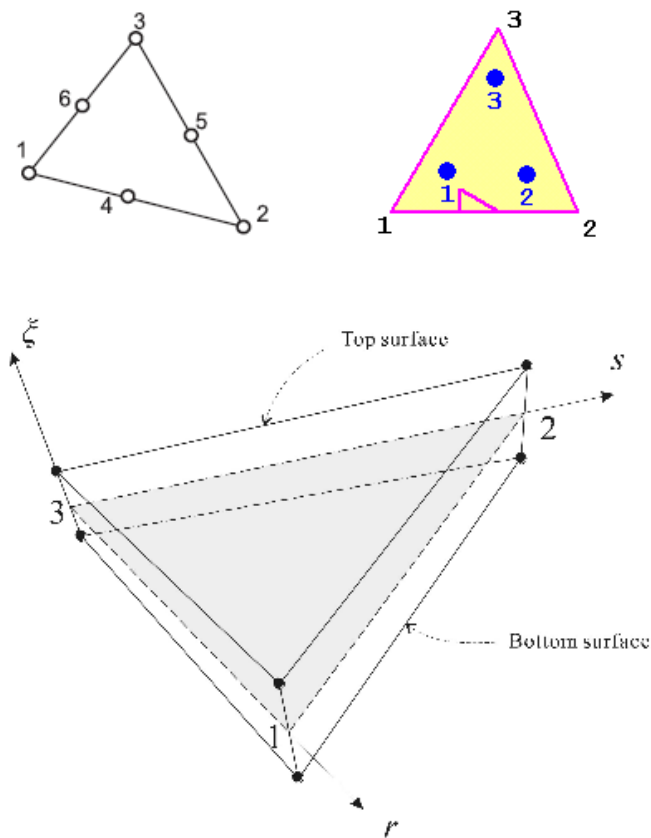


Figure 35: 6 nodes shell element, its integration points, and a representation of the surfaces that are created once a thickness is assigned to it [30].

Following this, an efficient mesh has to be determined. In that sense a mapped mesh is defined with the 6-node shell element type and an energy approach is used to verify the global convergence of the mesh. The principle of minimum TPE states that the value of the TPE is stationary when the structure is in static stable equilibrium. Moreover, using an FE approximation, this principle means that it is expected that the absolute value of the TPE from the FEA will converge to the exact one (from an analytical solution) when the number of degrees of freedom increases (mesh refinement).

Therefore, starting from a coarse mesh of 500 mm element size, the model is refined gradually up to 100 mm of element size. In addition, some mesh parameters and simulation results are taken, as shown in Table 27 for Design 1 and Table 28 for Design 3. In these tables, the maximum Von Mises stress is the element average.

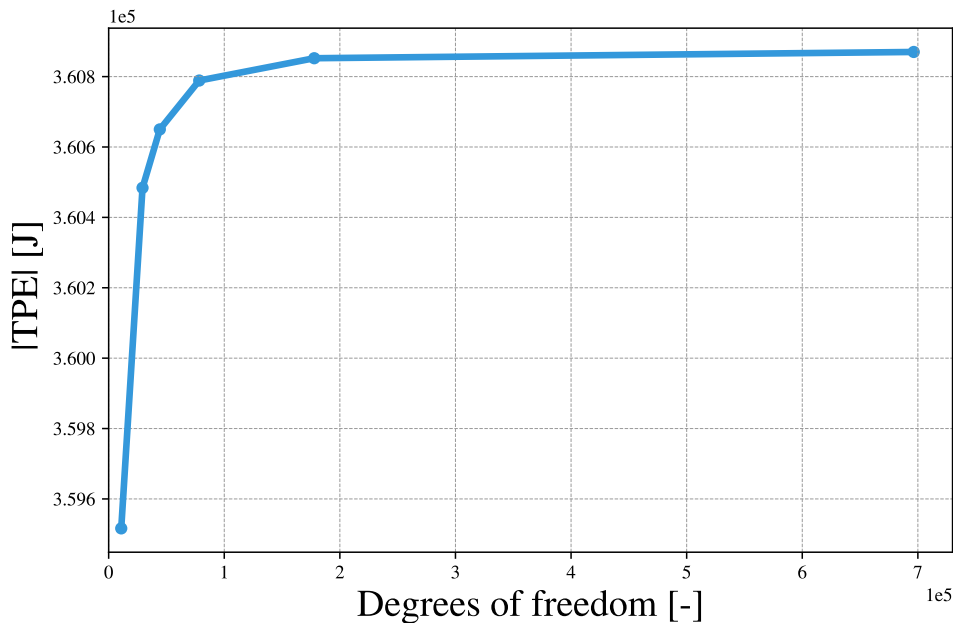
Table 27: Refinement study for Design 1.

Design 1						
Mesh size [mm]	Number of DOF	Potential energy [J]	TPE error [%]	Maximum displacement [mm]	Maximum Von Mises Stress [MPa]	Running time (seconds)
800	10878	3.60×10^5	-	7.93	119.71	2.2
500	29292	3.60×10^5	0.27	7.96	124.12	3.8
400	44256	3.61×10^5	0.05	7.96	125.87	4.3
300	78348	3.61×10^5	0.04	7.97	126.86	9.1
200	177834	3.61×10^5	0.02	7.97	127.77	44.8
100	696420	3.61×10^5	0.00	7.97	128.47	578.3

Table 28: Refinement study for Design 3.

Design 3						
Mesh size [mm]	Number of DOF	Potential energy [J]	TPE error [%]	Maximum displacement [mm]	Maximum Von Mises Stress [MPa]	Running time (seconds)
800	12708	3.93×10^5	-	10.53	156.27	1.5
500	28530	3.95×10^5	0.52	10.59	163.10	2.9
400	44688	3.96×10^5	0.18	10.61	165.54	4.8
300	74664	3.96×10^5	0.08	10.62	166.47	7.9
200	165114	3.96×10^5	0.05	10.63	167.46	24.9
100	645240	3.96×10^5	0.02	10.63	167.87	536.3

From these results, it is possible to notice the rapid increase in the computational time as the mesh is refined. In that sense, meshes with smaller elements become time costly. Furthermore, one may plot the evolution of the absolute value of TPE as a function of the degrees of freedom, as Figure 36 and Figure 37 show.

**Figure 36:** Global convergence of Design 1. From the analytical solution the absolute value of TPE is 3.61×10^5 J.

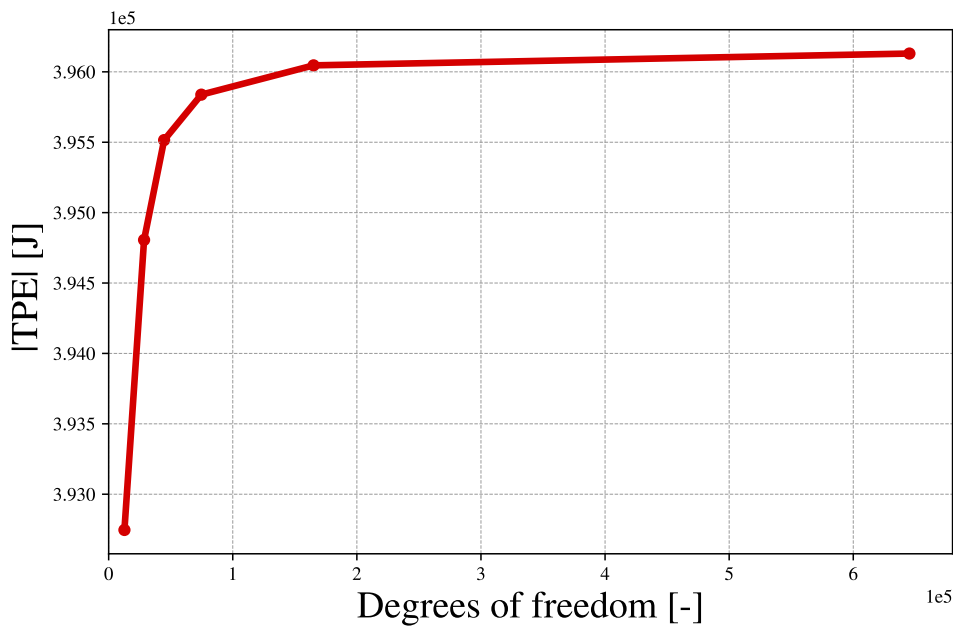


Figure 37: Global convergence of Design 3. From the analytical solution the absolute value of TPE is 3.96×10^5 J.

Based on the convergence of the mesh, the 100 mm element size is considered reliable to achieve a good accuracy of results of the simulation. Moreover one can compare the numerical solution of TPE from the finer mesh with those obtained in the analytical calculation (Table 16). As expected, the convergence of TPE from the approximation method (FEA) is a monotonic convergence that increases towards a maximum value established by the continuum solution. Further, in section 6 similarities between analytical and numerical stress results are shown, especially for points in the middle of the cans.

The next step consists on evaluate the quality of the finer and definitive mesh. Two mesh metrics are used to measure the uniformity and distortion of elements. The aspect ratio is a quantitative measure of the ratio between the side lengths of the element, as shown in Figure 38.

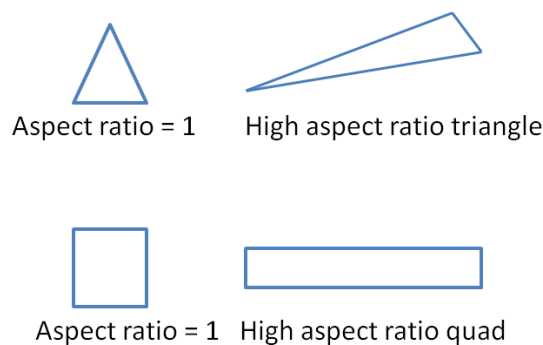


Figure 38: The closer the aspect ratio is from 1 the better quality of the element [31].

According to DNV-ST-0126 [19], the aspect ratio should ideally be equal to 1, but values of up to 3 to 5 do usually not influence the results and are thus acceptable. The second metric is the warping factor. This parameter measures the non-flatness or twist of the elements, as shown in Figure 39. According to DNV-ST-0126 [19], even a slight warping of the elements may influence the results significantly. Therefore, using the *Element Quality Check* tool in *NX*, these two specific checks are implemented. For aspect ratio, a warning limit of 3 and an error limit of 5 are set. Whereas for the warping factor, a warning limit of 0.01 and an error limit of 0.05 are set.

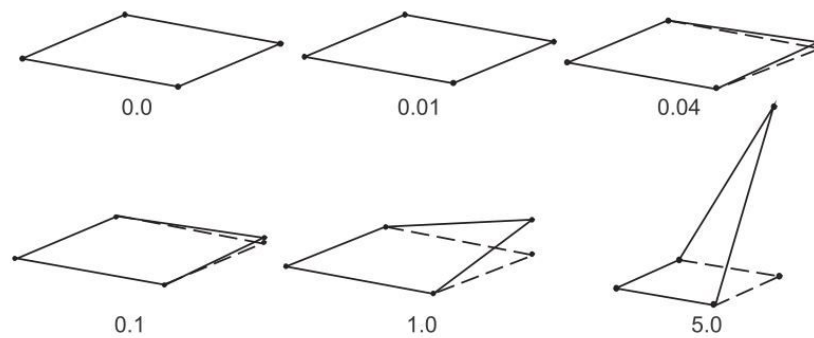
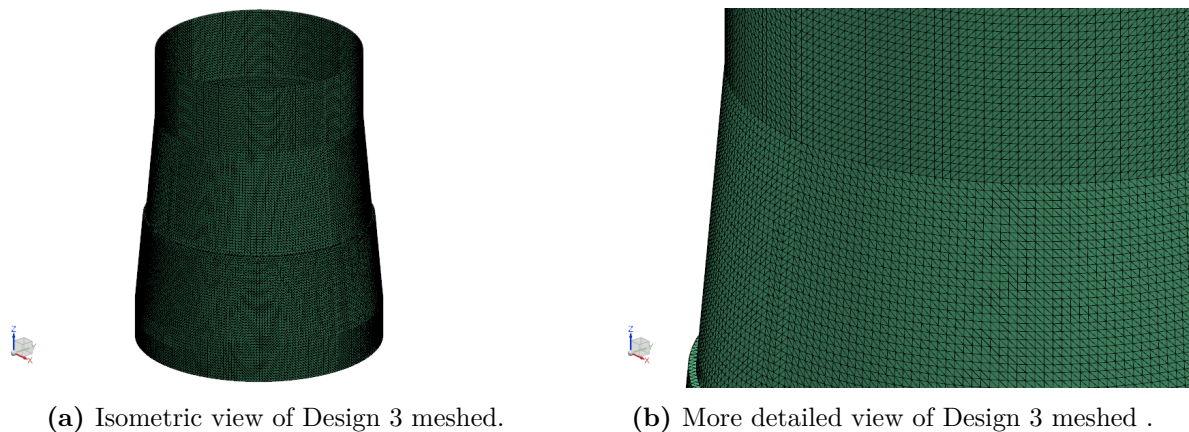


Figure 39: Warping factor metric. The higher the value, the higher the element distortion which results in poor approximations [31].

In the end, none of the two proposed designs presented any error or even warning. For Design 1, the worst aspect ratio value is 2.42 and for Design 3 it is 1.82. These results may be found in Appendix C.

The mesh suitability is also checked in terms of geometry approximation, as shown in Table 29. The comparison between the desired surface area with those obtained with the finer mesh, for both designs, demonstrates a quite accurate geometry approximation. Therefore, both fine meshes present excellent quality. Figure 40 illustrates the definitive mesh of Design 3.



(a) Isometric view of Design 3 meshed.

(b) More detailed view of Design 3 meshed .

Figure 40: Finer mesh of 100 mm at Design 3 geometry.

Table 29: Geometry approximation results for the finer mesh.

	Design 1	Design 3	Unit
Real surface area	278.7269564	279.8541266	m ²
FE approximation surface area	278.7552392	279.9037390	m ²
Error	-0.010	-0.018	%

5.5. Displacement and Von Mises stresses

The global converged mesh is used to assess the main results on stresses and displacement. The *.fem* file is imported to a *.sim* file where all the boundary conditions are defined, the simulation is launched and the solutions are stored.

It is important to mention that the approximate solution of a FEA provides a strong knowledge of the displacement field, as it is the solution of Equation 88. Nonetheless, the stresses are discontinuous throughout element boundaries and some strategies may be implemented to obtain a meaningful and reliable result. One of them is to display the weighted average of the stress field over the element. By doing that, large inter-element jumps may emerge. One way to eliminate these jumps is to convert the stress field into a continuous one by getting the nodal averaging and interpolating it by means of the shape functions.

In this project, the first approach is used to represent the stress results because it represents more accurately the results, despite the fact that it is not the most appealing visually. Moreover, in order to reduce the stress jumps one relies on the finer mesh so that a smoother transition between elemental stress values may be found. Figure 41 and Figure 42 display the displacement results for Design 1 and Design 3, respectively.

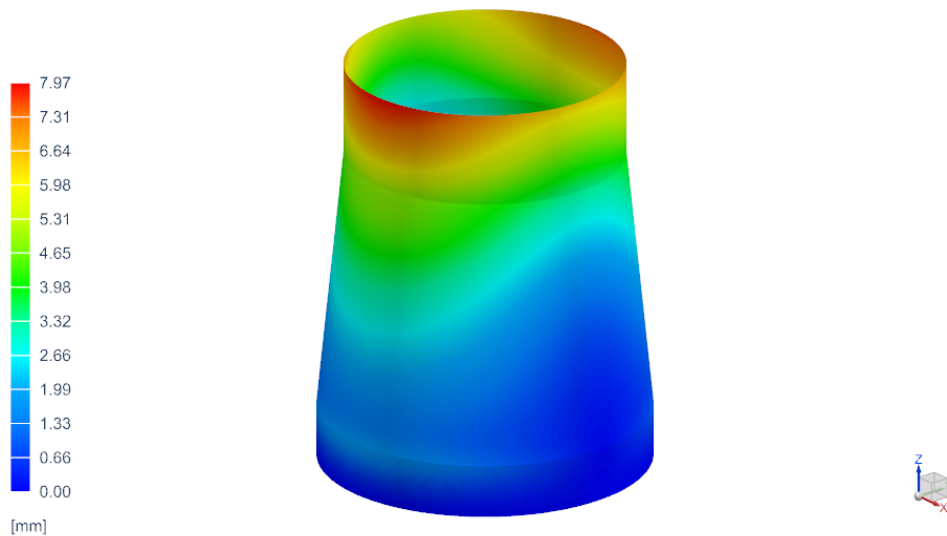


Figure 41: Displacement field | Design 1 | Maximum value: 7.97 mm .

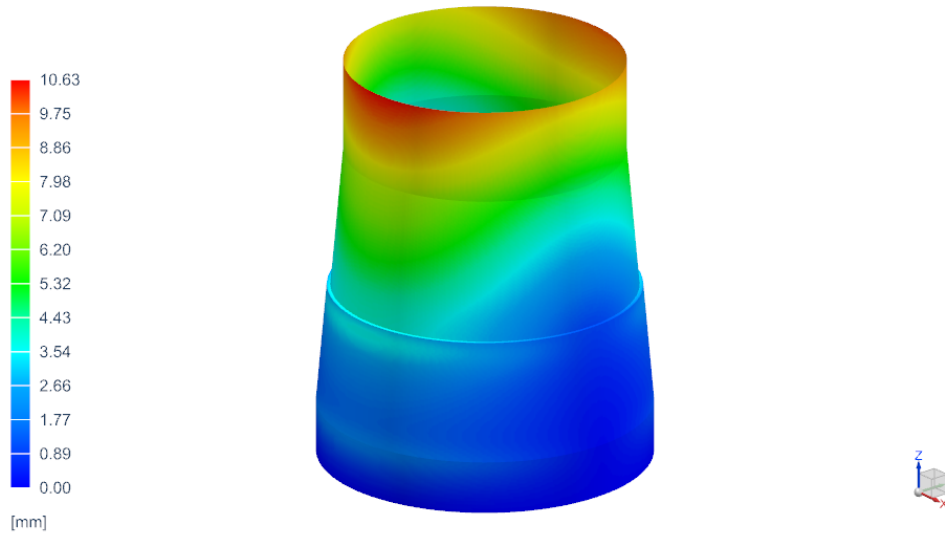


Figure 42: Displacement field | Design 3 | Maximum value: 10.63 mm .

These plots show that the TP tends to bend around the x-axis towards the negative region of the y-axis. That is a direct effect from the bending moment M_x which, as may be seen in Table 9, is relatively higher than the other loads. Moreover, this behaviour was anticipated in the analytical calculation in subsection 4.2.

Figure 43 and Figure 44 exhibit the stress distribution in the TPs. The shell stress assessed is a mean value between the top and the bottom face of the shell elements. As mentioned and predicted in section 4, there is a region of high stress in the negative y-axis and zero x-axis. In this region the compression effect of the bending moment M_x sums up with the compression from the normal force F_z .

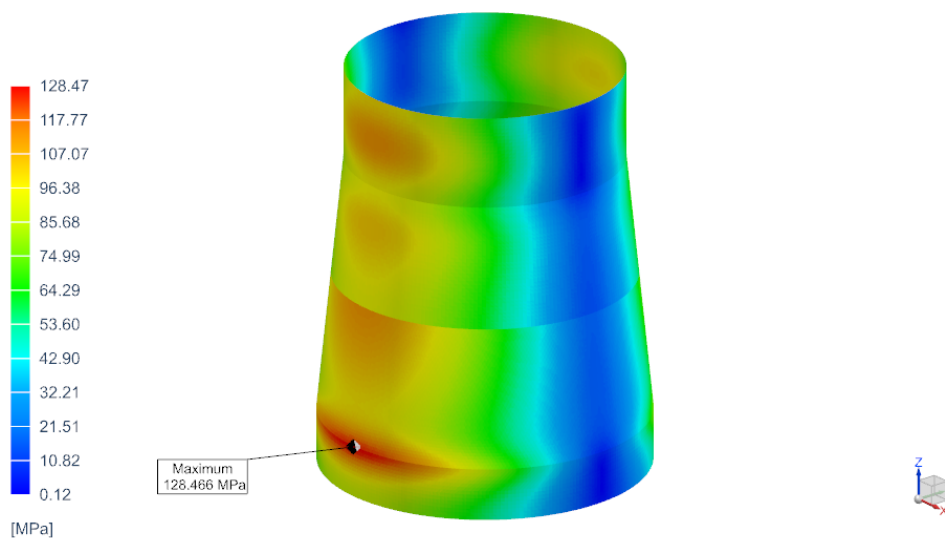


Figure 43: Von Mises Stress | Design 1 | Maximum value: 128.47 MPa .

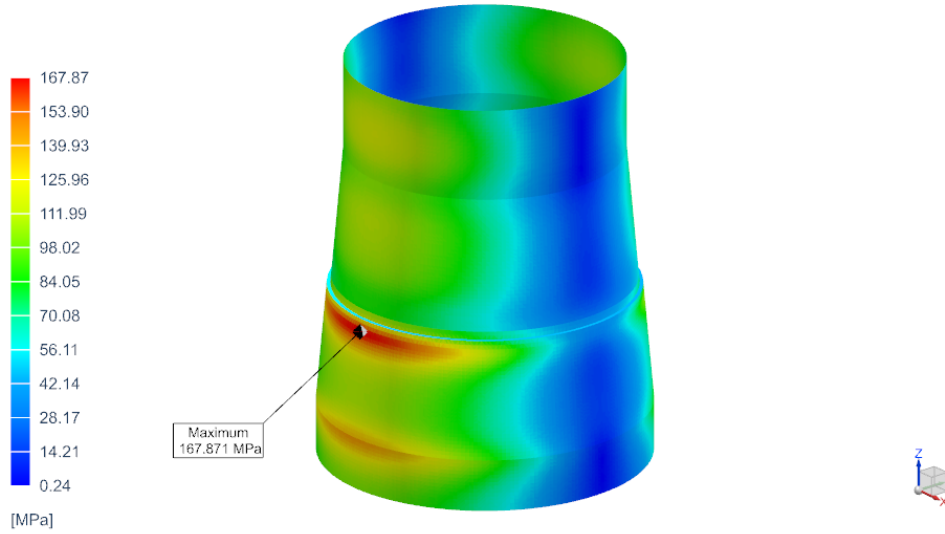


Figure 44: Von Mises Stress | Design 3 | Maximum value: 167.87 MPa .

Moreover, according to these plots, the junctions present themselves as a stress concentration area when compared to regions in the middle of the cans. In the case of Design 1, the region of Junction 3 which connects can_2 and the bottom_can is the more critical one. For Design 3, Junction 3 which connects the collar with the can_2 is the one with higher Von Mises stress.

Table 30 and Table 31 display a summary of the main results of stress distribution on different points along the longitudinal direction z , including the junctions, for Design 1 and Design 3, respectively. Elements at $x=0$ and with the greatest stress are elected to be representative of the stress at different points along z . Figure 51 and Figure 52 show the selected points position. Here, $z = 0$ is the clamped end.

Table 30: Stress distribution results from FEA for Design 1. The z -coordinate is given in metres from the top of the TP.

Design 1										
	Junction 1			Junction 2			Junction 3			
z-coordinate [m]	1	2	2.5	4	5	5.78	7	8	9.58	10
Von Mises stress [MPa]	114.90	104.35	98.57	104.94	98.37	115.48	109.76	103.07	130.71	114.22

Table 31: Stress distribution results from FEA for Design 3. The z -coordinate is given in metres from the top of the TP.

Design 3											
	Junction 1			Junction 2		Junction 3		Junction 4			
z-coordinate [m]	1	2	2.5	4	5	6.1	6.59	7.5	8.5	9.58	10
Von Mises stress [MPa]	119.30	111.64	103.65	111.12	103.32	107.53	167.87	118.92	109.61	145.56	128.69

Moreover, it is possible to verify the effect of the thickness change on the stress distribution along the profiles. Figure 45 shows how there is a break in the way the Von

Mises stress is distributed along junctions with large thickness jump. This can be seen when one goes from can_1 to can_2 in Design 1, and when one goes from can_1 to the collar in Design 3. Both transitions have a 20 mm thickness difference. On the other hand, the transition seems to be smoother in other junctions that connect cans with the same thickness or smaller thickness jump.

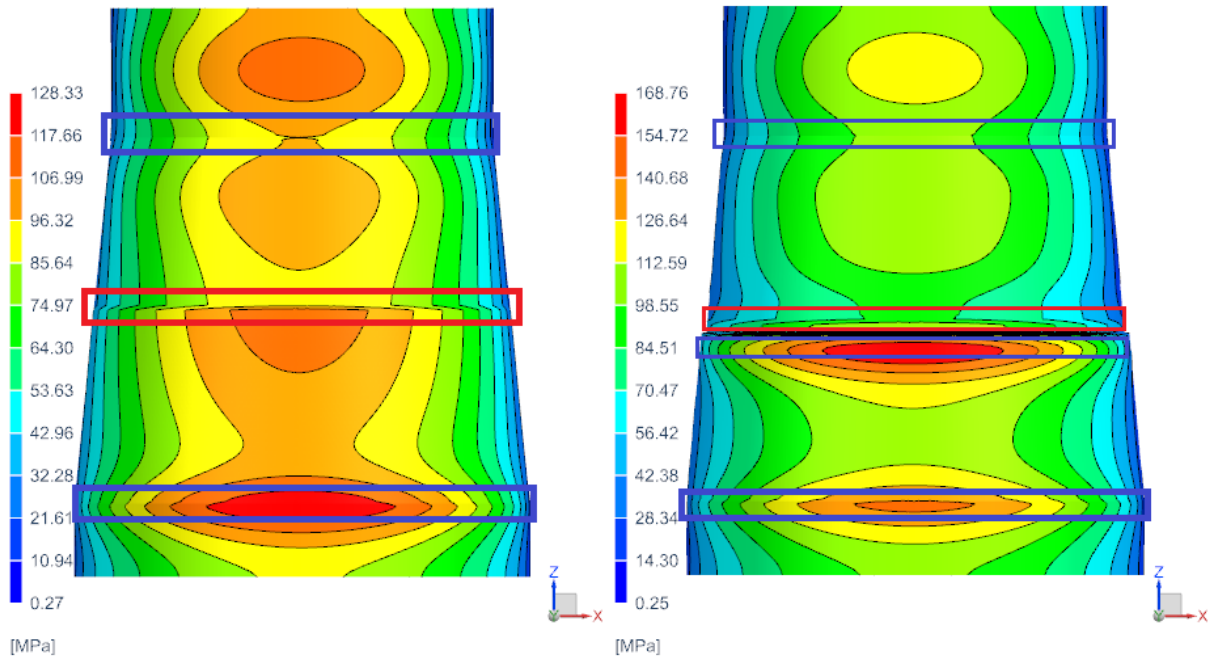


Figure 45: Von Mises stress | Front view | Stresses combined at nodes and with banded display lines | On the left is Design 1 and on the right is Design 3. Red boxes highlight junctions with a maximum thickness jump of 20 mm and in blue are the junctions between cans with the same thickness or smaller thickness jump.

However, results in Table 30 and Table 31 indicate a discrepancy when compared with the analytical results in Table 17 and Table 18. In the analytical calculation, for Design 1 the higher stress happens in Junction 2 whereas Junction 3 of the same design is the most critical one from the FEA result. Similarly, the analytical calculation points to higher stress in Junction 2 of Design 3, whereas the numerical results indicate Junction 3 as the most critical in this design. In that sense, further study is done to evaluate the FEA stress results at the junctions.

5.6. Discontinuities

Due to abrupt local transitions in the structure and the conical slopes of the cans, it is expected local discontinuity of stresses in some regions of the model. The stress concentration in Figure 43 and Figure 44 may also indicate, though not a sufficient condition, the presence of discontinuities.

Generally, points with high singularity levels present a not well-defined solution. In other words, the mesh refinement process may produce extremely high-stress values (local divergence) at these regions instead of a plateau on a certain amount. As a consequence, the stress levels predicted from FEA at these regions are not physically meaningful [32]. Figure 46 depicts the discontinuity regions on the Design 1 model and Figure 47 shows the same plot for Design 3. The discontinuity measure is unitless and the software documentation gives more details of how the value is calculated [33].

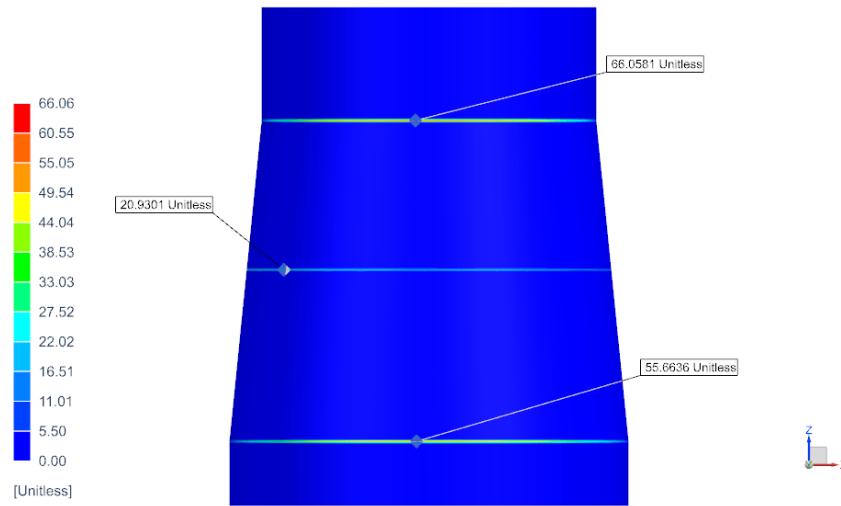


Figure 46: Discontinuities | Design 1 | Front view | Maximum value: 66.06.

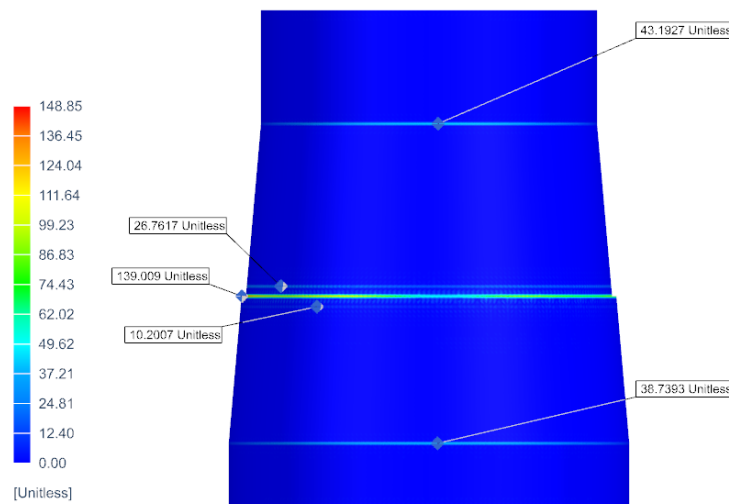


Figure 47: Discontinuities | Design 2 | Front view | Maximum value: 148.85.

As these plots show, the regions of discontinuities are exactly the junctions. Therefore, it is expected that the FE results on the junction may not reflect totally the physical reality of the problem. Constraints, welds, and point loads are also possible causes for the presence of singularities. However, in this project, they seem to be closely related to the connection between different cans which brings along changes in thickness, and

changes in slope. In that case, these factors contribute to generating stress concentration regions. The only exception is the large discontinuity in Figure 47 between Junction 2 and Junction 3. This discontinuity has to do with the geometry of the collar and could be reduced by bringing back the fillets instead of sharp corners that are created to make the mesh generation easier.

Comparing Figure 46 and Figure 47 it is possible to notice that the discontinuity at the conical junctions (Junction 1 and Junction 3 in Figure 46, and Junction 1 and Junction 4 in Figure 47) are relatively greater in Design 1 than in Design 3. That is due to the fact that Design 1 has a larger slope and this not only brings a critical situation in terms of fatigue by increasing the SCF, as seen in section 4, but also increases the singularities and makes it more difficult to find a locally convergent mesh.

Therefore, an approach presented in DNV-RP-C203 [8] is applied to deal with this uncertainty in the junctions by calculating the hot spot stress at tubular and conical connections (junctions) through a linear extrapolation of the FEA stress components, as shown in Figure 48.

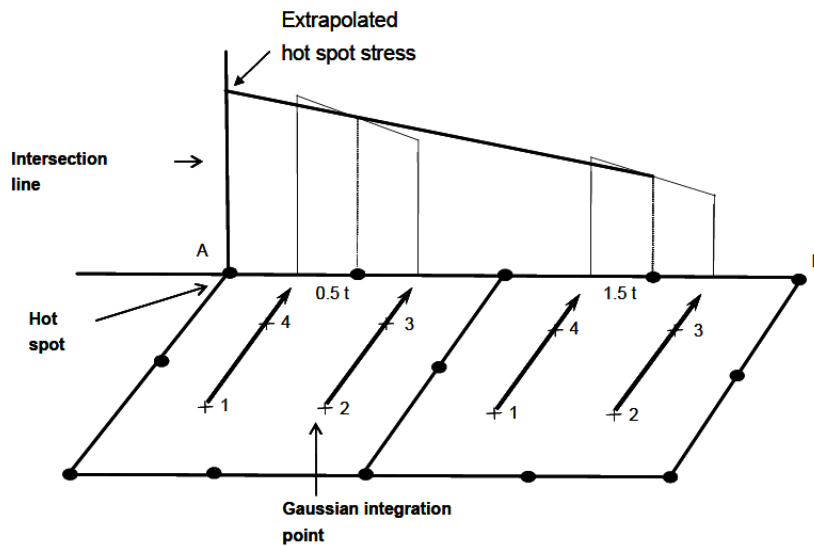


Figure 48: Derivation of hot spot stress through linear extrapolation [8].

For shell elements modelling the linear extrapolation is performed using the intersection line from the read-out points at $0.5t$ and $1.5t$, where t is the thickness of the can. This model considers that no weld is included, as is the case of the geometry drafted in *NX*. Furthermore, one defines the effective hot spot stress $\sigma_{hs,eff}$ as in Equation 89.

$$\sigma_{hs,eff} = \max \begin{cases} \sqrt{\sigma_{\perp}^2 + 0.81\tau_{//}^2} \\ \alpha_c |\sigma_1| \\ \alpha_c |\sigma_2| \end{cases} \quad (89)$$

The parameter α_c is equal to 0.8 and it is given according to the description of the weld

of the hollow profiles. More details are found in Appendix B. Moreover, σ_1 and σ_2 are defined in Equation 90 and Equation 91.

$$\sigma_1 = \frac{\sigma_{\perp} + \sigma_{//}}{2} + \frac{1}{2}\sqrt{(\sigma_{\perp} - \sigma_{//})^2 + 4\tau_{//}^2} \quad (90)$$

$$\sigma_2 = \frac{\sigma_{\perp} - \sigma_{//}}{2} + \frac{1}{2}\sqrt{(\sigma_{\perp} - \sigma_{//})^2 + 4\tau_{//}^2} \quad (91)$$

And σ_{\perp} , $\sigma_{//}$, and $\tau_{//}$ are equivalent to the components σ_z , σ_x , and τ_{zx} from the FEA, respectively. On top of that, the mesh around each one of the junctions is refined by defining a maximum element size of 20 mm (around 30% of the thickness of the thinner can, according to Table 12 and Table 14) in a specific region using the *2D Local Remesh* command in *NX*, as illustrated in Figure 49.

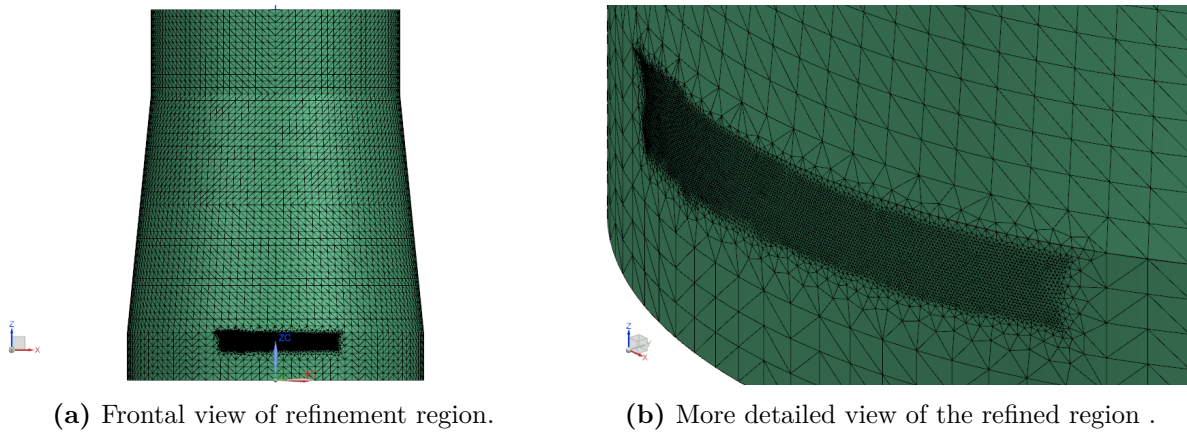


Figure 49: Region around Junction 3 of Design 1 with of local refinement for extrapolation of hot spot stress.

Therefore, the effective hot spot stress is calculated for two read-out points in the refined mesh, and results for the extrapolated junction stress σ_{extrap} are found in Table 32 for Design 1 and in Table 33 for Design 3. The comparison performed in the next section will show that this approach approximates the numerical results to the analytical calculation so that the maximum stress junction is the same in both studies for each one of the designs.

Table 32: Hot spot stresses at junctions of Design 1, in MPa.

Design 1			
	Junction 1	Junction 2	Junction 3
Hot spot stress (σ_{extrap})	113.48	123.63	111.18

Table 33: Hot spot stresses at junctions of Design 3, in MPa.

Design 3				
	Junction 1	Junction 2	Junction 3	Junction 4
Hot spot stress (σ_{extrap})	121.03	130.42	128.25	129.65

6. COMPARISON AND DESIGN DISCUSSION

Given the findings presented in the previous section and the ones obtained using the DNV standards, it is possible to draw some parallels, differences, challenges, and opportunities for improvement. Moreover, the goal is to compare the FEA results in the face of the mechanics of materials findings knowing that they provide a baseline for a critical insight into the numerical investigation.

6.1. Analytical and numerical comparison

The first results that can be compared are the total potential energy and the maximum deflection. The maximum deflection is located at the free end of the TP, as shown in Figure 41, Figure 42 and, according to the analytical result, in Table 16. Table 34 and Table 35 compare the findings from the analytical calculation performed in section 4 and the FE results. On top of that, Figure 50 plots the two results in the same graph. From that, it is possible to notice that, although the TPEs of the finer meshes are slightly higher than the analytical value, in general, with the mesh refinement the TPE converges for that one from the analytical calculation.

Table 34: Comparison between numerical and analytical TPE and deflection results for Design 1.

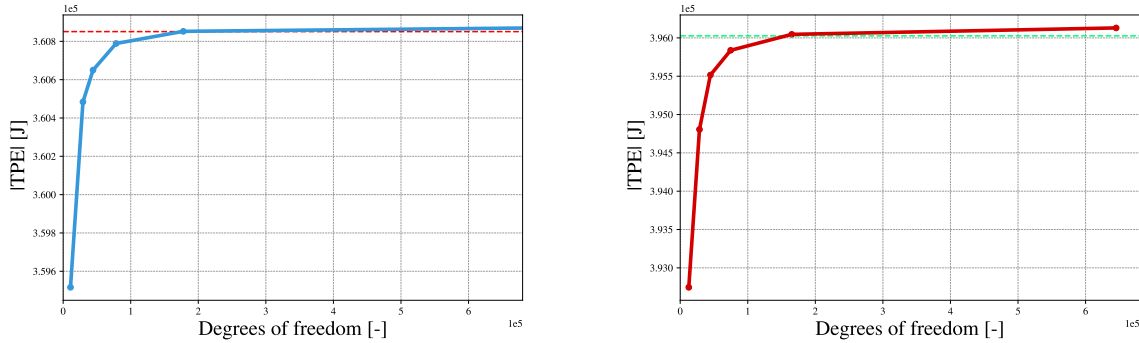
Design 1			
	Analytical	Numerical	Deviation [%]
Maximum deflection (ω_{max}) [mm]	8.23	7.97	3.11
TPE [MPa]	3.61×10^5	3.61×10^5	-0.01

Table 35: Comparison between numerical and analytical TPE and deflection results for Design 3.

Design 3			
	Analytical	Numerical	Deviation [%]
Maximum deflection (ω_{max}) [mm]	9.03	10.63	-17.77
TPE [MPa]	3.96×10^5	3.96×10^5	-0.03

Results from Table 34 indicate a small deviation of the maximum deflection of the TP of Design 1. On the other hand, Table 35 shows a large error associated with the numerical value of the maximum displacement when compared with the one from the analytical calculation. This indicates that the simplifications made on the geometry of Design 3 to calculate the deflection analytically may affect the final outcome. Especially the hypothesis in which an average value for the moment of inertia is used to solve Equation 24. One

possible way to reduce this difference is to elect a representative can and its geometrical properties to calculate the deflection or perform a weighted average of the inertia of each one of the cans. Both approaches would still be a simplification.



(a) Design 1 | Analytical TPE = 3.61×10^5 J. (b) Design 3 | Analytical TPE = 3.96×10^5 J.

Figure 50: TPE convergence plot similar to the ones in Figure 36 and Figure 37 but with the analytical solutions. The red horizontal line in a and the green horizontal line in b are the respective analytical solutions. Both numerical TPEs converge to the analytical value.

Next, the Von Mises stress results along the TPs may be compared. The FE junction stresses are taken from the extrapolated stress approach explained in subsection 5.6, as they reduce the deviation in the junctions. Figure 51 and Figure 52 are diagrams that illustrate the results at representative points along the structure.

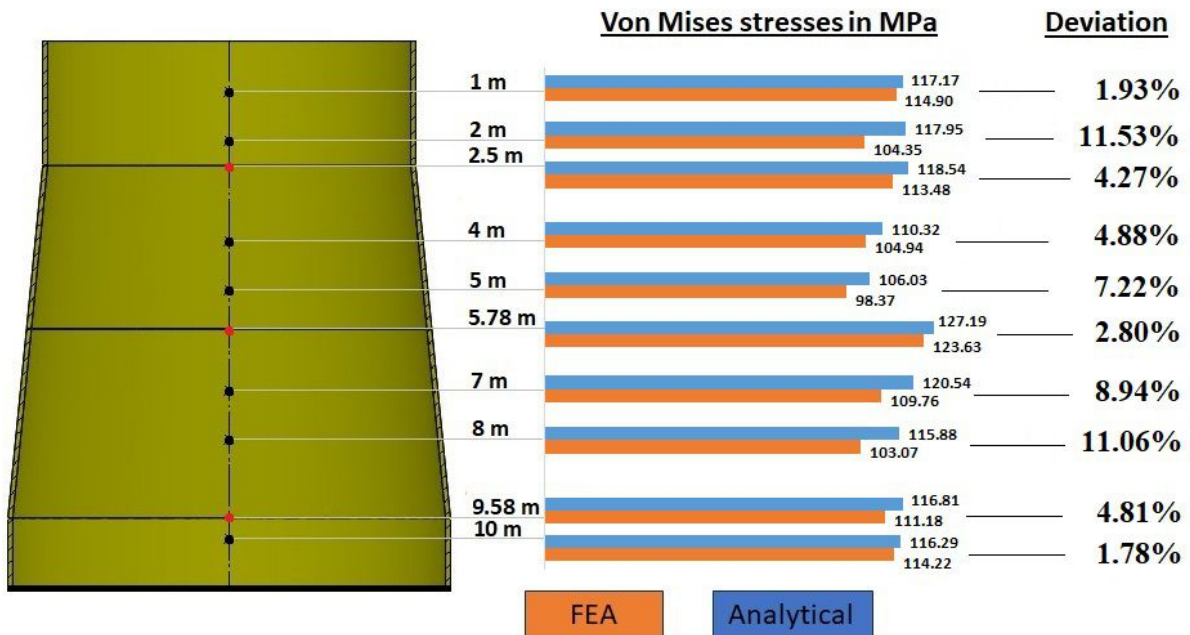


Figure 51: Stress distribution along Design 1 from FEA and analytical approach. Stress is taken in points along the longitudinal axis from 1 meter to 10 meters from the top of the TP. Junction points are in red, and intermediate points along the TP are in black.

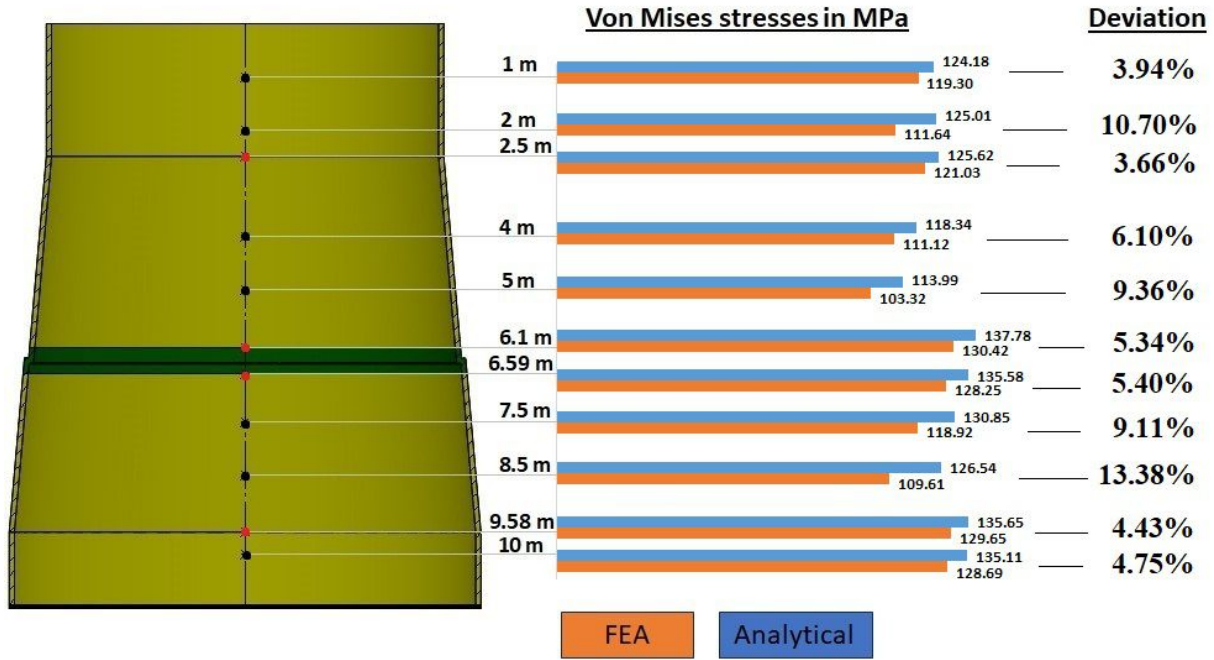


Figure 52: Stress distribution along Design 3 from FEA and analytical approach. Stress is taken in points along the longitudinal axis from 1 meter to 10 meters from the top of the TP. Junction points are in red, and intermediate points along the TP are in black.

Most of the points in Figure 51 and Figure 52 have a deviation smaller than 10%. Points at 2 m in both designs have a larger error due to the proximity to Junction 1 which presents discontinuities as shown in Figure 46 and Figure 47.

Moreover, these results show that the numerical solution for the stress at the top can of both designs does not follow the tendency presented in the analytical approach. In the latter, it is considered that the stresses increase as one moves away from the top of the TP in the z-direction. However, in Figure 45 it is possible to notice that in the middle of the top can, a stress region is formed and, although results do not vary in a large range, the distribution does not follow the expected trend as the analytical one. One of the reasons for this resides in a weakness of the hypothesis of the boundary condition for the analytical calculation. The top can actually is not fixed at its bottom, instead, the can just below it (can_1) is allowed to move.

Nonetheless, in general, the comparison between the results is satisfactory. The location of maximum stress in both approaches is the same (Junction 2 of Design 1 and Junction 2 of Design 3). Further, FE approximation results are smaller than the analytical solution and, through mesh refinement, tend to converge towards it. Triangular elements, in general, are stiffer than quadrilaterals and for this reason, it is expected a stiffer stiffness matrix. Regarding the stresses at the junctions, the results are also satisfactory in terms of deviation and DNV-ST-0126 [19] advises the use of solid elements if one searches for more accurate results. The maximum stress locations also suggest that special care has to

be taken regarding the positioning of longitudinally welded plates that form a single can. Welds aligned with the y-axis should be avoided.

Finally, according to the standards followed for the ULS and FLS calculation, the local stresses are calculated considering cylindrical cross sections, even for conical elements. However, as the slope increases, this approximation becomes weaker due to the fact that other stress components arise. These spurious stress components are observed in the FEA and, in the end, are included in the Von Mises stress calculation, which contributes to more deviations when compared with the analytical results.

6.2. Design outcome

As previously stated, since the FLS analysis and the definition of the thickness of the cans, only two proposed designs remained. In that sense, a direct comparison between them may provide some important insights.

Firstly, based on the geometry of the TPs, Table 12 and Table 14, the total mass of Design 1 and Design 3 can be estimated, as shown in Table 36. This table reveals an advantage of Design 3 over Design 1 for being around 7.5% lighter. Although that is a small margin, it still would mean reduced cost of production.

Table 36: Total mass of Design 1 and Design 3, in tonnes.

Design 1	Design 3
203.22	187.98

Important to highlight that the total mass in Table 36 does not correspond to the mass of the entire TP, but to a section of 11 metres of the TP from its top can. The `bottom_can` element in this project is not represented entirely, instead, just 1.42 meters are considered which is the clearance between the conical section and the top of the TP, according to the constraints of the problem in Table 2 and Figure 2.

When directly compared, the analytical maximum stress results in Design 3 are higher than in Design 1. According to Figure 51, the highest Von Mises stress in Design 1 is 127.19 MPa. In the case of Design 3, Figure 52 shows that the maximum Von Mises stress in this design is 137.78 MPa. One could argue that this is an advantage to Design 1. However, both results are below the limits of the material.

Moreover, from the FEA point of view, Figure 53 also illustrates that stresses in Design 1 are, in general, smaller than in Design 3. Still, both results met the design criteria. So, although some deviation is still present with respect to the analytical solution, the FEA results met the yielding and ultimate strength limits of the steel selected, including for the case of Design 3. On top of that, in the case of a full TP structure, internal reinforcements would provide an even higher resistance. In this project, however, only the primary steel

structure is considered. Therefore, from the structural analysis point of view, both designs are appropriate.

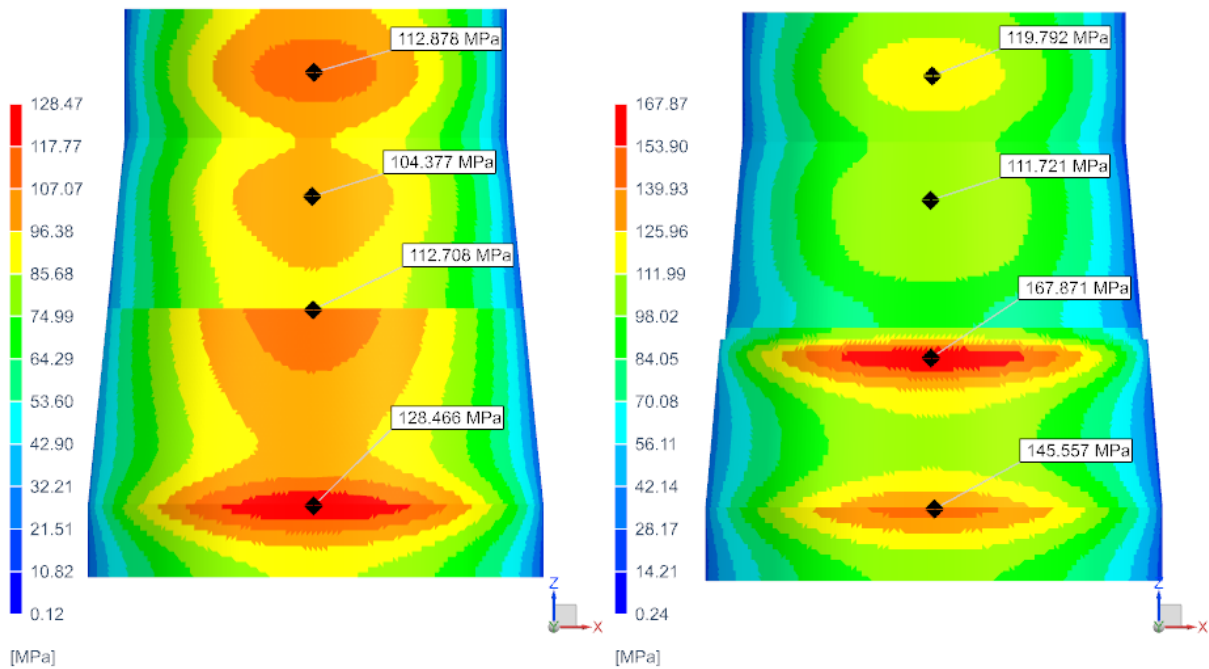


Figure 53: Von Mises stresses at different points in Design 1 (on the left) and Design 3 (on the right). The stresses at the junctions shown here are not the interpolated ones but simply the direct result of the finer mesh simulation. Element stress average and banded display are used.

Nonetheless, some manufacturing challenges may arise for both structures proposed. In the case of Design 1, these challenges are related to the manufacturing of cans with slopes larger than 5° . Whereas in the case of Design 3, the main difficulty may appear in the manufacturing and welding of the collar.

As shown in section 2, in order to assume a truncated cone shape, the steel plate has to be cut in a curved shape. Moreover, the rolling operation usually presents a limitation in terms of the width that the worktable is capable of process. This means that if the plate is too wide one would not be able to pass it through the rollers properly. In the end, the width limitation is translated into a maximum cone surface angle.

Another manufacturing challenge is regarding the manufacturing of the collar element in Design 3 (Figure 54). Due to its large size, shape, and application, the recommended process to obtain this part is high-precision rolling forging, as shown in Figure 55. Unlike casting, the forging process can effectively reduce defects in the microstructure, pores, and shrinkage areas. Moreover, it also yields better mechanical properties.

This process has to perform a precise rolling able to orientate the fibres and confer a compact structure with fine grains that will result in improvements in strength and fatigue resistance. Yet the cost of production may be a disadvantage and has to be properly

evaluated. The welding of this component can be done just as it is in the case of cans. So it is positioned over the welding rollers using overhead bridge cranes and then the circumferential welding is performed.

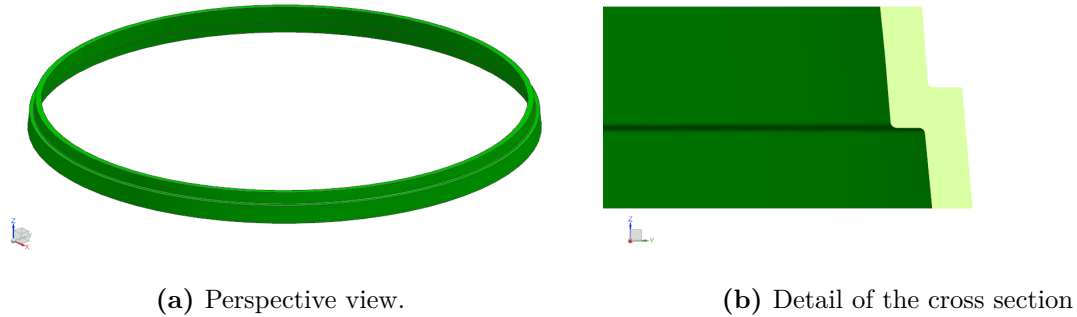


Figure 54: Collar component from Design 3.



Figure 55: Production rolling forging equipment to manufacture rings and collars [9].

Therefore, both designs have their specific challenges to overcome but feasible ways to deal with them. In the end, it is a compromise between the cost of forging the collar in Design 3 and the cost of possibly changing the factory layout and other parameters of rolling bending to account for the large slope in Design 1.

7. CONCLUSION

The design of TP with large slopes requires specific approaches to the evaluation of the limit states. Moreover, challenges arise when it comes to the manufacturing techniques and assembly of the structure. In this project, these aspects are addressed and studied for three specific proposed designs, especially the mechanical behaviour and response of the primary steel structure to a given load condition. Boundary conditions are defined in a simplified approach that does not assume the effect of the monopile or the grouted connection. Instead, the MP-TP connection is considered a fixed end. If compared with other boundary condition models, the one implemented in the project is more conservative from the perspective of generated bending moment and internal reactions. That is due to the fact that the reactions are higher than if it was the case of a boundary condition that assumes the soil stiffness as linear springs, for instance. Future works, however, may investigate a more realistic case in order to obtain a better estimation of the displacement or even modes of vibration.

Important to highlight that the effects of attachments for secondary steel are not included in this study. Some welded attachments, for instance, would increase the number of stress concentration points, create regions where a mesh refinement would be needed, and introduce holes that would reduce the resistance of the cans. Future works may investigate the structure response taking these effects into account, as well as internal reinforcements.

The various cans and conical or tubular junctions of each one of the proposed designs are evaluated in the face of the ultimate limit state and fatigue limit state, according to the applicable standards. One of the designs (Design 2) proved to not comply with manufacturing limits, due to the fact that the slopes are so high that the required thicknesses of the cans would be over the limit of a rolling bending process. The remaining candidates, Design 1 and Design 3, satisfy all the specific design requirements. Further, the mechanical behaviour of cans and junctions of these structures are also evaluated using a numerical approach.

Based on the comparison between the numerical and analytical results, one observes some similarities and it is possible to acquire a visual understanding of how the stresses are distributed along the TPs. It is also possible to identify critical points in the cans and junctions and correlate that with the longitudinal position of the element or its slope. Further studies could be performed in future works by using solid finite elements for the numerical model. For instance, a FEA could be used specifically to study the junctions taking into account the welding geometry and its effects, such as initial imperfections and residual stresses. It is worth remembering that, although some requirements are imposed in the context of a specific site and project, most of the outcomes discussed regarding the effect of large slope cans apply to any other site or load condition.

Finally, the discussion of the main challenges that may arise in the manufacturing of these structures provides some insights and possible solutions to overcome some of these obstacles. Nonetheless, that is a non-exhaustive set of possibilities, and the ongoing advances in manufacturing technology and design requirements from the industry play a significant role in establishing feasible limits and exploring new alternatives.

8. ACKNOWLEDGEMENTS

At first, I thank God for His grace and for being my everlasting source of strength and courage.

I would like to express my heartfelt gratitude to Prof. Phillippe Rigo for granting me the invaluable opportunity to be part of the EMSHIP program. It has been an honor and I hope to proudly represent it throughout my career. Additionally, I would like to extend my special thanks to Christine Reynders for all the support during these two years. Moreover, I truly appreciate the financial support provided by the University of Liège during the program.

I also express my sincere appreciation to the faculty members at the University of Rostock for providing me with one of my best academic experiences in life during the time I spent there. Especially to Dr.-Ing. Thomas Lindemann and Prof. Dr. Patrick Kaeding. Furthermore, I thank Dipl.-Ing. Gunnar Kistner for his support during the elaboration, revision, and discussions of this thesis.

Moreover, I extend my gratitude to ParkWind N.V. for proposing this topic and providing me with the opportunity to learn so much during the last few months. A special thanks to my supervisor, Timothee Piree for his support, attention, and patience. His guidance was critical for me to understand practical aspects of this project and it contributed significantly to the quality of my work. Further, I thank Rasoul Shirzadeh and Eric Degand for their assistance and insightful feedback.

I am grateful to all my classmates who have shared this time with me. Especially Marianna Sipaubá, Samson Alufa, Felipe Alcantara, Tadea Quintuña and Gabriel Vandegar. Their fellowship during these years have made this academic journey more enjoyable and memorable.

Finally, and most importantly, I thank my mother, Francisca de Carvalho, and my stepfather, Atacidio de Carvalho. Even though we are far away, their love and encouragement are the cornerstones of my achievements and the fuel for me to pursue my dreams.

References

- [1] Offshore support structures. <https://www.wind-energy-the-facts.org/offshore-support-structures-7.html>. Accessed on 24/03/2023.
 - [2] Gemini - The building and installation of monopiles. <https://www.geminiwindpark.nl/monopiles--transition-pieces.html#a4>. Accessed on 27/03/2023.
 - [3] Sif Group. Production process world's largest monopile foundation manufacturing plant. <https://www.youtube.com/watch?v=k9Enoa2pNB4>, 2023. Accessed on 06/07/2023.
 - [4] Frustum (truncated cone) calculator. <https://www.hampsonlife.com/conecalculator.php?dT=8500&dB=8900&h=3800.00&form1=Calculate>. Accessed on 06/07/2023.
 - [5] Tom Russell. Sif group starts production of hkn tp-less monopiles. <https://www.offshorewind.biz/2022/10/07/sif-rolls-out-first-hollandse-kust-noord-tp-less-monopiles/>, 2022. Accessed on 07/07/2023.
 - [6] Raquel Redondo and Ali Mehmanparast. Numerical analysis of stress distribution in offshore wind turbine m72 bolted connections. *Metals*, 10(5):689, 2020.
 - [7] Mohamed Shama and Mohamed Shama. Shear stresses in thin-walled structures. *Torsion and Shear Stresses in Ships*, pages 111–132, 2011.
 - [8] DNV. RP-C203: Fatigue design of offshore steel structures. Online, September 2021.
 - [9] Euskalforging. Rectangular ring rolling and profile ring rolling according to customer's specifications. <https://euskalforging.com/en/rolled-rings/types-ring-rolling>. Accessed on 06/07/2023.
 - [10] Sergio Sánchez, José-Santos López-Gutiérrez, Vicente Negro, and M Dolores Esteban. Foundations in offshore wind farms: Evolution, characteristics and range of use. analysis of main dimensional parameters in monopile foundations. *Journal of Marine Science and Engineering*, 7(12):441, 2019.
 - [11] Ana-Maria Chiroasca, Liliana Rusu, and Anca Bleoju. Study on wind farms in the north sea area. *Energy Reports*, 8:162–168, 2022.
 - [12] Laszlo Arany, Subhamoy Bhattacharya, John Macdonald, and SJ Hogan. Design of monopiles for offshore wind turbines in 10 steps. *Soil Dynamics and Earthquake Engineering*, 92:126–152, 2017.
-

-
- [13] Monopiles - BLADT industries. <https://www.bladt.dk/solutions/monopiles/>. Accessed on 27/03/2023.
- [14] Navalia. Navantia-seanergies y windar renovables se adjudican el primer contrato de monopiles xxl para su nueva fábrica de fene (2). <https://www.navalia.es/en/sectors-news/2591-navantia-seanergies-y-windar-renovables-se-adjudican-el-primer-contrato-de-monopiles-xxl-para-su-nueva-fabrica-de-fene-2,2022>. Accessed on 06/07/2023.
- [15] SteelWind. Conical and cylindrical cans and piles. https://www.steelwind-nordham.de/steelwind/produkte/konische_zylindrische_mantelschuesse/index.shtml.en. Accessed on 06/07/2023.
- [16] PEMAMEK. Roller beds: Essential for turning heavy-duty cylindrical workpieces. <https://pemamek.com/discover/roller-beds-essential-for-turning-heavy-duty-cylindrical-workpieces/>, 2019. Accessed on 06/07/2023.
- [17] Offshore Wind Turbine Foundations: Leveling and fixation with hydraulic cylinders. <https://blog.enerpac.com/offshore-wind-turbine-foundations-leveling-and-fixation-with-hydraulic-cylinders/>, 2022. Accessed on 28/03/2023.
- [18] Adnan Memija. Final TP-Less Monopile in place at Hollandse Kust Noord offshore wind farm. <https://www.offshorewind.biz/2023/02/09/final-tp-less-monopile-in-place-at-hollandse-kust-noord-offshore-wind-farm/>, 2023. Accessed on 28/03/2023.
- [19] DNV. ST-0126: Support structures for wind turbines. Online, December 2021.
- [20] DNV. OS-J101: Design of offshore wind turbine structures. Online, May 2014.
- [21] NORSOK. Design of steel structures. *N-004*, June 2021.
- [22] DNV. RP-C202: Buckling strength of shells. Online, September 2021.
- [23] International Electrotechnical Commission (IEC). Iec 61400-3 wind turbines – part 3: design requirements for offshore wind turbines, 2019.
- [24] Anand Natarajan. Damage equivalent load synthesis and stochastic extrapolation for fatigue life validation. *Wind Energy Science*, 7(3):1171–1181, 2022.
- [25] Steffen Aasen. Soil-structure interaction modelling for an offshore wind turbine with monopile foundation. Master’s thesis, Norwegian University of Life Sciences, Ås, 2016.
- [26] J.P. PONTHOT. An introduction to the finite element method. Class notes, 2022.
-

-
- [27] Kuang-Hua Chang. Chapter 7 - Structural analysis. In Kuang-Hua Chang, editor, *e-Design*, pages 325–390. Academic Press, Boston, 2015.
- [28] DNV. RP-0416: Corrosion protection for wind turbines. Online, October 2021.
- [29] FEA Tips. Linear vs quadratic fe elements. <https://featips.com/2019/03/29/linear-vs-quadratic-fe-elements/>. Accessed on 03/07/2023.
- [30] Siemens Industry Software NV. 3-d heterosis shell (t155/t156). https://docs.plm.automation.siemens.com/data_services/resources/nx/1899/nx_help/custom/en_US/samcef_solver_documentation/m003/elem-1556-m003.html#examples, 2018. Accessed on 03/07/2023.
- [31] Wikimedia Commons. Aspect ratio grid. https://commons.wikimedia.org/wiki/File:Aspect_ratio_grid.PNG, 2012. Accessed on 03/07/2023.
- [32] Tony Abbey. Dealing with stress concentrations and singularities. <https://www.digitalengineering247.com/article/dealing-stress-concentrations-singularities>, 2017. Accessed on 04/07/2023.
- [33] Siemens. Element library reference. https://docs.plm.automation.siemens.com/data_services/resources/nxnastran/10/help/en_US/tdocExt/pdf/element.pdf. Accessed on 17/07/2023.
-

APPENDICES

A. DESIGN DRAWINGS

Figure 56 illustrates the space available for sketching the 3 proposed designs. From this available transition region, concepts are created so that they respect the limits of the site stated in subsection 1.2. Furthermore, as explained in section 3 each design is created with one or more aspects in mind regarding manufacturing, slope angle, number of cans, and height of cans.

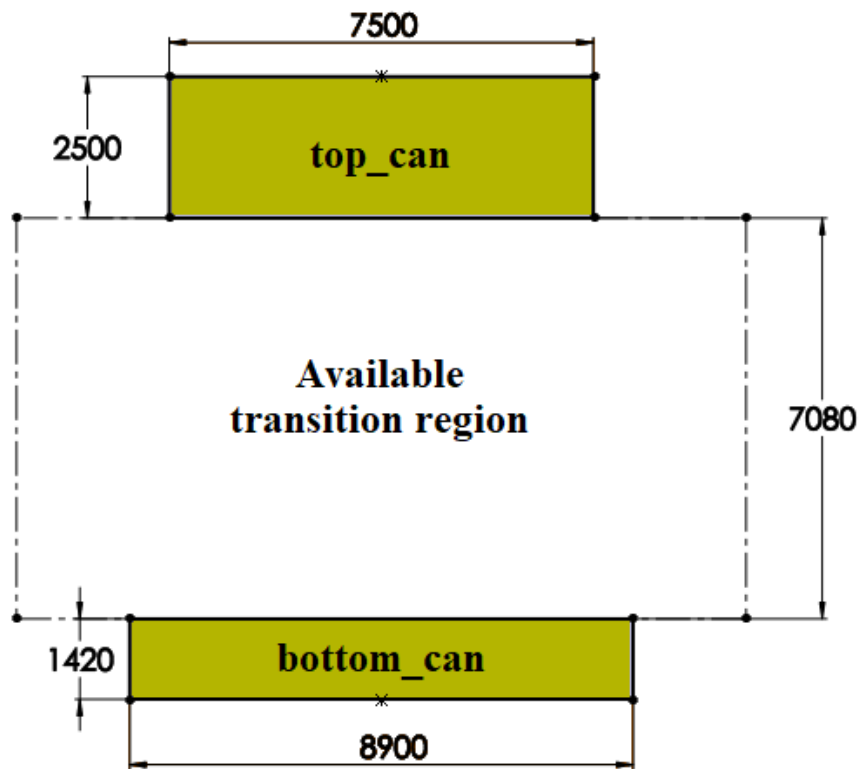
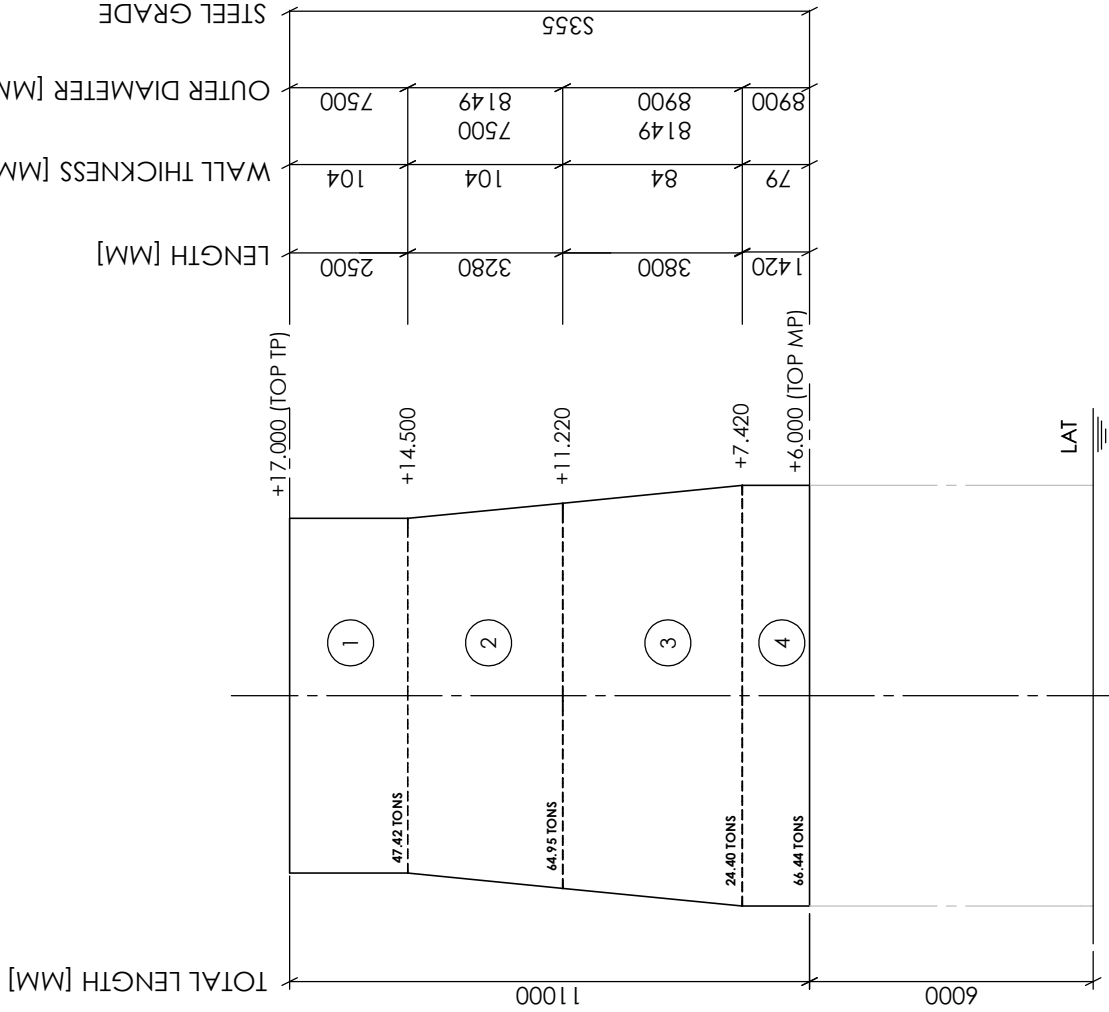


Figure 56: Sketch of the available region. All the 3 proposed concepts of TP are designed along the region shown. The top and bottom cans are the same for all. Dimensions in mm.



Nominal weight cylindrical	[ton]	71.83
Number of cans cylindrical	[-]	2
Nominal weight conical	[ton]	131.39
Number of cans conical	[-]	2
Nominal weight	[ton]	203.22
TP length (from top MP)	[m]	11

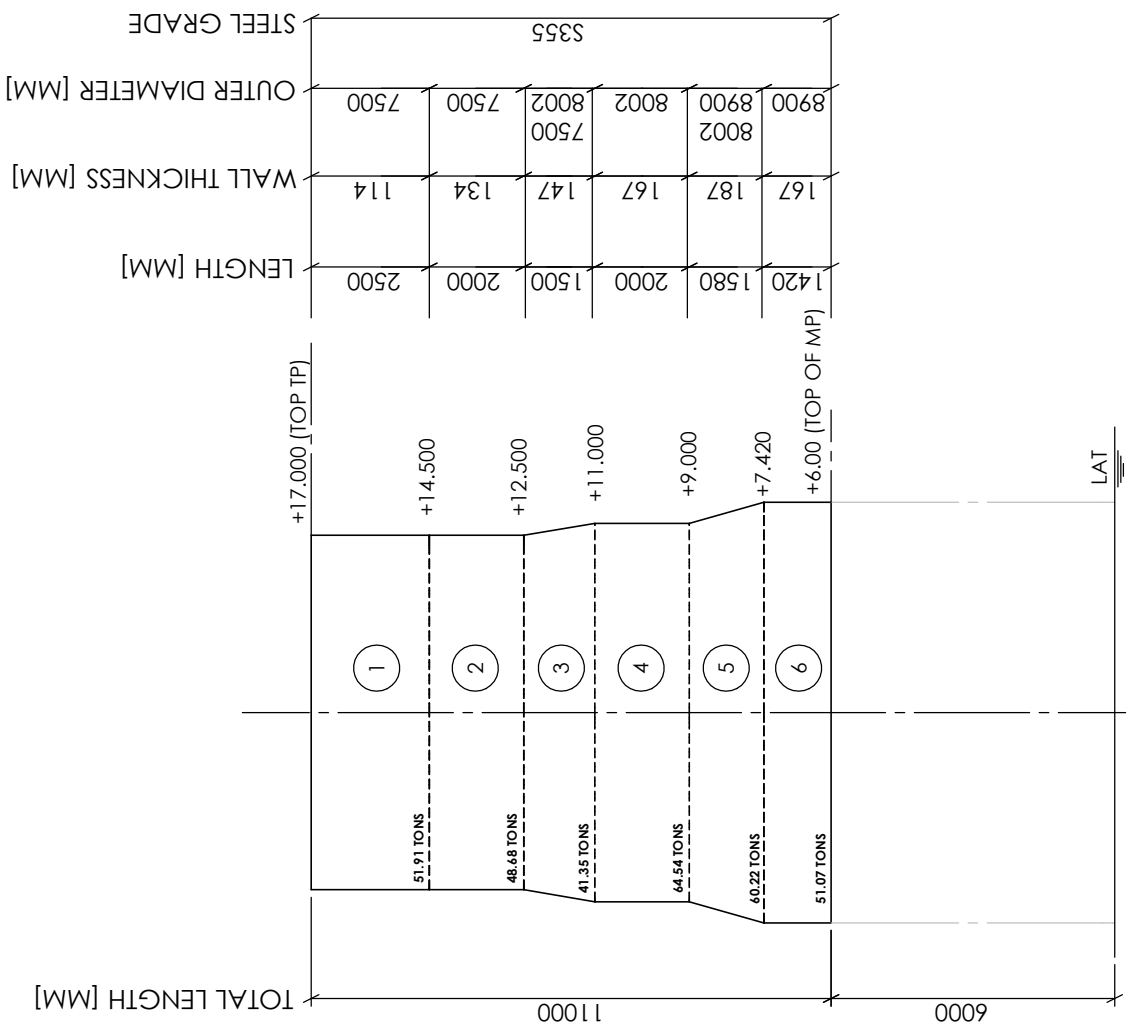
CAN SECTIONS								
Number	Can identification	Bottom elevation [mLAT]	Outside diameter (at can bottom) [mm]	Can height [mm]	Slope [°]	Wall thickness [mm]	Nominal weight [ton]	Steel grade
1	top_can	14.50	7500	2500	0.00	104	47.42	S355
2	can_1	11.22	8149	3280	5.65	104	64.95	S355
3	can_2	7.42	8900	3800	5.65	84	66.44	S355
4	bottom_can	6.00	8900	1420	0.00	79	24.40	S355

Master's thesis: Investigation of the mechanical behaviour of conical cans with large slopes

Approx Weight: 203.22 tons
 Drawing Scale: 1:160
 Sheet Size: A4



Drawn by: Marcos Vieira
 Drawn Date: 19/07/2023
 Checked/Approved by: Timothee Piree
 Drawing Number: Design 1
 Sheet: 1 of 1
 Revision: 1



Nominal weight cylindrical	[fon]	216.21
Number of cans cylindrical	[-]	4
Nominal weight conical	[fon]	101.57
Number of cans conical	[-]	2
Nominal weight	[fon]	317.77
TP length (from top MP)	[m]	11

CAN SECTIONS								
Number	Can identification	Bottom elevation [mLAT]	Outside diameter (at can bottom) [mm]	Can height [mm]	Slope [°]	Wall thickness [mm]	Nominal weight [fon]	Steel grade
1	top_can	14.50	7500	2500	0.00	114	51.91	S355
2	can_1	12.50	7500	2000	0.00	134	48.68	S355
3	can_2	11.00	8002	1500	9.50	147	41.35	S355
4	can_3	9.00	8002	2000	0.00	167	64.54	S355
5	can_4	7.42	8900	1580	15.86	187	60.22	S355
6	bottom_can	6.00	8900	1420	0.00	167	51.07	S355

Master's thesis: Investigation of the mechanical behaviour of conical cans with large slopes

Approx Weight: 317.77 tons
Drawing Scale: 1:160

Sheet Size: A4

Drawn by: Marcos Vieira
Checked/Approved by: Timothee Piree

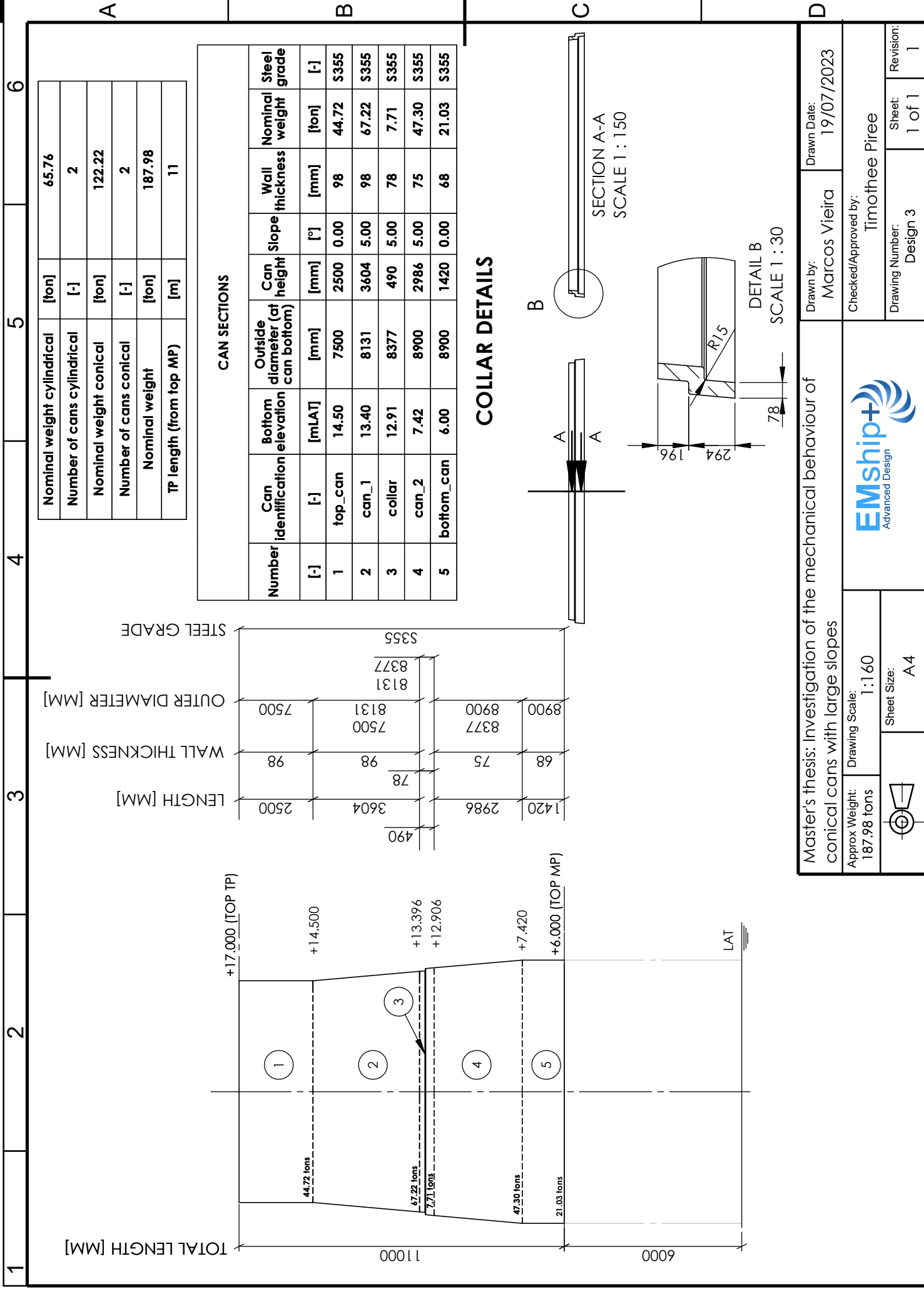
Drawn Date: 19/07/2023

Drawing Number: Design 2

Sheet: 1 of 1

Revision: 1





Master's thesis: Investigation of the mechanical behaviour of conical cans with large slopes

Approx Weight: 187.98 tons

Drawing Scale: 1:160

Sheet Size: A4

Drawn by: Marcos Vieira

Checked/Approved by: Timothee Piree

Drawing Number: Design 3

Sheet: 1 of 1

Revision: 1

Drawn Date: 19/07/2023

B. TABLES AND SPREADSHEETS

B.1. Main dimensions

Table 37: Design 1 - main dimensions and components

Component	Outer diameter (at top junction) [mm]	Outer diameter (at bottom junction) [mm]	Tp [mm]	Height [mm]	Slope [°]	Volume [m3]	Weight [ton]	Nominal thickness [mm]
top_can	7500	7500	102.28	2500	0.00	6.04	47.42	104
can1	7500	8149	102.28	3280	5.65	8.27	64.95	104
can2	8149	8900	82.28	3800	5.65	8.46	66.44	84
bottom_can	8900	8900	77.28	1420	0.00	3.11	24.40	79
	Steel density [kg/m ³]					7850		
	Total weight [ton]					203.22		

Table 38: Design 2 - main dimensions and components

Component	Outer diameter (at top junction) [mm]	Outer diameter (at bottom junction) [mm]	Tp [mm]	Height [mm]	Slope [°]	Volume [m3]	Weight [ton]	Nominal thickness [mm]
top_can	7500.00	7500.00	112.28	2500.00	0.00	6.61	51.91	114
can_1	7500.00	7500.00	132.28	2000.00	0.00	6.20	48.68	134
can_2	7500.00	8002.02	145.28	1500.00	9.50	5.27	41.35	147
can_3	8002.02	8002.02	165.28	2000.00	0.00	8.22	64.54	167
can_4	8002.02	8900.00	185.28	1580.00	15.86	7.67	60.22	187
bottom_can	8900.00	8900.00	165.28	1420.00	0.00	6.51	51.07	167
	Steel density [kg/m ³]					7850		
	Total weight [ton]					187.98		

Table 39: Design 3 - main dimensions and components

Component	Outer diameter (at top junction) [mm]	Outer diameter (at bottom junction) [mm]	Tp [mm]	Height [mm]	Slope [°]	Volume [m3]	Weight [ton]	Nominal thickness [mm]
top_can	7500.00	7500.00	96.28	2500.00	0.00	5.70	44.72	98
can_1	7500.00	8130.62	96.28	3604.00	5.00	8.56	67.22	98
collar	8130.62	8377.52	76.28	490.00	5.00	0.98	7.71	78
can_2	8377.52	8900.00	73.28	2986.00	5.00	6.03	47.30	75
bottom_can	8900.00	8900.00	66.28	1420.00	0.00	2.68	21.03	68
	Steel density [kg/m ³]					7850		
	Total weight [ton]					187.98		

B.2. Stress distribution

Table 40: Analytical stress distribution in the junctions

	Design 1					Design 2					Design 3						
	Junction 1	Junction 2	Junction 3	Junction 1	Junction 2	Junction 3	Junction 1	Junction 2	Junction 3	Junction 1	Junction 2	Junction 3	Junction 1	Junction 2	Junction 3	Junction 4	Junction 5
M_x [N.m]	474000000	474000000	474000000	474000000	474000000	474000000	474000000	474000000	474000000	474000000	474000000	474000000	474000000	474000000	474000000	474000000	474000000
F_x [N]	34060000	34060000	34060000	34060000	34060000	34060000	34060000	34060000	34060000	34060000	34060000	34060000	34060000	34060000	34060000	34060000	34060000
F_z [N]	-16850220.44	-17487352.32	-18139143.96	-16894263.68	-17371853.48	-17777492.58	-18410596.7	-19001311.7	-16823736.43	-17483161.33	-17558761.69	-18022746.85	-16823736.43	-17483161.33	-17558761.69	-18022746.85	-18022746.85
M_z [N.m]	-33737000	-33737000	-33737000	-33737000	-33737000	-33737000	-33737000	-33737000	-33737000	-33737000	-33737000	-33737000	-33737000	-33737000	-33737000	-33737000	-33737000
Diameter_outer [m]	7.50	8.15	8.90	7.50	7.50	8.00	8.00	8.00	8.00	8.00	8.00	8.00	7.50	8.13	8.38	8.90	8.90
Diameter_inner [m]	7.30	7.98	8.75	7.28	7.24	7.71	7.67	7.67	7.67	7.67	7.67	7.67	7.31	7.98	8.23	8.77	8.77
Radius_outer [m]	3.75	4.07429	4.45	3.75	3.75	4.00101	4.00101	4.00101	4.00101	4.00101	4.00101	4.00101	3.75	4.06531	4.18876	4.45	4.45
Radius_inner [m]	3.65	3.99	4.37	3.64	3.62	3.86	3.84	3.84	3.84	3.84	3.84	3.84	3.65	3.99	4.12	4.38	4.38
Thickness [m]	0.10	0.08	0.08	0.11	0.13	0.15	0.17	0.17	0.17	0.17	0.15	0.17	0.10	0.08	0.07	0.07	0.07
Second moment of inertia (I) [m ⁴]	16.26	16.96	20.84	17.78	20.78	27.68	31.25	43.27	15.35	15.65	16.48	17.94	15.35	15.65	16.48	17.94	17.94
First moment of inertia (S_{max}) [m ³]	2.80	2.68	3.01	3.06	3.59	4.48	5.08	6.31	2.64	2.47	2.53	2.59	2.64	2.47	2.53	2.59	2.59
Polar moment of inertia (J) [m ⁴]	32.53	33.92	41.68	35.56	41.56	55.36	62.50	86.54	30.69	31.30	32.96	35.88	30.69	31.30	32.96	35.88	35.88
Longitudinal position (L_z) [m]	2.5	5.78	9.58	2.5	4.5	6	8	9.58	2.5	6.104	6.594	9.58	2.5	6.104	6.594	9.58	9.58
Area [m ²]	2.38	2.08	2.14	2.61	3.06	3.59	4.07	4.54	2.24	1.93	1.91	1.84	2.24	1.93	1.91	1.84	1.84
M_x at L_z [N.m]	85150000	19686680	32629480	85150000	153270000	204360000	272480000	326294800	85150000	20790224	22459164	32629480	85150000	20790224	22459164	32629480	32629480
σ_{zM} [MPa]	-111.26	-118.61	-108.17	-101.76	-88.30	-71.47	-64.17	-52.11	-117.91	-128.51	-126.19	-125.66	-117.91	-128.51	-126.19	-125.66	-125.66
σ_{zN} [MPa]	-7.09	-8.39	-8.47	-6.48	-5.67	-4.96	-4.52	-4.19	-7.51	-9.06	-9.19	-9.80	-7.51	-9.06	-9.19	-9.80	-9.80
Normal stress (σ_z) [MPa]	-118.35	-126.99	-116.64	-108.24	-93.97	-76.43	-68.70	-56.29	-125.42	-137.57	-135.37	-135.46	-125.42	-137.57	-135.37	-135.46	-135.46
τ_{zyV}	2.87	3.27	3.18	2.61	2.22	1.90	1.67	1.50	3.04	3.53	3.56	3.70	3.04	3.53	3.56	3.70	3.70
τ_{zyVmax}	3.89	4.05	3.60	3.56	3.04	2.44	2.16	1.73	4.12	4.38	4.29	4.18	4.12	4.38	4.29	4.18	4.18
Shear stress (τ_{zy}) [MPa]	3.89	4.05	3.60	3.56	3.04	2.44	2.16	1.73	4.12	4.38	4.29	4.18	4.12	4.38	4.29	4.18	4.18
Von Mises [MPa]	118.54	127.19	116.81	108.42	94.12	76.55	68.80	56.37	125.62	137.78	135.58	135.65	125.62	137.78	135.58	135.65	135.65

B.3. Fatigue Limit State

Table 41: Design 1 - SCF calculations

	top_can	can_1	can_1	can_2	can_2	bottom_can
	junction1		junction2		junction3	
	Conical		Tubular		Conical	
δ_m (eccentricity) [mm]	-	-	3	3	-	-
δ_0 (misalignment) [mm]	-	-	0	0	-	-
α	-	-	0.07	0.12	-	-
α (inner diameter)			0.07	0.12		
L	-	-	92.275	92.275	-	-
D	-	-	8148.58	8148.58	-	-
d (inner diameter)			7944.03	7984.03		
T	-	-	102.28	82.28	-	-
t	-	-	82.28	102.28	-	-
δ_t	-	-	10	10	-	-
β	-	-	2.75	2.86	-	-
β (inner diameter)			2.77	2.87		
SCF	1.72	1.72	1.31	1.44	1.91	1.81

SCFs summary

	junction1		junction2		junction3	
	top_can	can_1	can_1	can_2	can_2	bottom_can
Outer diameter	1.72	1.72	1.31	1.44	1.91	1.81
Inner diameter	1.71	1.71	1.00	1.00	1.91	1.80

Table 42: Design 2 - SCF calculations

	top_can	can_1	can_1	can_2	can_2	can_3	can_3	can_4	can_4	bottom_can
	Junction1		Junction2		Junction3		Junction4		Junction5	
	Tubular		Conical		Conical		Conical		Conical	
δ_m (eccentricity) [mm]	3	3	-	-	-	-	-	-	-	-
δ_0 (misalignment) [mm]	0	0	-	-	-	-	-	-	-	-
α	0.139	0.093	-	-	-	-	-	-	-	-
L	122.275	122.275	-	-	-	-	-	-	-	-
D	7500.00	7500.00	-	-	-	-	-	-	-	-
T	112.28	132.28	-	-	-	-	-	-	-	-
t	132.28	112.28	-	-	-	-	-	-	-	-
δ_t	10	10	-	-	-	-	-	-	-	-
β	3.045853127	2.948962632	-	-	-	-	-	-	-	-
SCF	1.50	1.35	2.10	1.91	2.24	1.96	2.45	2.82	2.45	2.82

SCFs summary

	Junction1		Junction2		Junction3		Junction4		Junction5	
	top_can	can_1	can_1	can_2	can_2	can_3	can_3	can_4	can_4	bottom_can
Outer diameter	1.50	1.35	2.10	1.91	2.24	1.96	2.45	2.82	2.45	2.82

Table 43: Design 3 - SCF calculations

	top_can	can_1	can_1	collar	collar	can_2	can_2	bottom_can
	Junction1		Junction2		Junction3		Junction4	
	Conical		Tubular		Tubular		Conical	
δ_m (eccentricity) [mm]	-	-	3	3	3	3	-	-
δ_0 (misalignment) [mm]	-	-	0	0	0	0	-	-
α	-	-	0.069107792	0.116937341	0.082158785	0.086848468	-	-
α (inner diameter)	-	-	0.069833558	0.118136008	0.082904188	0.087618213	-	-
L	-	-	86.275	86.275	74.775	74.775	-	-
D	-	-	8130.62	8130.62	8377.52	8377.52	-	-
d (inner diameter)	-	-	7938.07	7978.07	8224.97	8230.97	-	-
T	-	-	96.28	76.28	76.28	73.28	-	-
t	-	-	76.28	96.28	73.28	73.28	-	-
δ_t	-	-	10	10	1.5	0	-	-
β	-	-	2.722778458	2.827273777	2.694082723	2.694082723	-	-
β (inner diameter)	-	-	2.732871578	2.836445432	2.701498908	2.70120312	-	-
SCF	1.66	1.66	1.33	1.47	1.16	1.11	1.72	1.88

SCFs summary								
	junction1		junction2		junction3		junction4	
	top_can	can_1	can_1	collar	collar	can_2	can_2	bottom_can
Outer diameter	1.66	1.66	1.33	1.47	1.16	1.11	1.72	1.88
Inner diameter	1.65	1.65	1.33	1.47	1.16	1.11	1.72	1.88

Table 44: Design 1: S-N curve calculation.

	top_can	can_1	can_1	can_2	can_2	bottom_can
	junction1		junction2		junction3	
Diameter [mm]	7500.00		8148.58		8900.00	
x [m]	3.75		4.07		4.45	
z [m]	2.5		5.78		9.58	
Second moment of inertia [m ⁴]	16.26	16.26	20.93	16.96	22.15	20.84
First moment of inertia [m ³]	2.80	2.80	3.31	2.68	3.20	3.01
Polar moment of inertia [m ⁴]	32.53	32.53	41.85	33.92	44.31	41.68
Generated moment (M_e) [N.m]	2180000		5040160		8353760	
Normal stress from M_y [MPa]	0.50	0.50	0.98	1.21	1.68	1.78
Normal stress from Equiv_bending [MPa]	16.53	16.53	13.96	17.23	14.40	15.31
Total normal stress [MPa]	17.04	17.04	14.94	18.44	16.08	17.09
Shear stress (from shear force) [MPa]	0.73	0.73	0.67	0.84	0.77	0.81
Shear stress (from torsion) [MPa]	3.06	3.06	2.58	3.19	2.67	2.83
Von Mises stress [MPa]	18.26	18.26	15.97	19.71	17.14	18.22
Hot spot stress range [MPa]	31.38	31.38	20.96	28.39	32.83	32.93
Fatigue limit (at 10 ⁷)	52.63	52.63	52.63	52.63	52.63	52.63
log(a)	15.606	15.606	15.606	15.606	15.606	15.606
m	5	5	5	5	5	5
n	10000000	10000000	10000000	10000000	10000000	10000000
t_{ref}	32	32	32	32	32	32
k	0.25	0.25	0.25	0.25	0.25	0.25
N	3.11E+07	3.11E+07	2.33E+08	6.72E+07	3.25E+07	3.46E+07
D	0.32	0.32	0.04	0.15	0.31	0.29
Theoretical fatigue life (L_t) [years]	31.5	31.5	31.5	31.5	31.5	31.5
Design fatigue factor (DFF)	3	3	3	3	3	3
Criteria 1: $D < 1$	ok	ok	ok	ok	ok	ok
η	0.333333333	0.333333333	0.333333333	0.333333333	0.333333333	0.333333333
Criteria 2: $D > \eta$	ok	ok	ok	ok	ok	ok
Calculated fatigue life (L_c) [years]	98	98	735	212	102	109

Table 45: Design 2: S-N curve calculation.

	top_can	can_1	can_1	can_2	can_2	can_3	can_3	can_4	can_4	bottom_can
	Junction1		Junction2		Junction3		Junction4		Junction5	
Diameter [mm]	7500.00		7500.00		8002.02		8002.02		8900.00	
x [m]	3.75		3.75		4.00		4.00		4.45	
z [m]	2.5		4.5		6		8		9.58	
Second moment of inertia [m ⁴]	17.78	20.78	20.78	22.70	27.68	31.25	31.25	34.77	48.18	43.27
First moment of inertia [m ³]	3.06	3.59	3.59	3.93	4.48	5.08	5.08	5.66	7.04	6.31
Polar moment of inertia [m ⁴]	35.56		41.56		55.36		62.50		96.35	
Generated moment (M_x) [N.m]	2180000		3924000		5232000		6976000		8353760	
Normal stress from M_y [MPa]	0.46	0.39	0.71	0.65	0.76	0.67	0.89	0.80	0.77	0.86
Normal stress from Equiv_bending [MPa]	15.12	12.94	12.94	11.84	10.37	9.18	9.18	8.25	6.62	7.37
Total normal stress [MPa]	15.58	13.33	13.65	12.49	11.12	9.85	10.07	9.05	7.40	8.23
Shear stress (from shear force) [MPa]	0.67	0.57	0.57	0.52	0.49	0.43	0.43	0.38	0.34	0.38
Shear stress (from torsion) [MPa]	2.80	2.39	2.39	2.19	1.92	1.70	1.70	1.53	1.23	1.36
Von Mises stress [MPa]	16.70	14.29	14.58	13.34	11.88	10.52	10.73	9.64	7.88	8.77
Hot spot stress range [MPa]	25.04937489	19.24992454	30.55018299	25.46129614	26.59727044	20.58873967	26.27610696	27.20122696	19.30086037	24.75728239
Fatigue limit (at 10 ⁷)	52.63	52.63	52.63	52.63	52.63	52.63	52.63	52.63	52.63	52.63
log(a)	15.606	15.606	15.606	15.606	15.606	15.606	15.606	15.606	15.606	15.606
m	5	5	5	5	5	5	5	5	5	5
n	10000000	10000000	10000000	10000000	10000000	10000000	10000000	10000000	10000000	10000000
t_{ref}	32	32	32	32	32	32	32	32	32	32
k	0.25	0.25	0.25	0.25	0.25	0.25	0.25	0.25	0.25	0.25
N	85231313.44	318008322.6	31587449.72	78556314.83	63153626.94	227213866.3	67108655.5	56447039.9	313834221.4	90379262.16
D	0.117327771	0.031445718	0.31658143	0.127297214	0.158344033	0.044011398	0.149012075	0.177157208	0.031863957	0.110644851
Theoretical fatigue life (L_t) [years]	31.5	31.5	31.5	31.5	31.5	31.5	31.5	31.5	31.5	31.5
Design fatigue factor (DFF)	3	3	3	3	3	3	3	3	3	3
Criteria 1: $D < 1$	ok	ok	ok	ok	ok	ok	ok	ok	ok	ok
η	0.333333333	0.333333333	0.333333333	0.333333333	0.333333333	0.333333333	0.333333333	0.333333333	0.333333333	0.333333333
Criteria 2: $D > \eta$	ok	ok	ok	ok	ok	ok	ok	ok	ok	ok
Calculated fatigue life (L_c) [years]	268.4786373	1001.726216	99.50046662	247.4523917	198.9339249	715.7236789	211.3922648	177.8081757	988.5777975	284.6946758

Table 46: Design 3: S-N curve calculation.

	top_can	can_1	can_1	collar	collar	can_2	can_2	bottom_can
	Junction1		Junction2		Junction3		Junction4	
Diameter [mm]	7500.00		8130.62		8377.52		8900.00	
x [m]	3.75		4.07		4.19		4.45	
z [m]	2.5		6.104		6.594		9.58	
Second moment of inertia [m ⁴]	15.35	15.35	19.61	15.65	17.14	16.48	19.79	17.94
First moment of inertia [m ³]	2.64	2.64	3.11	2.47	2.63	2.53	2.85	2.59
Polar moment of inertia [m ⁴]	30.69		39.22		34.27		39.58	
Generated moment (M_x) [N.m]	2180000		5322688		5749968		8353760	
Normal stress from M_y [MPa]	0.53	0.53	1.10	1.38	1.41	1.46	1.88	2.07
Normal stress from Equiv_bending [MPa]	17.52	17.52	13.71	17.18	15.69	16.32	13.59	14.99
Total normal stress [MPa]	18.06	18.06	14.82	18.56	17.10	17.78	15.47	17.06
Shear stress (from shear force) [MPa]	0.78	0.78	0.72	0.90	0.88	0.91	0.86	0.95
Shear stress (from torsion) [MPa]	3.24	3.24	2.75	3.45	3.24	3.37	2.98	3.29
Von Mises stress [MPa]	19.35	19.35	15.99	20.03	18.53	19.27	16.84	18.57
Hot spot stress range [MPa]	32.03	32.03	21.28	29.55	21.50	21.44	29.00	34.97
Fatigue limit (at 10 ⁷)	52.63	52.63	52.63	52.63	52.63	52.63	52.63	52.63
log(a)	15.606	15.606	15.606	15.606	15.606	15.606	15.606	15.606
m	5	5	5	5	5	5	5	5
n	10000000	10000000	10000000	10000000	10000000	10000000	10000000	10000000
t_{ref}	32	32	32	32	32	32	32	32
k	0.25	0.25	0.25	0.25	0.25	0.25	0.25	0.25
N	3.02E+07	3.02E+07	2.34E+08	6.05E+07	2.97E+08	3.17E+08	6.99E+07	3.11E+07
D	0.33	0.33	0.04	0.17	0.03	0.03	0.14	0.32
Theoretical fatigue life (L_t) [years]	31.5	31.5	31.5	31.5	31.5	31.5	31.5	31.5
Design fatigue factor (DFF)	3	3	3	3	3	3	3	3
Criteria 1: $D < 1$	ok	ok	ok	ok	ok	ok	ok	ok
η	0.333333333	0.333333333	0.333333333	0.333333333	0.333333333	0.333333333	0.333333333	0.333333333
Criteria 2: $D > \eta$	ok	ok	ok	ok	ok	ok	ok	ok
Calculated fatigue life (L_c) [years]	95	95	736	191	934	997	220	98

S-N curve	$N \leq 10^7$ cycles		$N > 10^7$ cycles $\log \bar{a}_2$ $m_2 = 5.0$	Fatigue limit at 10^7 cycles *)	Thickness exponent k	Structural stress concentration embedded in the detail (S-N class), ref. also equation (2.3.2)
	m_1	$\log \bar{a}_1$				
B1	4.0	15.117	17.146	106.97	0	
B2	4.0	14.885	16.856	93.59	0	
C	3.0	12.592	16.320	73.10	0.05	
C1	3.0	12.449	16.081	65.50	0.10	
C2	3.0	12.301	15.835	58.48	0.15	
D	3.0	12.164	15.606	52.63	0.20	1.00
E	3.0	12.010	15.350	46.78	0.20	1.13
F	3.0	11.855	15.091	41.52	0.25	1.27
F1	3.0	11.699	14.832	36.84	0.25	1.43
F3	3.0	11.546	14.576	32.75	0.25	1.61
G	3.0	11.398	14.330	29.24	0.25	1.80
W1	3.0	11.261	14.101	26.32	0.25	2.00
W2	3.0	11.107	13.845	23.39	0.25	2.25
W3	3.0	10.970	13.617	21.05	0.25	2.50
T	3.0	12.164	15.606	52.63	0.25 for SCF ≤ 10.0 0.30 for SCF > 10.0	1.00

*) see also [2.11]

Figure 57: S-N curves parameters. The one used for tubular and conical junctions is the curve T [8].

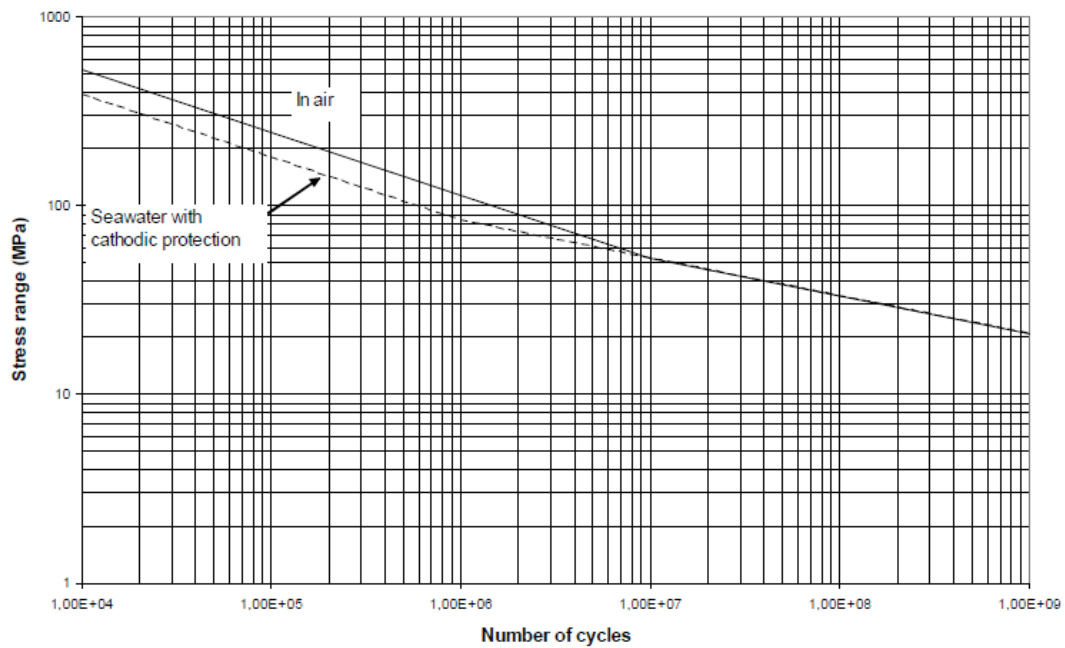


Figure 58: S-N curve for tubular and conical joints [8].

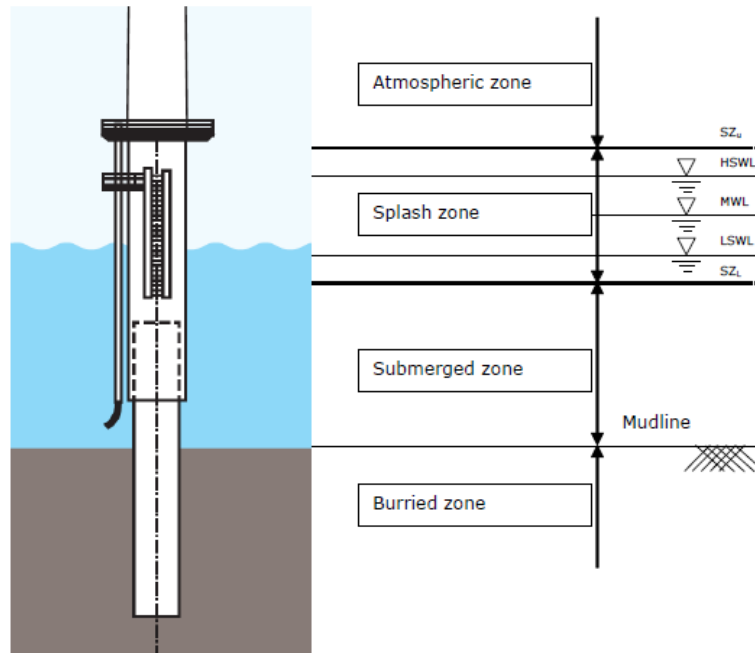


Figure 59: Representation of levels and zones in seawater environment [28].

Location	Accessibility for inspection and repair of initial fatigue and coating damages ²⁾	S-N curve ⁵⁾	Minimum DFF ⁶⁾
Atmospheric zone	No	In air for coated surfaces free corrosion for surfaces protected by corrosion allowance, only ⁴⁾	3
	Yes		1
Upper splash zone (above MWL) ¹⁾	No	Combination of in air and free corrosion curves ^{3) 4)}	3
	Yes		2
Lower splash zone (below MWL) ¹⁾	No	In seawater for surfaces with cathodic protection Free corrosion for surfaces protected by corrosion allowance, only ⁴⁾	3
	Yes		2
Submerged zone	No	In seawater for surfaces with cathodic protection Free corrosion for surfaces protected by corrosion allowance, only ⁴⁾	3
	Yes		2
Scour zone	No	In seawater	3
Below scour zone	No	In seawater	3

Note:

- Splash zone definition according to DNVGL-RP-0416.
- If the designer considers the steel surface accessible for inspection and repair of initial fatigue damage and coating, this shall be documented through qualified procedures for these activities. See also [4.16] and Sec.9.
- The basic S-N curve for unprotected steel in the splash zone is the curve marked free corrosion. The basic S-N curve for coated steel is the curve marked in air. It is acceptable to carry out fatigue life calculations in the splash zone based on accumulated damage for steel considering the probable coating conditions throughout the design life - intact, damaged and repaired. The coating conditions shall refer to an inspection and repair plan as specified in Sec.9.
- When free corrosion S-N curves are applied in design, the full benefit of potential grinding of welds as outlined in [4.13.5] cannot be expected and therefore may not be taken into account. The effect of free corrosion on a ground weld may be accounted for by downgrading the S-N curve one class and applying the S-N curves for in seawater for free corrosion.
- Shear keys within grouted connections may be designed assuming S-N curves marked in air.
- According to the chosen DFF, an inspection program according to [9.3] will be required.

Figure 60: S-N curves and design fatigue factors (DFF) for different locations [19]. The TPs in this project are considered as being located at the upper splash zone.

Table A-9 Hollow sections (Continued)

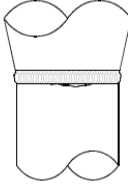
Detail category	Constructional details	Description	Requirement
C1		8. Circumferential butt welds between tubular and conical sections, weld made from both sides dressed flush.	8., 9., 10., and 11. – The applied stress must also include the stress concentration factor due to the overall form of the joint, ref. section [3.3.9]. – The requirements to the corresponding detail category in Table A-5 apply.
D		9. Circumferential butt welds between tubular and conical sections, weld made from both sides.	
E		10. Circumferential butt welds between tubular and conical sections, weld made from both sides made at site.	
F		11. Circumferential butt welds between tubular and conical sections, weld made from one side on a backing bar.	

Figure 61: Weld description of conical hollow profiles for determining the parameter α_c for hot spot stress calculation according to DNV-RP-C203 [8].

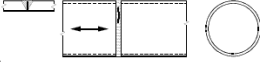
C1		3. Circumferential butt weld made from both sides dressed flush.	3., 4., 5. and 6. – The applied stress must include the stress concentration factor to allow for any thickness change and for fabrication tolerances, ref. section [3.3.7]. – The requirements to the corresponding detail category in Table A-5 apply.
D		4. Circumferential butt weld made from both sides.	
E		5. Circumferential butt weld made from both sides made at site.	
F		6. Circumferential butt weld made from one side on a backing bar.	

Figure 62: Weld description of tubular hollow profiles for determining the parameter α_c for hot spot stress calculation according to DNV-RP-C203 [8].

B.4. Ultimate Limit State

Table 47: ULS calculation | Design 1 | Reduced thickness.

	top_can	can_1	can_1	can_2	can_2	bottom_can
	Conical		Tubular		Conical	
Material factor (γ_m)	1.15	1.15	1.15	1.15	1.15	1.15
Outer diameter [m]	7.5	7.50	8.15	8.15	8.90	8.9
Expected maximum corrosion rate (V_corr) [mm/year]	0.3	0.3	0.3	0.3	0.3	0.3
Design useful life of the coating (Tc) [years]	20	20	20	20	20	20
Design life of the structure (Td) [years]	31.5	31.5	31.5	31.5	31.5	31.5
Real thickness [m]	0.10	0.10	0.10	0.08	0.08	0.08
Corrosion allowance (CA) [m]	0.0035	0.0035	0.0035	0.0035	0.0035	0.0035
Thickness (t_p) [m]	0.10	0.10	0.10	0.08	0.08	0.07
Area [m ²]	2.30	2.30	2.50	2.00	2.18	2.05

Table 48: ULS calculation | Design 1 | Conical connections.

Component	Conical connection: junction1		Conical connection: junction3	
	top_can	can_1	can_2	bottom_can
Design axial force at the junction (N_Sd) [kN]		1.69E+04		1.81E+04
Design bending moment at the junction (M_Sd) [kN.m]		4.83E+05		5.07E+05
Slope angle of the cone [deg]		5.65		5.65
Cone diameter (D_c) [m]	-	7.50	8.90	-
Cone thickness (t_c) [m]	-	0.10	0.08	-
Design axial stress at the section within the cone ($\sigma_{ac,Sd}$) [MPa]	-	7.33	8.30	-
Design bending stress at the section within the cone ($\sigma_{mc,Sd}$) [MPa]	-	113.47	105.16	-
Equivalent design axial stress within the conical transition ($\sigma_{eq,Sd}$) [MPa]		121.40		114.02
Tubular diameter (D_j) [m]	7.5	-	-	8.9
Tubular member thickness (t) [m]	0.10	-	-	0.07
Design axial stress in tubular section at junction ($\sigma_{at,Sd}$) [MPa]	-7.09	-	-	-8.47
Design bending stress in tubular section at junction ($\sigma_{mt,Sd}$) [MPa]	-111.26	-	-	-108.17
Local design bending stress at the tubular side ($\sigma_{mlt,Sd}$) [MPa]	-86.49	-	-	-109.25
Local design bending stress at the cone side ($\sigma_{mlc,Sd}$) [MPa]	-	-86.49	-95.83	-
Design hoop stress at unstiffened tubular-cone junction ($\sigma_{hc,Sd}$) [MPa]		-45.87		-56.98
Strength requirements - local buckling under axial compression				
Equivalent diameter (D_e) [m]	7.54	7.54	8.94	8.94
Critical elastic buckling coefficient (Ce)	0.3	0.3	0.3	0.3
Ratio f_y/f_{cle}	0.21	0.21	0.32	0.34
Characteristic elastic local buckling strength (f_{cle}) [MPa]	1652.20	1652.20	1110.53	1040.09
Local buckling strength of conical transition (f_{clc}) [MPa]	350.79	350.79	340.59	338.49
Criteria test	Ok	Ok	Ok	Ok
Junction yielding				
Diameter (D_j)	7.50	7.50	8.90	8.9
Thickness (t)	0.10	0.10	0.08	0.07
Critical elastic buckling coefficient (Ce)	0.30	0.30	0.30	0.30
Characteristic elastic local buckling strength (f_{cle}) [MPa]	1660.26	1660.26	1115.95	1045.16
Ratio f_y/f_{cle}	0.21	0.21	0.32	0.34
Characteristic local buckling strength (f_{cl}) [MPa]	350.89	350.89	340.74	338.65
Effective length factor (k)	1.00	1.00	1.00	1.00
Longer unbraced length (l) [m]	2.50	3.28	3.80	1.42
Radius of gyration (i) [m]	0.43	0.43	0.42	0.40
Smaller Euler buckling strength (f_E) [MPa]	60638.23	35227.26	24950.67	167439.67
Column slenderness parameter (λ)	0.08	0.10	0.12	0.04
Characteristic axial local compressive strength (f_{clj}) [MPa]	354.42	354.01	353.64	354.80
Elastic hoop buckling strength (f_{he}) [MPa]	2213.68	2213.68	1487.93	1393.55
Characteristic hoop buckling strength (f_h) [MPa]	355	355	355	355
$\sigma_{tot,Sd}$ - on the tubular side of the junction [MPa]	-204.84	-	-	-225.89
$\sigma_{tot,Sd}$ - on the cone side of the junction [MPa]	-	34.90	18.19	-
Criteria test (junction yielding)	Ok	Ok	Ok	Ok

Table 49: ULS calculation | Design 1 | Tubular connections.

			Tubular connection: junction2	
AXIAL COMPRESSION				
Component	can_1	can_2		
Critical elastic buckling coefficient (Ce)	0.3	0.3		
Characteristic elastic local buckling strength (f_cle) [MPa]	1528.11	1218.86		
Ratio f_y/f_cle	0.23	0.29		
Characteristic local buckling strength (f_cl) [MPa]	349.09	343.35		
Effective length factor (k)	1	1		
Longer unbraced length (l) [m]	3.28	3.80		
Radius of gyration (i) [m]	2.66	2.66		
Smaller Euler buckling strength (f_E) [MPa]	1363518.10	1015877.64		
Column slenderness parameter (λ)	0.02	0.02		
Characteristic axial compressive strength (f_c) [MPa]	354.97	354.97		
Axial compression resistance (N_c,Rd) [kN]	7.71E+05	6.17E+05		
Design axial compression (N_Sd) [kN]	1.75E+04	1.75E+04		
Criteria test	Ok	Ok		
BUCKLING - STABILITY AS A SHELL CYLINDER				
Z_l	25.49	42.89		
$\psi_{axial/bending}$	1	1		
$\epsilon_{axial/bending}$	17.89	30.11		
$\rho_{axial/bending}$	0.44	0.43		
C_axial	7.99	13.02		
Elastic buckling strength_axial (f_E_a)	1376.07	1063.47		
C_bending	7.99	13.02		
Elastic buckling strength_bending (f_E_b)	1376.07	1063.47		
$\psi_{torsion}$	5.34	5.34		
$\epsilon_{torsion}$	9.71	14.35		
$\rho_{torsion}$	0.6	0.6		
C_torsion_shear	7.90	10.13		
Elastic buckling strength_torsion (f_E_t)	1361.71	827.29		
σ_j	127.19	127.19		
λ_{s2}	-0.25	-0.32		
f_ks_d	299.53	294.04		
Criteria test	Ok	Ok		
BUCKLING - STABILITY AS A SHELL COLUMN				
Ratio 1	40.83	40.83		
Ratio 2	1478.87	1478.87		
Check	No test needed	No test needed		
BENDING MOMENT				
Elastic section modulus (W) [m ³]	4.97	3.99		
Plastic section modulus (Z) [m ³]	6.40	5.13		
Ratio f_y*D/E*t	0.14	0.17		
Check	Ok	Ok		
Characteristic bending strength (f_m) [MPa]	381.59	368.39		
Bending moment resistance (M_Rd) [kN.m]	1.65E+06	1.28E+06		
Design bending moment (M_Sd) [kN.m]	4.94E+05	4.94E+05		
Criteria test	Ok	Ok		
SHEAR FORCE				
Shear force resistance (V_Rd) [kN]	2.23E+05	1.78E+05		
Design shear force (V_Sd) [kN]	3.41E+03	3.41E+03		
Criteria test	Ok	Ok		
TORSIONAL MOMENT				
Polar moment of inertia (I_p) [m ⁴]	40.49	32.54		
Torsional moment resistance (M_T,Rd) [kN.m]	1.77E+06	1.42E+06		
Design torsional moment (M_T,Sd) [kN.m]	3.37E+04	3.37E+04		
Criteria test	Ok	Ok		
INTERACTION SHEAR, BENDING AND TORSION				
Ratio V_Sd/V_Rd	0.02	0.02		
Shear stress due to design torsional moment ($\tau_{T,Sd}$) [MPa]	3.27	4.10		
Design yield strength (f_d) [MPa]	308.70	308.70		
Reduced bending strength due to torsional moment (f_m,Red) [MPa]	381.52	368.29		
Reduced design bending moment resistance due to torsional moment (M_Red,Rd) [kN.m]	1648585.00	1278756.97		
Ratio M_Sd/M_Red,Rd	0.30	0.39		
Criteria test	Ok	Ok		

Table 52: ULS calculation | Design 2 | Tubular connections.

Tubular connection: junction1		
AXIAL COMPRESSION		
Component	top_can	can_1
Critical elastic buckling coefficient (Ce)	0.3	0.3
Characteristic elastic local buckling strength (f_cle) [MPa]	1828.26	1828.26
Ratio f_y/f_cle	0.19	0.19
Characteristic local buckling strength (f_cl) [MPa]	352.80	352.80
Effective length factor (k)	1	1
Longer unbraced length (l) [m]	2.50	2.00
Radius of gyration (i) [m]	2.65	2.44
Smaller Euler buckling strength (f_E) [MPa]	2333578.40	3088500.74
Column slenderness parameter (λ)	0.01	0.01
Characteristic axial compressive strength (f_c) [MPa]	354.98	354.99
Axial compression resistance (N_c,Rd) [kN]	780017.17	920880.69
Design axial compression (N_Sd) [kN]	16894.26	16894.26
Criteria test	Ok	Ok
BUCKLING - STABILITY AS A SHELL CYLINDER		
Z_1	14.61	7.90
$\psi_{axial/bending}$	1	1
$\epsilon_{axial/bending}$	10.26	5.54
$\rho_{axial/bending}$	0.45	0.46
C_axial	4.73	2.73
Elastic buckling strength_axial (f_E_a)	1701.54	2147.52
C_bending	4.73	2.73
Elastic buckling strength_bending (f_E_b)	1701.54	2147.52
ψ	5.34	5.34
ϵ	6.40	4.03
ρ	0.6	0.6
C_torsion_shear	6.58	5.86
Elastic buckling strength_torsion (f_E_t)	2365.08	4616.73
σ_j	137.78	137.78
λ_{s2}	-0.16	-0.13
f_ks_d	304.82	306.20
Criteria test	Ok	Ok
BUCKLING - STABILITY AS A SHELL COLUMN		
Ratio 1	41.07	48.49
Ratio 2	1478.87	1478.87
Check	No test needed	No test needed
BENDING MOMENT		
Elastic section modulus (W) [m ³]	4.60	5.40
Plastic section modulus (Z) [m ³]	5.95	7.00
Ratio f_y*D/E*t	0.12	0.10
Check	Ok	Ok
Characteristic bending strength (f_m) [MPa]	390.47	402.83
Bending moment resistance (M_Rd) [kN.m]	1562716.35	1893189.67
Design bending moment (M_Sd) [kN.m]	482515	482515
Criteria test	Ok	Ok
SHEAR FORCE		
Shear force resistance (V_Rd) [kN]	225181.09	265843.86
Design shear force (V_Sd) [kN]	3406	3406
Criteria test	Ok	Ok
TORSIONAL MOMENT		
Polar moment of inertia (I_p) [m ⁴]	34.52	40.54
Torsional moment resistance (M_T,Rd) [kN.m]	1640558.68	1926510.80
Design torsional moment (M_T,Sd) [kN.m]	33737	33737
Criteria test	Ok	Ok
INTERACTION SHEAR, BENDING AND TORSION		
Ratio V_Sd/V_Rd	0.02	0.01
Shear stress due to design torsional moment ($\tau_{T,Sd}$) [MPa]	3.51	2.96
Design yield strength (f_d) [MPa]	308.70	308.70
Reduced bending strength due to torsional moment (f_m,Red) [MPa]	390.39	402.77
Reduced design bending moment resistance due to torsional moment (M_Red,Rd) [kN.m]	1562413.50	1892927.87
Ratio M_Sd/M_Red,Rd	0.31	0.25
Criteria test	Ok	Ok

Table 53: ULS calculation | Design 3 | Reduced thickness.

	top_can	can_1	can_1	collar	collar	can_2	can_2	bottom_can
	Conical		Tubular		Tubular			Conical
Material factor (γ_m)	1.15	1.15	1.15	1.15	1.15	1.15	1.15	1.15
Outer diameter [m]	7.50	7.50	8.13	8.13	8.38	8.38	8.90	8.90
Expected maximum corrosion rate (V_corr) [mm/year]	0.30	0.30	0.30	0.30	0.30	0.30	0.30	0.30
Design useful life of the coating (Tc) [years]	20.00	20.00	20.00	20.00	20.00	20.00	20.00	20.00
Design life of the structure (Td) [years]	31.50	31.50	31.50	31.50	31.50	31.50	31.50	31.50
Real thickness [m]	0.10	0.10	0.10	0.08	0.08	0.07	0.07	0.07
Corrosion allowance (CA) [m]	0.0035	0.0035	0.0035	0.0035	0.0035	0.0035	0.0035	0.0035
Thickness (t_p) [m]	0.09	0.09	0.09	0.07	0.07	0.07	0.07	0.06
Area [m ²]	2.16	2.16	2.34	1.84	1.90	1.82	1.94	1.74

Table 54: ULS calculation | Design 3 | Conical connections.

Component	Conical connection: junction1		Conical connection: junction4	
	top_can	can_1	can_2	bottom_can
Design axial force at the junction (N_Sd) [kN]		1.68E+04		1.80E+04
Design bending moment at the junction (M_Sd) [kN.m]		4.83E+05		5.07E+05
Slope angle of the cone [deg]		5.00		5.00
Cone diameter (D_c) [m]	-	7.50	8.90	-
Cone thickness (t_c) [m]	-	0.09	0.07	-
Design axial stress at the section within the cone ($\sigma_{ac,Sd}$) [MPa]	-	7.79	9.30	-
Design bending stress at the section within the cone ($\sigma_{mc,Sd}$) [MPa]	-	120.62	118.47	-
Equivalent design axial stress within the conical transition ($\sigma_{eq,Sd}$) [MPa]		128.90		128.27
Tubular diameter (D_j) [m]	7.50	-	-	8.90
Tubular member thickness (t) [m]	0.09	-	-	0.06
Design axial stress in tubular section at junction ($\sigma_{at,Sd}$) [MPa]	-7.51	-	-	-9.80
Design bending stress in tubular section at junction ($\sigma_{mt,Sd}$) [MPa]	-117.91	-	-	-125.66
Local design bending stress at the tubular side ($\sigma_{mlt,Sd}$) [MPa]	-83.69	-	-	-122.97
Local design bending stress at the cone side ($\sigma_{mlc,Sd}$) [MPa]	-	-83.69	-99.55	-
Design hoop stress at unstiffened tubular-cone junction ($\sigma_{hc,Sd}$) [MPa]		-44.38		-63.47
Strength requirements - local buckling under axial compression				
Equivalent diameter (D_e) [m]	7.53	7.53	8.93	8.93
Critical elastic buckling coefficient (Ce)	0.3	0.3	0.3	0.3
Ratio f_y/f_cle	0.23	0.23	0.36	0.40
Characteristic elastic local buckling strength (f_cle) [MPa]	1553.53	1553.53	984.77	886.05
Local buckling strength of conical transition (f_clc) [MPa]	349.46	349.46	336.62	332.71
Criteria test	Ok	Ok	Ok	Ok
Junction yielding				
Diameter (D_j)	7.50	7.50	8.90	8.90
Thickness (t)	0.09	0.09	0.07	0.06
Critical elastic buckling coefficient (Ce)	0.30	0.30	0.30	0.30
Characteristic elastic local buckling strength (f_cle) [MPa]	1559.46	1559.46	988.53	889.43
Ratio f_y/f_cle	0.23	0.23	0.36	0.40
Characteristic local buckling strength (f_cl) [MPa]	349.54	349.54	336.75	332.86
Effective length factor (k)	1.00	1.00	1.00	1.00
Longer unbraced length (l) [m]	2.50	3.60	2.99	1.42
Radius of gyration (i) [m]	0.41	0.41	0.39	0.37
Smaller Euler buckling strength (f_E) [MPa]	57002.85	27428.82	35831.06	142668.57
Column slenderness parameter (λ)	0.08	0.11	0.10	0.05
Characteristic axial local compressive strength (f_clj) [MPa]	354.39	353.73	354.07	354.77
Elastic hoop buckling strength (f_he) [MPa]	2079.28	2079.28	1318.04	1185.91
Characteristic hoop buckling strength (f_h) [MPa]	355.00	355.00	355.00	355.00
$\sigma_{tot,Sd}$ - on the tubular side of the junction [MPa]	-209.11	-	-	-258.43
$\sigma_{tot,Sd}$ - on the cone side of the junction [MPa]	-	45.20	28.71	-
Criteria test (junction yielding)	Ok	Ok	Ok	Ok

Table 55: ULS calculation | Design 3 | Tubular connections.

		Tubular connection: junction2		Tubular connection: junction3	
AXIAL COMPRESSION					
Component	can_1	collar	collar	can_2	
Critical elastic buckling coefficient (Ce)	0.3	0.3	0.3	0.3	
Characteristic elastic local buckling strength (f_cle) [MPa]	1438.51	1128.57	1095.31	1050.19	
Ratio f_y/f_cle	0.25	0.31	0.32	0.34	
Characteristic local buckling strength (f_cl) [MPa]	347.68	341.09	340.16	338.80	
Effective length factor (k)	1	1	1	1	
Longer unbraced length (l) [m]	3.60	0.49	0.49	2.99	
Radius of gyration (i) [m2]	2.58	2.91	2.95	3.01	
Smaller Euler buckling strength (f_E) [MPa]	1065539.25	73291233.87	74872582.57	2102074.28	
Column slenderness parameter (λ)	0.02	0.00	0.00	0.01	
Characteristic axial compressive strength (f_c) [MPa]	354.97	355.00	355.00	354.98	
Axial compression resistance (N_c,Rd) [kN]	7.24E+05	5.69E+05	5.87E+05	5.63E+05	
Design axial compression (N_Sd) [kN]	1.75E+04	1.75E+04	1.76E+04	1.76E+04	
Criteria test	Ok	Ok	Ok	Ok	
BUCKLING - STABILITY AS A SHELL CYLINDER					
Z_l	32.83	0.77	0.75	29.08	
ψ _{axial/bending}	1	1	1	1	
ε _{axial/bending}	23.05	0.54	0.53	20.41	
ρ _{axial/bending}	0.44	0.43	0.43	0.42	
C_axial	10.19	1.03	1.02	8.68	
Elastic buckling strength_axial (f_E_a)	1282.84	4303.60	4296.37	901.35	
C_bending	10.19	1.03	1.02	8.68	
Elastic buckling strength_bending (f_E_b)	1282.84	4303.60	4296.37	901.35	
ψ	5.34	5.34	5.34	5.34	
ε	11.74	0.71	0.69	10.72	
ρ	0.6	0.6	0.6	0.6	
C_torsion_shear	8.84	5.36	5.36	8.36	
Elastic buckling strength_torsion (f_E_t)	1113.04	22457.90	22454.81	867.61	
σ _j	137.78	137.78	135.58	135.58	
λ _{s2}	-0.28	-0.09	-0.09	-0.41	
f_ks_d	296.92	307.53	307.52	285.92	
Criteria test	Ok	Ok	Ok	Ok	
BUCKLING - STABILITY AS A SHELL COLUMN					
Ratio 1	43.28	34.04	33.32	31.96	
Ratio 2	1478.87	1478.87	1478.87	1478.87	
Check	No test needed	No test needed	No test needed	No test needed	
BENDING MOMENT					
Elastic section modulus (W) [m ³]	4.66	3.68	3.91	3.75	
Plastic section modulus (Z) [m ³]	6.00	4.73	5.02	4.82	
Ratio f_y*D/E*t	0.15	0.19	0.19	0.20	
Check	Ok	Ok	Ok	Ok	
Characteristic bending strength (f_m) [MPa]	378.30	363.28	361.20	358.18	
Bending moment resistance (M_Rd) [kN.m]	1.53E+06	1.16E+06	1.23E+06	1.17E+06	
Design bending moment (M_Sd) [kN.m]	4.95E+05	4.95E+05	4.96E+05	4.96E+05	
Criteria test	Ok	Ok	Ok	Ok	
SHEAR FORCE					
Shear force resistance (V_Rd) [kN]	2.09E+05	1.64E+05	1.69E+05	1.62E+05	
Design shear force (V_Sd) [kN]	3.41E+03	3.41E+03	3.41E+03	3.41E+03	
Criteria test	Ok	Ok	Ok	Ok	
TORSIONAL MOMENT					
Polar moment of inertia (I_p) [m ⁴]	37.86	29.93	32.76	31.45	
Torsional moment resistance (M_T,Rd) [kN.m]	1.66E+06	1.31E+06	1.39E+06	1.34E+06	
Design torsional moment (M_T,Sd) [kN.m]	3.37E+04	3.37E+04	3.37E+04	3.37E+04	
Criteria test	Ok	Ok	Ok	Ok	
INTERACTION SHEAR, BENDING AND TORSION					
Ratio V_Sd/V_Rd	0.02	0.02	0.02	0.02	
Shear stress due to design torsional moment (τ _{T,Sd}) [MPa]	3.50	4.46	4.20	4.38	
Design yield strength (f_d) [MPa]	308.70	308.70	308.70	308.70	
Reduced bending strength due to torsional moment (f_m,Red) [MPa]	378.23	363.17	361.10	358.07	
Reduced design bending moment resistance due to torsional moment (M_Red,Rd) [kN.m]	1531635.24	1162354.10	1227967.11	1168757.16	
Ratio M_Sd/M_Red,Rd	0.32	0.43	0.40	0.42	
Criteria test	Ok	Ok	Ok	Ok	

B.5. Extrapolated values - hot spot stress

Table 56: Hot spot stress calculation | Design 1.

	Junction1		Junction2		Junction3	
	Point1	Point2	Point1	Point2	Point1	Point2
Thickness [mm]	104		84		79	
Distance [mm]	52	156	42	126	39.5	118.5
Element ID	17170	17021	31258	31373	32837	32662
$\sigma_{//}$ [MPa]	-41.86	-38.43	-3.09	-2.62	45.98	43.73
σ_{\perp} [MPa]	-109.21	-100.76	-119.84	-112.37	-107.07	-98.93
τ_{\perp} [MPa]	-3.71	-3.69	-3.82	-3.80	-3.58	-3.54
σ_1 [MPa]	-41.66	-38.21	-2.96	-2.48	46.06	43.82
σ_2 [MPa]	-109.41	-100.98	-119.97	-112.50	-107.15	-99.02
α	0.8	0.8	0.8	0.8	0.8	0.8
σ_{ef1} [MPa]	109.26	100.82	119.89	112.42	107.12	98.99
σ_{ef2} [MPa]	33.32	30.57	2.37	1.99	36.85	35.05
σ_{ef3} [MPa]	87.53	80.78	95.97	90.00	85.72	79.22
σ_{eff} [MPa]	109.26	100.82	119.89	112.42	107.12	98.99
Extrapolated value [MPa]	113.48		123.63		111.18	
New deviation [%]	4.27		2.80		4.81	

Table 57: Hot spot stress calculation | Design 3.

	Junction1		Junction2		Junction3		Junction4	
	Point1	Point2	Point1	Point2	Point1	Point2	Point1	Point2
Thickness [mm]	98		78		75		68	
Distance [mm]	49	147	39	117	37.5	112.5	34	102
Element ID	16201	18727	31725	32653	30721	30644	31680	31838
$\sigma_{//}$ [MPa]	-40.53	-38.35	-58.25	-42.34	68.58	71.26	48.46	46.90
σ_{\perp} [MPa]	-119.27	-115.87	-127.53	-121.87	-125.39	-119.76	-123.04	-109.93
τ_{\perp} [MPa]	-3.95	-3.86	-4.26	-4.33	-4.21	-4.22	-4.08	-4.05
σ_1 [MPa]	-40.33	-38.16	-57.99	-42.11	68.67	71.35	48.56	47.01
σ_2 [MPa]	-119.47	-116.06	-127.79	-122.10	-125.48	-119.85	-123.13	-110.03
α	0.8	0.8	0.8	0.8	0.8	0.8	0.8	0.8
σ_{ef1} [MPa]	119.33	115.92	127.59	121.93	125.44	119.82	123.09	109.99
σ_{ef2} [MPa]	32.26	30.53	46.39	33.69	54.94	57.08	38.85	37.61
σ_{ef3} [MPa]	95.58	92.85	102.23	97.68	100.38	95.88	98.51	88.02
σ_{eff} [MPa]	119.33	115.92	127.59	121.93	125.44	119.82	123.09	109.99
Extrapolated value [MPa]	121.03		130.42		128.25		129.65	
New deviation [%]	3.66		5.34		5.40		4.43	

C. FEA PLOTS

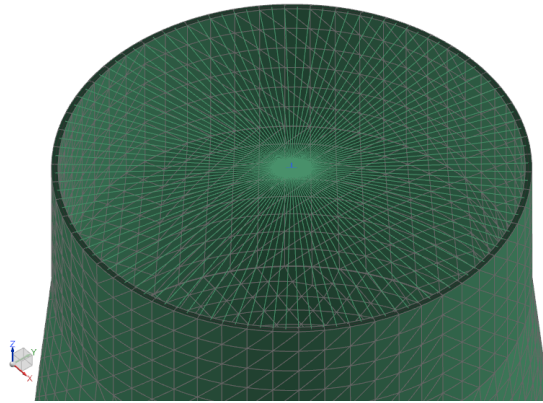


Figure 63: Detail of the node created to impose the loads and the rigid link connections with the top face. The element size is 400 mm to improve visibility.

Listing 1: Mesh quality results | Design 1

```
1 Environment:      Simcenter Samcef - Structural
2 Solver:          Simcenter Samcef
3 =====
4 Results of Element Shape Check
5 =====
6 Overview
7
8               Number Failed  Number Warning  Number Checked
9 Elements           0             0             57826
10
11 Check           Number Failed  Number Warning  Worst Value
12 Tet Collapse     0             0             -N/A-
13 Aspect Ratio     0             0             2.423375
14 Warp Factor      0             0             -N/A-
```

Listing 2: Mesh quality results | Design 3

```
1 Environment:      Simcenter Samcef - Structural
2 Solver:          Simcenter Samcef
3 =====
4 Results of Element Shape Check
5 =====
6 Overview
7               Number Failed  Number Warning  Number Checked
8 Elements           0             0             53551
9
10 Check           Number Failed  Number Warning  Worst Value
11 Tet Collapse     0             0             -N/A-
12 Aspect Ratio     0             0             1.817288
13 Warp Factor      0             0             -N/A-
```

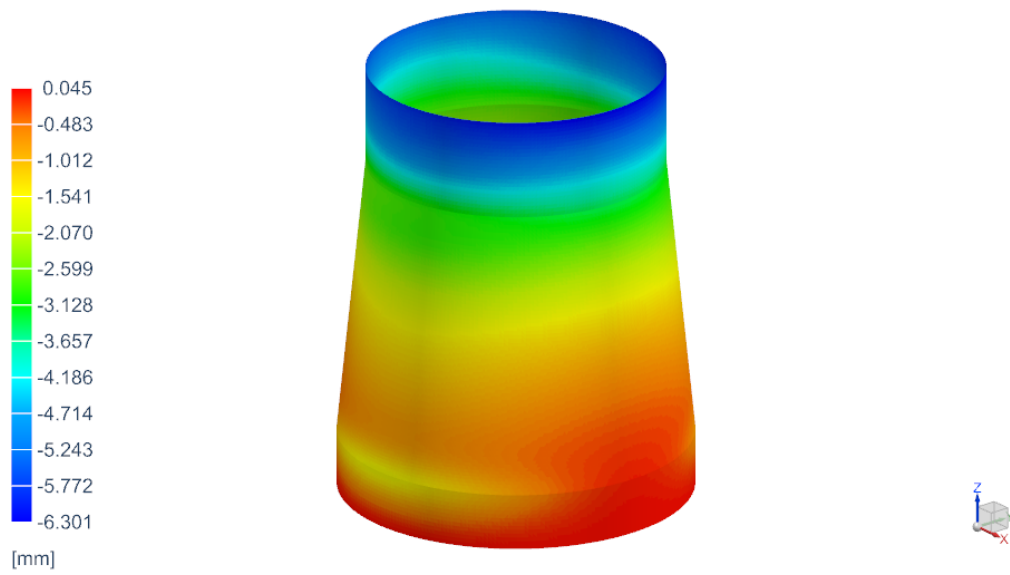


Figure 64: Displacement in y-direction | Design 1

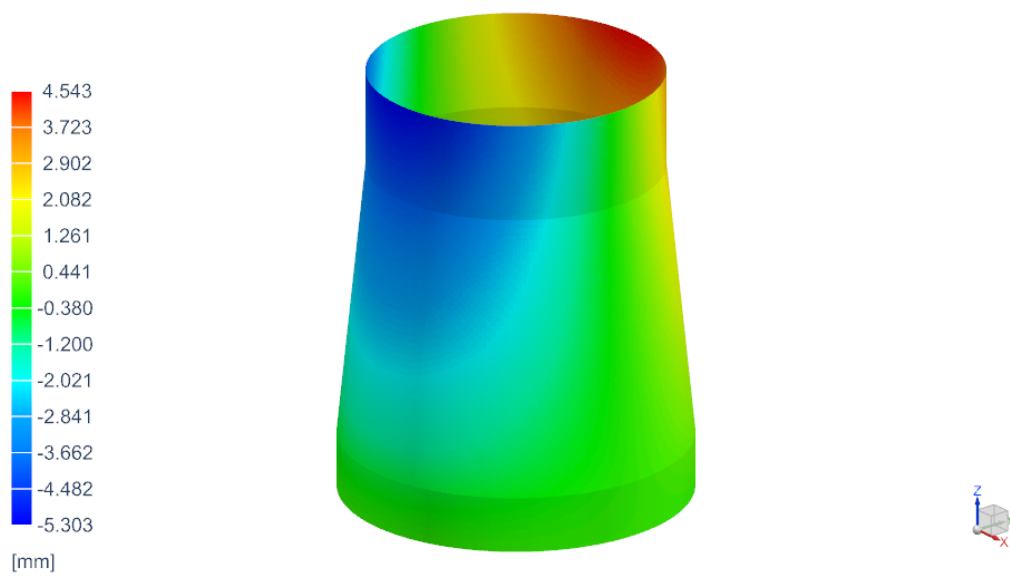


Figure 65: Displacement in z-direction | Design 1

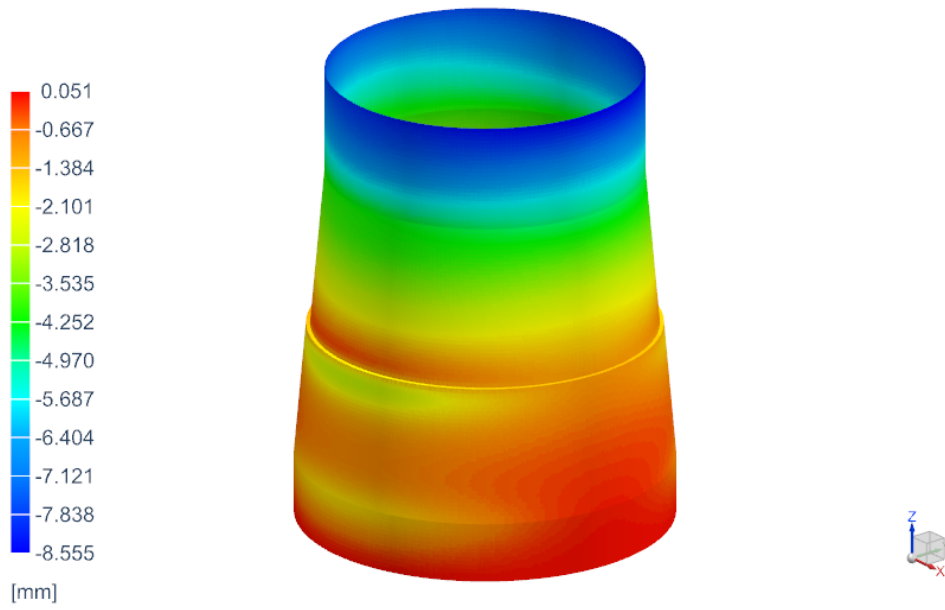


Figure 66: Displacement in y-direction | Design 3

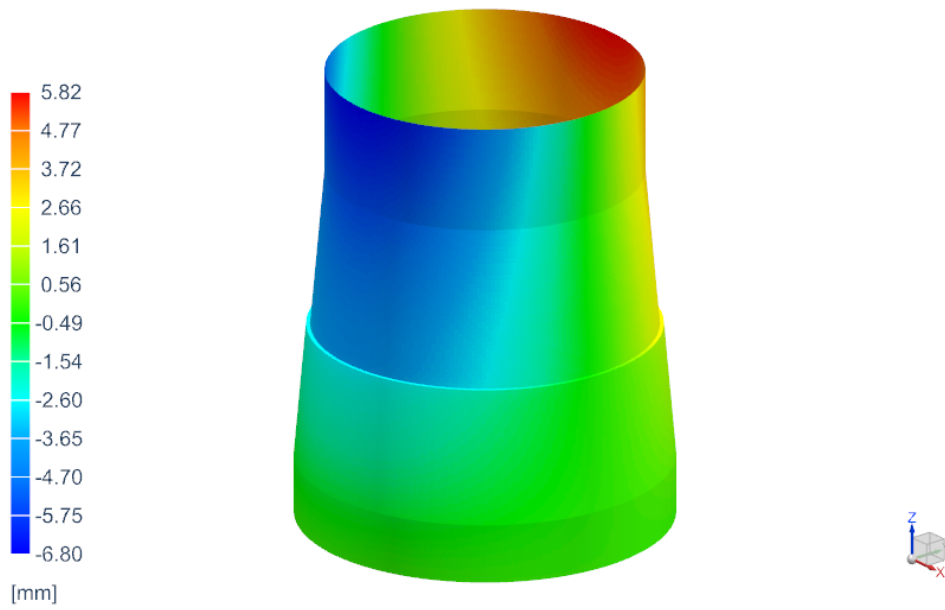


Figure 67: Displacement in z-direction | Design 3.

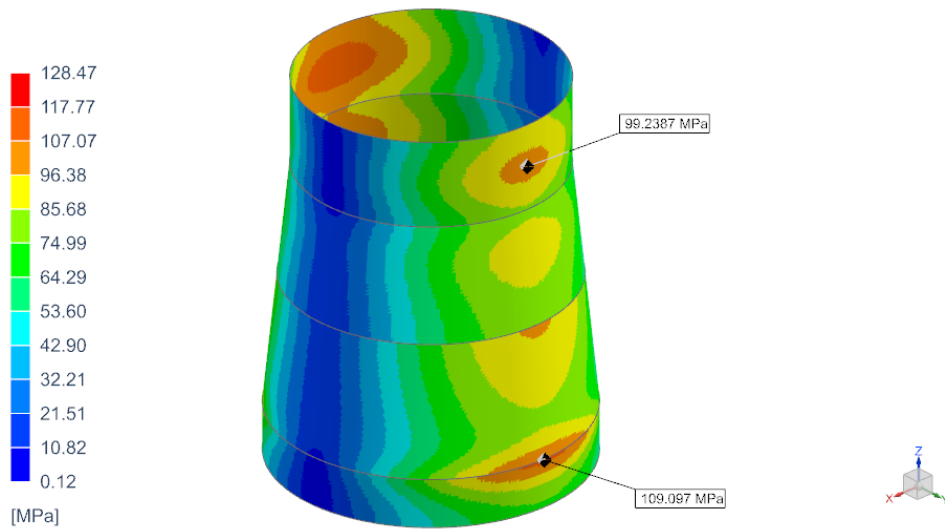


Figure 68: Stresses on the other side of the TP. Values are element average and banded feature display. Maximum values on this side are indicated | Design 1.

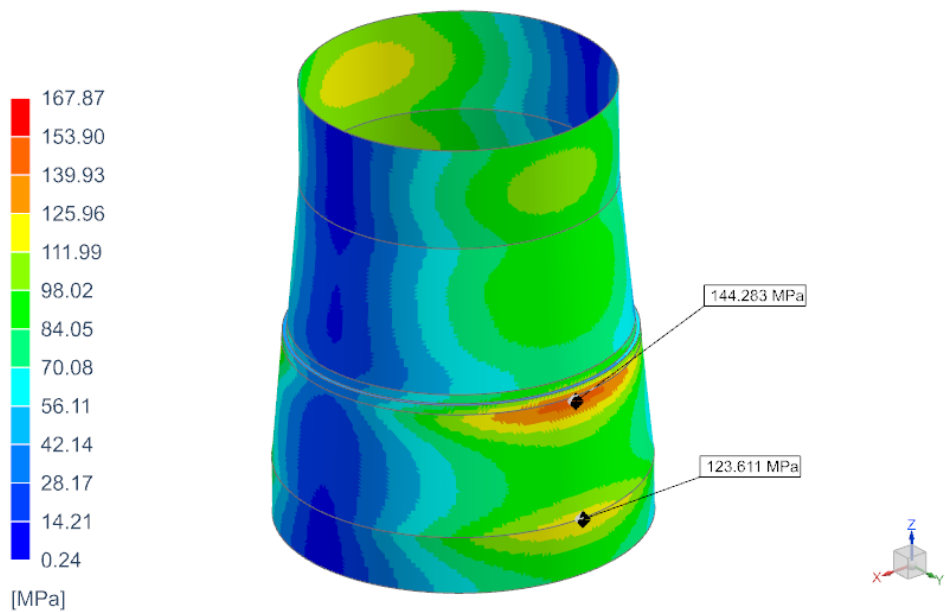


Figure 69: Stresses on the other side of the TP. Values are element average and banded feature display. Maximum values on this side are indicated | Design 3.